



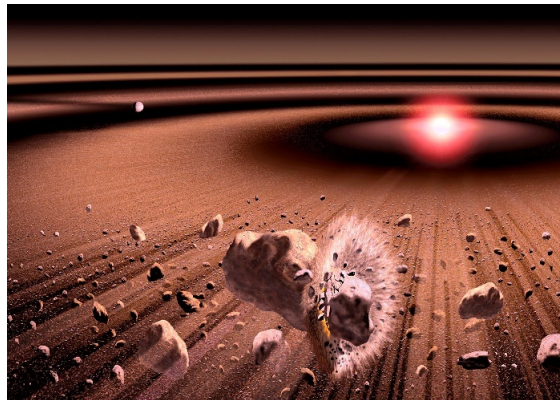
FRIEDRICH-SCHILLER-UNIVERSITÄT JENA  
PHYSIKALISCH-ASTRONOMISCHE FAKULTÄT  
ASTROPHYSIKALISCHES INSTITUT UND  
UNIVERSITÄTS-STERNWARTE



# Collisional modelling of resolved debris discs

—DISSERTATION—

zur Erlangung des akademischen Grades  
Doctor rerum naturalium (Dr. rer. nat.)



vorgelegt dem Rat der Physikalisch-Astronomischen Fakultät  
der Friedrich-Schiller-Universität Jena

von Dipl.-Phys. CHRISTIAN SCHÜPPLER  
geboren am 12. Juni 1987 in Hildburghausen

26. Januar 2017

1. Gutachter: Prof. Dr. ALEXANDER V. KRIVOV  
*Friedrich-Schiller-Universität Jena*

2. Gutachter: Prof. Dr. JÜRGEN BLUM  
*TU Braunschweig*

3. Gutachter: Prof. Dr. PHILIPPE THÉBAULT  
*LESIA Observatoire de Paris*

Tag der Disputation: 5. Januar 2017

Image on the title page:  
Artist impression of a planetesimal collision in a circumstellar disc  
(Illustration by Kouji Kanba, ISAS/JAX)



# Kurzfassung

Trümmerscheiben sind optisch dünne, zirkumstellare Scheiben, bestehend aus Körpern verschiedenster Größen, angefangen von winzigen, (Sub-)Mikrometer großen Staubteilchen bis hin zu Objekten mit hunderten von Kilometern im Durchmesser. Letztere werden als Planetesimale bezeichnet. Abrieb und Zerstörung miteinander kollidierender Planetesimale führen zu einer ständigen Nachproduktion des kurzlebigen Trümmerscheibenstaubes. Die planetesimalen Reservoirs ähneln dem Asteroiden- und dem Kuipergürtel in unserem Sonnensystem. Trümmerscheiben können durch die Messung von Streulicht und thermischer Emission der sich in ihnen befindenden Staubteilchen detektiert werden. Sie werden mit signifikanter Häufigkeit um Hauptreihen- und Nachhauptreihensterne gefunden und gelten zusammen mit Planeten als Endprodukte der Stern- und Planetenentstehungsprozesse. Untersuchungen von Trümmerscheiben liefern somit wichtige Informationen über Planetensysteme und über Vorgänge, die sich in solchen Systemen in der Vergangenheit abgespielt haben.

In dieser Dissertation werden Trümmerscheiben mithilfe der Kollisionsmodellierung untersucht, bei welcher die langzeitige Kollisionsentwicklung von Planetesimalen zu Staub simuliert wird. Die hiernach berechneten Staubverteilungen werden für den Vergleich mit Beobachtungsdaten verwendet. Das Verfahren erlaubt Rückschlüsse auf Eigenschaften der staubproduzierenden Planetesimalgürtel, die nicht direkt durch Beobachtungen zugänglich sind. Dies steht im Gegensatz zur klassischen Modellierung, welche sich allein auf Untersuchungen des sichtbaren Staubes beschränkt.

Zur Modellierung wird das Programm *ACE* der Jenaer AIU-Gruppe verwendet. Es simuliert die Entwicklung rotationssymmetrischer Trümmerscheiben, basierend auf einer statistischen Methode zur Berechnung von Kollisionen zwischen Ensembles zirkumstellarer Körper. Neben Kollisionen betrachtet *ACE* auch die Einflüsse der stellaren Gravitation sowie Effekte durch radiative und korpuskulare Kräfte, die der Zentralstern auf die Trümmerscheibenmaterie ausübt. Es werden drei ausgewählte Trümmerscheibensysteme betrachtet, HIP 17439, AU Microscopii und  $q^1$  Eridani, bei denen jeweils der äußere Teil der Scheibe in mehreren Wellenlängenbereichen räumlich aufgelöst worden ist.

Alle drei Systeme besitzen Anzeichen für eine Zweikomponentenstruktur aus einer warmen und einer kalten Staubpopulation. Die in dieser Dissertation präsentierten Modellierungen verfolgen die Frage nach dem Ursprung dieser beiden Populationen. Hierzu werden zwei Szenarien betrachtet. Dies ist zum einen eine sonnensystemähnliche Architektur mit einem inneren und einem äußeren Planetesimalgürtel als In-situ-Quellen des Staubes (Szenario I) und zum anderen ein äußerer Planetesimalgürtel, von welchem Staub durch den Poynting-Robertson-Effekt und durch Sternwinde nach innen, d. h. Richtung Stern, transportiert wird (Szenario II). Während Szenario I für  $q^1$  Eridani am plausibelsten erscheint, wird Szenario II bei AU Microscopii bevorzugt. Für HIP 17439 kann jedoch keine klare Aussage getroffen werden, da beide Szenarien als Möglich-

keiten in Betracht kommen. Ferner können hier mehr als zwei Planetesimalgürtel oder sogar ein radial ausgedehnter bzw. sehr breiter Planetesimalgürtel nicht ausgeschlossen werden.

Die Beobachtbarkeit der ermittelten Scheibenarchitekturen wird diskutiert und z. T. modelliert. Kontraststarke Aufnahmen zukünftiger Beobachtungskampagnen bieten eine potentielle Möglichkeit die inneren Scheibenkomponenten aufzulösen, obwohl dies durch ihre erwartete geringe Oberflächenhelligkeit erschwert wird. Prognosen für das Vorhandensein von bisher unentdeckten Planeten werden anhand der abgeleiteten Verteilungen der Planetesimale und deren dynamischer Anregung getroffen.

# Abstract

Debris discs are optically thin circumstellar discs that comprise solids in a broad range of sizes, beginning from tiny (sub)micron-sized dust grains up to objects with hundreds of kilometres in diameter, referred to as planetesimals. The dust component of debris discs is short-lived and continuously replenished through collisional attrition between planetesimals in reservoirs analogous to the Solar system’s asteroid and Kuiper belts. Debris discs are detected by observing the scattered light and the thermal emission of their dust. They have been found around a significant fraction of main- and post-main-sequence stars, and are believed to be the end product of the star and planet formation process, together with planets. Thus, analysing debris discs provides important information on planetary systems and can shed light on the processes that were operating in the past.

In this thesis, collisional modelling is employed, which simulates the long-term collisional evolution from planetesimals to dust. The calculated dust distributions are used for the comparison with observational data. This powerful technique allows one to infer properties of the underlying dust-producing planetesimal belts which are not directly discernible by observations. This is opposed to classic modelling approaches that only focus on investigations of the visible dust portion of debris discs.

The **ACE** code of the Jena AIU research group is used which predicts the evolution of rotationally-symmetric debris discs. It is based on a statistical approach to calculate collisions between ensembles of circumstellar objects. Beside collisions, **ACE** considers the influence of stellar gravity as well as stellar radiative and corpuscular forces working on the circumstellar material. The code is applied to three selected systems – HIP 17439, AU Microscopii, and  $\alpha$  Eridani. In each system, the outer part of a debris disc is spatially resolved at multiple wavelengths.

All three systems show hints for a two-component structure of warm and cold dust populations. The modelling presented in this thesis addresses the question of what might be the origin of these dust populations. Two scenarios are considered: a Solar system-like architecture with an inner and an outer planetesimal belt as in-situ sources of dust (Scenario I), and an outer planetesimal belt from which dust is transported inwards by Poynting-Robertson and stellar wind drag (Scenario II). While Scenario I seems to be the most plausible for  $\alpha$  Eridani, Scenario II is preferred for AU Microscopii. However, no strict conclusion can be drawn for HIP 17439, where both scenarios are possible. More than two planetesimal belts or even a radially extended planetesimal belt cannot be excluded either.

The observability of the proposed disc architectures is discussed and modelled. Future high-contrast imaging offers a potential avenue to resolve the inner disc component directly, although this is complicated by the relatively low expected surface brightness. Possibilities for the presence of yet undetected planets in the systems are discussed from the derived underlying planetesimal distributions and their dynamical excitation.





# Contents

<b>Kurzfassung</b>	<b>v</b>
<b>Abstract</b>	<b>vii</b>
<b>Contents</b>	<b>1</b>
<b>1 Introduction</b>	<b>3</b>
1.1 Debris discs . . . . .	3
1.2 Insights from observations and modelling . . . . .	5
1.3 Collisional versus classic modelling . . . . .	10
1.4 Aims of this work . . . . .	11
<b>2 Fundamentals</b>	<b>13</b>
2.1 Keplerian motion and orbital elements . . . . .	13
2.2 Physical processes in debris discs . . . . .	14
2.2.1 Collisions . . . . .	14
2.2.2 Pressure forces . . . . .	16
2.2.3 Drag forces . . . . .	18
2.2.4 Other forces . . . . .	19
2.2.5 Planetary perturbations . . . . .	19
2.3 Kinetic theory . . . . .	20
2.3.1 General description . . . . .	20
2.3.2 Implementation: the ACE code . . . . .	22
2.4 Interaction between dust and stellar radiation . . . . .	24
2.4.1 Thermal emission . . . . .	25
2.4.2 Scattered light . . . . .	26
2.4.3 Numerical tools . . . . .	28
<b>3 HIP 17439</b>	<b>30</b>
3.1 System description and previous work . . . . .	30
3.2 Observational data . . . . .	31
3.3 Modelling . . . . .	32
3.4 Models with one planetesimal belt . . . . .	34
3.4.1 First-guess model . . . . .	34
3.4.2 Adding stellar winds . . . . .	34
3.4.3 Shifting the planetesimal belt . . . . .	39
3.5 Models with two planetesimal belts . . . . .	39
3.6 Possibility of an extended planetesimal belt . . . . .	43
3.7 Prospects for observations . . . . .	44
3.8 Conclusions and discussion . . . . .	46
<b>4 AU Microscopii</b>	<b>48</b>
4.1 System description . . . . .	48

# CONTENTS

4.2	Data used . . . . .	51
4.2.1	Stellar parameters . . . . .	51
4.2.2	ALMA observations . . . . .	52
4.2.3	Auxiliary thermal emission data . . . . .	53
4.2.4	Scattered light observations . . . . .	55
4.3	Modelling parameters . . . . .	56
4.3.1	Stellar winds and mass-loss rate . . . . .	56
4.3.2	Material properties . . . . .	56
4.3.3	Setups . . . . .	57
4.4	Probing the resolved outer disc . . . . .	58
4.4.1	Stellar wind strength . . . . .	58
4.4.2	Chemical composition of solids . . . . .	67
4.4.3	Eccentricity of planetesimal orbits . . . . .	69
4.4.4	Planetesimal belt width . . . . .	71
4.5	Probing the unresolved central emission . . . . .	73
4.6	Comparison with classic modelling . . . . .	75
4.7	Conclusions and discussion . . . . .	76
<b>5</b>	<b>q<sup>1</sup> Eridani</b>	<b>79</b>
5.1	System description . . . . .	79
5.2	Long-term collisional evolution model . . . . .	80
5.2.1	Extended planetesimal disc . . . . .	80
5.2.2	Two narrow planetesimal belts . . . . .	84
5.3	Application to q <sup>1</sup> Eri . . . . .	86
5.3.1	Stellar parameters . . . . .	86
5.3.2	Observational data . . . . .	86
5.3.3	Modelling results . . . . .	86
5.4	Conclusions and discussion . . . . .	90
<b>6</b>	<b>Conclusive remarks</b>	<b>94</b>
6.1	Summary . . . . .	94
6.2	Outlook . . . . .	99
	<b>References</b>	<b>101</b>
	<b>Units</b>	<b>127</b>
	<b>List of Figures</b>	<b>129</b>
	<b>List of Tables</b>	<b>130</b>
	<b>Danksagung</b>	<b>131</b>
	<b>Ehrenwörtliche Erklärung</b>	<b>133</b>
	<b>Lebenslauf</b>	<b>135</b>

# 1 Introduction

## 1.1 Debris discs

Since the discovery of the first extrasolar planet around a Sun-like star (Mayor & Queloz, 1995), thousands of such objects have been found with a large diversity of properties.<sup>1)</sup> Thus, astronomy has been enriched with an exciting new field of research which is planetary science. However, planets are only one of the two material classes detectable around mature stars. The other class consists of debris discs that are optically thin belts of solids, including comets, asteroids, and dust particles, which revolve around their host stars (Backman & Paresce, 1993; Wyatt, 2008; Krivov, 2010; Matthews et al., 2014). Like planets, debris discs are believed to be generic outcomes of the planet formation process (Wetherill, 1980; Lissauer, 1987).

The origin of debris discs goes back to the early stages of star formation. A star is formed at the centre of a collapsing interstellar cloud (Shu et al., 1993) where it is surrounded by an envelope of primordial material. Owing to rotation, the envelope is flattened to a gas- and dust-rich protoplanetary disc (Adams & Lin, 1993), in which planets can form (see, Beckwith et al., 2000; Montmerle et al., 2006; Youdin & Kenyon, 2013, for reviews).

This requires different growth mechanisms. First, sticking collisions between micron-sized grains at low relative velocities cause an agglomeration to decimetre-sized aggregates (Blum & Wurm, 2008; Güttler et al., 2010). However, the sticking efficiency drops with increasing aggregate size because of their larger relative velocities. This leads to the so-called barriers for bouncing (Blum & Wurm, 2008) and fragmentation (Zsom et al., 2010), beyond which dust aggregates bounce off one another or disperse to fragments rather than accrete. Different models seem to be physically feasible to overcome or avoid these barriers. Some models suggest that particles grow further in transient high pressure zones and streaming instabilities (Johansen et al., 2006, 2007). Other models propose the possibility of growth by mass transfer in high-velocity collisions between large targets and small projectiles (e.g., Wurm et al., 2005; Windmark et al., 2012; Garaud et al., 2013), or the formation of icy pebbles through direct sticking (e.g., Kataoka et al., 2013) of water-ice grains with high stickiness (Gundlach & Blum,

---

<sup>1)</sup>See [exoplanet.eu](http://exoplanet.eu) and [exoplanets.org](http://exoplanets.org).

## 1 Introduction

2015). Outcomes of all these processes are asteroidal or cometary bodies, called planetesimals, ranging in size from a few kilometres to hundreds of kilometres (Johansen et al., 2014). After the phases of runaway growth (Greenberg et al., 1978; Wetherill & Stewart, 1989), where the largest bodies grow the fastest, and the subsequent oligarchic growth (Ida & Makino, 1993), where the growth rate slows down to a similar rate for all bodies, the protoplanetary disc is populated with planetary embryos. Interior to the ice line, i.e. a region of the disc that is too hot for gaseous hydrogen-rich compounds to condense, further collisional agglomeration of planetary embryos leads to terrestrial planets (see, Raymond et al., 2014, for review). Outside the ice line the protoplanets can reach a critical core mass of  $10 M_{\oplus}$  where rapid gas accretion onto the planetary core is triggered, resulting in the formation of gas giants (see, Chabrier et al., 2014, for review).

The protoplanetary disc phase lasts until the gas is dispersed, possibly through viscous accretion and photoevaporation although these mechanisms are still debated. The gas dispersal is generally believed to occur a few Myr after the birth of the protostar (Haisch et al., 2001; Hillenbrand et al., 2008). This probably happens earlier for protoplanetary discs around high-mass stars (Ribas et al., 2015, and references therein). However, it is also possible that the gas remains in many discs significantly longer than a few Myr (Pfalzner et al., 2014).

After the gas dispersal, the relative velocities are no longer damped but increase by gravitational perturbations. Therefore, mutual collisions do not lead to growth but to erosion and fragmentation. Collisions between planetesimals produce smaller fragments, which in turn collide to produce even smaller fragments. This sets up a collisional cascade where planetesimals are ground down into smaller bodies, and the disc is now called a debris disc. The grinding ends with tiny, (sub)micron-sized dust grains. The size of the smallest grains can be determined by different processes related to the repelling action of stellar radiation pressure (Burns et al., 1979), the dynamical properties of planetesimals (Th ebault & Wu, 2008), or the microphysics of collisional dust production (Krijt & Kama, 2014; Pawellek & Krivov, 2015; Th ebault, 2016). The collisional cascade continuously replenishes the dust, which is removed from a debris disc by radiation pressure on timescales much shorter than the system’s age (Backman & Paresce, 1993). Thus, debris discs are also referred to as second-generation discs.

Debris discs are ubiquitous around main-sequence stars with an incidence rate of about 20...26% for FGK stars (Eiroa et al., 2013; Montesinos et al., 2016) and 24...30% for A stars (Su et al., 2006; Thureau et al., 2014), albeit these numbers are limited by

the instrument sensitivity and depend on survey strategy. Differences in the occurrence rate between FGK- and A-star samples appear to be largely due to the observed age ranges (Siegler et al., 2007; Trilling et al., 2008; Hillenbrand et al., 2008) and the typical disc decay timescales for different spectral types (e.g., Decin et al., 2003; Wyatt et al., 2007b; Kains et al., 2011). The frequency of debris discs around M stars remains controversial (Lestrade et al., 2006; Gautier et al., 2007; Forbrich et al., 2008; Plavchan et al., 2009; Lestrade et al., 2009; Greaves, 2010; Lestrade et al., 2012; Heng & Malik, 2013). Despite the high abundance of M dwarfs in the Galaxy ( $\sim 80\%$ , Lada, 2006), only a few discs around them have been detected so far.

Debris discs are known to have long lifetimes that can exceed the duration of the main-sequence phase. They have been found in very evolved systems, namely around subgiants (Bonsor et al., 2013, 2014) and white dwarfs (Wyatt et al., 2014). For the latter, the incidence rate is estimated to be at least 14% (Kilic & Redfield, 2007), and might be twice as high, as indicated by the observed fraction of metal-enriched white dwarf atmospheres (Rocchetto et al., 2015).

Although debris discs are remnants of the planet formation process, there is as yet no compelling evidence for the co-existence of planets and debris discs (Moro-Martín et al., 2007, 2015; Kóspál et al., 2009; Bryden et al., 2009; Maldonado et al., 2012; Wyatt et al., 2012; Matthews et al., 2014; Marshall et al., 2014). However, progress is made in explaining why correlations between planets, debris, and host star metallicity possibly do not exist (Fletcher & Nayakshin, 2016).

## 1.2 Insights from observations and modelling

A debris disc is detected through observations of the light emitted by circumstellar dust particles with characteristic sizes up to about 1 mm. In general, there are two types of radiation that can be detected by telescopes: scattered light and thermal emission. While the former refers to the deflection of stellar light due to the interaction with dust grains at a given wavelength, the latter is the process where dust particles absorb stellar light and re-emit it at longer wavelengths. Observations are only sensitive to the dust portion of a debris disc which forms the biggest radiating surface. Furthermore, observations are limited to a spectral range where the dust disc appears bright relative to the host star, which is typically true for the mid-infrared (mid-IR) and longer wavelengths. At these wavelengths, the dust is most effectively traced by its thermal emission seen on top of the stellar photosphere, which is referred to as IR excess. If the disc is close enough to be spatially resolved, it can be detected by imaging. This

## 1 Introduction

is not only possible at long wavelengths but also in the visible and near-IR, provided that one uses a coronagraph to block the stellar light, and therefore, to prevent the star from outshining the disc. In contrast to long-wavelength observations, visible/near-IR imaging reveals the scattered light emitted by the dust and comes with the advantage of a better angular resolution.

Over the last more than 30 years, hundreds of debris discs have been discovered by IR space missions, which are *IRAS* (Neugebauer et al., 1984), *ISO* (Kessler et al., 1996), *Spitzer* (Werner et al., 2004), *AKARI* (Murakami et al., 2007), *WISE* (Wright et al., 2010), and *Herschel* (Pilbratt et al., 2010). In addition, data are complemented by various ground-based submillimetre/millimetre facilities, e.g., IRAM (Guilloteau et al., 1992), JCMT/SCUBA (Holland et al., 1999, 2006), SEST/SIMBA (Nyman et al., 2001), CSO/SHARC (Dowell et al., 2003), SMA (Ho et al., 2004), APEX/LABOCA (Siringo et al., 2009), and ATCA (Wilson et al., 2011). Most recently, the Atacama Large Millimetre/submillimetre Array (ALMA) started working. It enables debris disc observations with unprecedented sensitivity and spatial resolution. As for scattered light, debris discs have been detected by powerful instruments belonging to various facilities, such as the W. M. Keck Observatory, the Centre for High Angular Resolution Astronomy (CHARA), the Very Large Telescope (VLT), or the *Hubble Space Telescope* (*HST*).

Most of the known debris discs are spatially unresolved and have been characterised by photometric and spectral data, which are measurements of the total flux density at a single wavelength or at various wavelengths in a narrow range. Given such a sparse data set, modelling of the spectral energy distribution (SED) of an unresolved debris disc does not result in a unique solution owing to the degeneracies between the optical properties of dust particles and the disc geometry. For example, the observed temperature, derived from an SED, can in principle be reproduced by large grains close to the star or small ones located far away (e.g., Pawellek et al., 2014). Thus, a broad SED could be the result of a broad size distribution or a broad radial distribution of the dust population. Spatially resolved discs, where the location of the dust is directly measurable, offer the best opportunities to break those degeneracies (e.g., Matthews et al., 2010; Ertel et al., 2011; Eiroa et al., 2011; Lestrade et al., 2012; Booth et al., 2013).

To date, there are more than 100 resolved debris discs from which about a few dozen are well resolved at multiple wavelengths (Pawellek, 2016). It is matter of fact that images at different wavelengths of the same disc are quite different (e.g., images of the

Fomalhaut system, Kalas et al., 2005; Acke et al., 2012). This is caused by two reasons. First, observations are mostly sensitive to the emission from grains with sizes of the same order of magnitude as the wavelength. Accordingly, optical and IR observations trace micron-sized grains, whereas observations in the (sub)millimetre probe the emission of millimetre-sized dust. Second, there is a segregation of grains according to their size due to physical mechanisms influencing the particle dynamics, such as stellar radiation pressure and Poynting-Robertson drag, which become more efficient with decreasing grain size. The disc morphology therefore changes with wavelength (Wyatt, 2006). As a consequence, a set of multi-wavelength images of the same disc provides vast information about the spatial distribution of dust particles over a wide size range.

While far-IR observations of the past decades typically revealed cold, distant dust (temperature  $T \sim 50 \dots 70$  K, distance to star  $r \sim 50 \dots 100$  au) stemming from Kuiper belt analogues, recent observations and analyses demonstrate that many discs possess a rich radial structure. Amongst the archetypes, there are the systems of Fomalhaut and Vega where dust appears to be present all the way through from more than a hundred au to the sublimation zone at a few stellar radii (e.g., Su et al., 2013; Lebreton et al., 2013). The presence of material in the cavities of the main, cold discs seems to be a rule rather than an exception. Indeed, studies of large samples of debris disc systems conclude that up to two-thirds of them show evidence for an additional warm, inner component ( $T \sim 150 \dots 200$  K,  $r \sim 1 \dots 10$  au, e.g., Hillenbrand et al., 2008; Morales et al., 2009, 2011; Ballering et al., 2013; Booth et al., 2013; Chen et al., 2014; Pawellek et al., 2014; Thureau et al., 2014; Kennedy & Wyatt, 2014; Jang-Condell et al., 2015). However, inner and outer components are not necessarily spatially separated in all systems. If a disc is unresolved, the degeneracy in SED modelling can mimic an additional dust component (Kennedy & Wyatt, 2014). Most of the reported two-component discs seem to be real and reminiscent of the Solar system with asteroid- and Kuiper-belt analogues. However, it is still uncertain whether a Solar system-like architecture is a common feature of two-component debris discs since the origin of warm dust can differ from one system to another. Currently, several scenarios providing an explanation for two-component discs are proposed in the literature and are intensively debated (Figure 1.1):

### **Scenario I: an asteroid and a Kuiper belt analogue**

This is similar to the Solar system. The warm dust emission is attributed to an inner planetesimal belt, which implies that the dust observed further in was also produced

## 1 Introduction

further in. Such a two-component configuration could be created by a set of giant planets. If giant planets succeeded to form in a radially broad protoplanetary disc, they would carve a hole in the disc by removing neighbouring dust and gas (Dipierro et al., 2016, and references therein). After the gas dispersal, nascent planets would swiftly remove planetesimals from their chaotic zones. At the same time, these planets would dynamically excite planetesimals in the zones bracketing the planetary region, preventing their further growth to full-size planets. All this can generate a broad gap in the planetary region, splitting up the disc into two distinct planetesimal belts. Even though the collisionally produced dust is spread over large distances, because of forces induced by the host star, the structure of the underlying planetesimal distribution remains that of a two-component disc. Many systems are believed to have such a two-belt configuration since their overall SEDs can be well fitted with two blackbodies (e.g., Matthews et al., 2010; Donaldson et al., 2013; Broekhoven-Fiene et al., 2013; Su et al., 2013; Steele et al., 2016; Lebreton et al., 2016, among many others). However, the presumed inner belt may have been marginally resolved for only two systems so far,  $\varepsilon$  Eridani (Greaves et al., 2014) and HD 107146 (Ricci et al., 2015a). Beside the Solar system, planets between two debris belts have been found in only one system: HR 8799 (Marois et al., 2008, 2010; Su et al., 2009). Very recently, Morrison & Kratter (2016) analysed the maximum number of unseen giant planets that can fit dynamically between two debris belts in systems belonging to the young Scorpius-Centaurus OB association. They conclude that some systems of their sample can harbour a handful of planets with several Jupiter masses, which makes them appealing targets for direct imaging campaigns.

### Scenario II: dust transport

Instead of being locally produced in an “asteroid belt”, warm dust may be transported inward from outer production zones by Poynting-Robertson and stellar wind drag. For low-density systems, where collisional timescales are longer than the transport timescales, the inner disc region is filled by dust, leading to a nearly uniform density profile (Wyatt, 2005b; Kennedy & Piette, 2015). This scenario is able to explain the observed emission of discs around late-type stars such as  $\varepsilon$  Eri (Reidemeister et al., 2011). However, this may not be a viable alternative for discs around stars with spectral types earlier than  $\sim$ F5 for which no strong coronal winds are expected (Lamers & Cassinelli, 1999).



### Scenario III: very eccentric planetesimal population

As shown by Wyatt et al. (2010), an outer planetesimal swarm with very high orbital eccentricities can be responsible for warm dust in the inner region of a system. Since the planetesimals are in highly eccentric orbits, they spend most of the time in apocentric regions, where collisions are rare. Conversely, the majority of the collisions, and therefore, an efficient dust production takes place during the pericentre passages, because of an enhanced particle density and higher relative velocities. A system with such a quasi-cometary planetesimal population can generate a long-lived warm dust component. However, explaining the origin of such a high eccentricity population remains challenging. Planetary migration and scattering are suggested as plausible reasons (Payne et al., 2009; Bonsor & Wyatt, 2012).

### Scenario IV: recent heavy collision

The observed warm dust might be an aftermath of a recent major collision between two big planetesimals in the inner region (Grigorieva et al., 2007a). Such a major breakup is a stochastic event and provides a large amount of dust that renders the inner region atypically bright for a short period of time ( $\sim 1$  Myr, Kral et al., 2015). However, the frequency of heavy collisions goes down as the number of asteroidal bodies in the inner system decreases because of collisional depletion. Thus, this scenario only seems to be feasible for young systems.<sup>2)</sup>

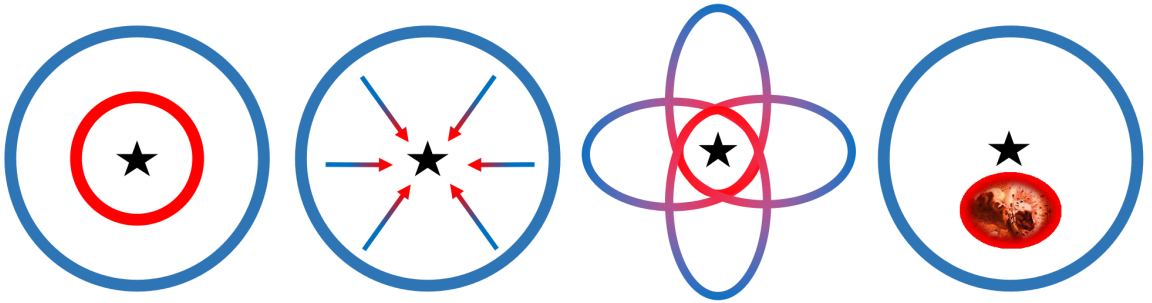


**Figure 1.1:** Cartoons of four scenarios explaining the presence of warm (red) and cold (blue) dust in debris discs. *From left to right:* asteroid-plus-Kuiper-like belt configuration, transport of warm dust from an outer Kuiper-like belt, disc of eccentric planetesimals, heavy collision between massive bodies in the inner system. Thick lines depict planetesimal belts, arrows the dust transport.

<sup>2)</sup>Moreover, in young systems the dust production is not necessarily limited to planetesimals. Collisions between protoplanets during the terrestrial planet formation can also release a large amount of dust in the inner region (Jackson & Wyatt, 2012; Genda et al., 2015).

### 1.3 Collisional versus classic modelling

When it comes to modelling of debris disc observations, a classic approach is often used that is based on analytic functions to describe the distribution of circumstellar dust. Usually, a combination of two independent power laws is assumed for the size and the spatial distribution of the dust (e.g., Ertel et al., 2012a). This choice is motivated by the shape of the size distribution set by collisional equilibrium (Dohnanyi, 1969; Tanaka et al., 1996), and the shape of the radial brightness profiles extracted from images of resolved debris discs (e.g., Thébault & Wu, 2008). In such models, the most important parameters are the slopes of the size and the radial distribution, the lower and upper grain size cutoff, the radial extent of the dust disc, and the dust mass. By fitting, it is easy to explore a huge parameter space in a relatively short time and to adapt the model parameters to observables like SEDs and surface brightness profiles. Results can be compared to findings of many other publications, which use similar approaches. However, classic models do not consider physical mechanisms that drive the dynamical and the collisional evolution of dust and planetesimals. In reality, size and spatial distributions of the circumstellar material significantly depart from power laws and are coupled to each other in an intricate way (e.g., Campo Bagatin et al., 1994; Durda & Dermott, 1997; Thébault & Augereau, 2007). Furthermore, there is no link between the dust distribution and the dust-producing parent bodies. Therefore, classic models cannot access the parameters of planetesimals (mass, location, orbital eccentricities, etc.) and only address the two uppermost levels in Figure 1.2.

To overcome the problems of classic methods, an alternative modelling approach is needed, which can be referred to as debris disc modelling “from the sources”. Here, the basic idea is to start with an initial distribution of planetesimals and to model its subsequent collisional evolution by calculating the production and loss of material in a collisional cascade. The dust distribution as a function of time can be determined in this way. In the recent years, collisional codes necessary for this purpose have been developed. They are either based on purely statistical methods (Thébault et al., 2003; Thébault & Augereau, 2007; Kenyon & Bromley, 2004b; Gáspár et al., 2012; van Lieshout et al., 2014), or include a combination of  $N$ -body simulations and particle-in-a-box models (Kral et al., 2013; Nesvold et al., 2013) to connect particle dynamics and collisions (Thébault, 2012). These approaches provide coupled size and spatial distributions for the whole population of objects in a debris disc, ranging from planetesimals down to dust grains. In a second step, thermal emission and scattered light models are applied to compute the resulting dust emission that is compared with

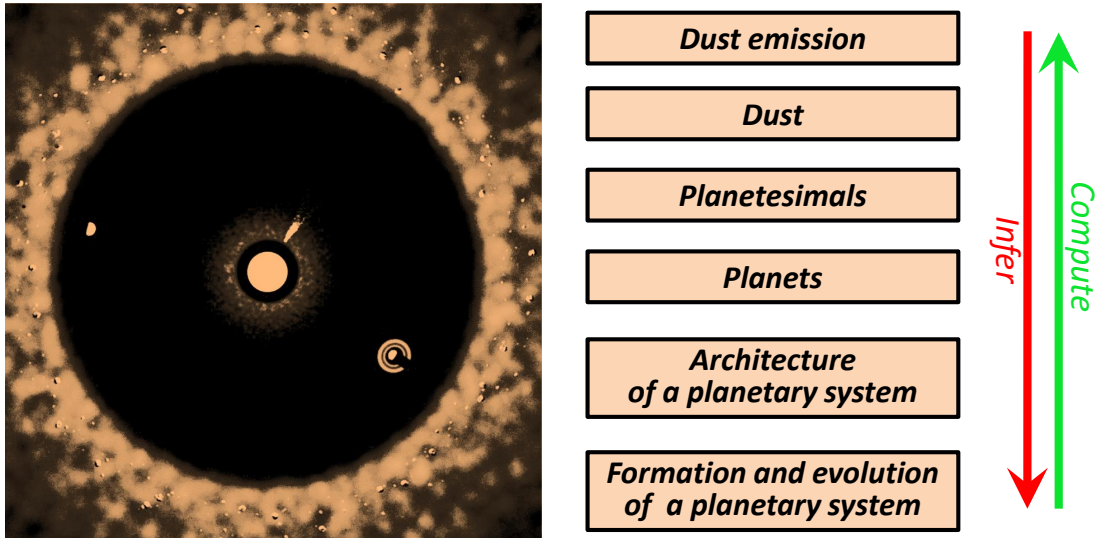


**Figure 1.2:** Schematic illustrating the methodology of debris disc studies. The boxes on the right show the links from the directly observable quantities (the uppermost level) to the most fundamental properties of planetary systems (the lowermost one). Image courtesy of A. V. Krivov.

observations. An adaption of the model to observables means to find an appropriate dust distribution, which can only be found by variations of the planetesimal parameters. Thus, collisional modelling allows constraining properties of planetesimals. It goes at least one level deeper than classic approaches in terms of Figure 1.2. There is also a chance that even more fundamental properties of planetary systems can be deduced from the planetesimal distribution computed by collisional modelling. These include, e.g., the presence of yet undetected planets that work as sculptors of the planetesimal belts (level 4 in Figure 1.2). Gaps or sharp edges in the radial planetesimal distribution may hint at the locations where planet formation or migration removed planetesimals or prevented their formation. Although collisional modelling provides a more complete picture of debris discs, the price to pay is the numerical complexity so that only a limited number of parameter combinations can be explored.

## 1.4 Aims of this work

The main goal of this work is to infer properties of dust and dust-producing planetesimal populations in selected debris disc systems by in-depth collisional modelling. These properties include the chemical composition and typical sizes of the dust grains, as well as the location, radial distribution, and dynamical excitation of the planetes-

## 1 Introduction

imals. Furthermore, the work intends to make predictions of the presence of hidden perturbers such as alleged planets that dynamically sculpt and stir planetesimal belts.

To this end, a numerical code, named **ACE**, is used to model the collisional evolution of debris discs. The code follows a statistical approach to solve the kinetic equation, which includes the combined effects of stellar gravity, mutual non-elastic collisions, and forces exerted by stellar radiation and stellar winds on circumstellar dust particles. A first description of the kinetic model implemented in **ACE** is presented by Krivov et al. (2000). Since then, the numerical implementation has been developed further and maintained by T. Löhne and A. V. Krivov in Jena. In the recent years, the code was employed for studies of the Solar system (Vitense et al., 2010, 2012) and several extrasolar systems (Krivov et al., 2008, 2013; Müller et al., 2010; Reidemeister et al., 2011; Löhne et al., 2012). These works show that the collisional modelling method is able to provide valuable information on planetesimals, and allows for constraining the architecture, formation, and evolution of planetary systems. Furthermore, the studies revealed very different properties of debris discs, e.g. with respect to their collisional activity. For instance, the planetesimals in the Vega disc are likely to have a maximum orbital eccentricity in the order of 0.1, which results in high impact velocities and an effective production of small dust (Müller et al., 2010). In contrast, *Herschel*'s “cold discs” show evidence for a low amount of material in grains smaller than 1 mm, which implies eccentricities as low as  $\sim 0.001$  (Krivov et al., 2013).

Continuing the previous works, this thesis focuses on three further systems: HIP 17439, AU Microscopii, and  $\alpha^1$  Eridani. All three are excellent candidates for in-depth collisional modelling since they have bright, spatially resolved debris discs for which a great abundance of observational data is available. These include densely-sampled SEDs and images at optical, IR, and submillimetre/millimetre wavelengths. Furthermore, they are chosen because they are remarkable in one or another respect, which is explained in dedicated chapters for each system.

Chapter 2 outlines the basic physical processes working in debris discs and shows the way how these processes are incorporated in a kinetic model. This chapter also addresses the interaction between dust grains and stellar light, and presents the numerical tools used to predict observables. Chapter 3 contains our analysis of the HIP 17439 system (Schüppler et al., 2014), followed by a work about the AU Mic disc in Chapter 4 (Schüppler et al., 2015). In Chapter 5, a long-term collisional evolution of a two-component system is described and a specific application is made to the disc around  $\alpha^1$  Eri (Schüppler et al., 2016). Finally, a summary of conclusions is given in Chapter 6.

# 2 Fundamentals

## 2.1 Keplerian motion and orbital elements

Circumstellar objects revolve around their primary in Keplerian orbits. Given Newton's law of gravity

$$\vec{F}_g = -G \frac{m M_\star}{r^3} \vec{r}, \quad (2.1)$$

where  $G$  is the gravitational constant and  $\vec{r}$  the distance vector from the stellar mass  $M_\star$  to the mass  $m$  of a revolving body, the derivation of the absolute distance between the two masses yields

$$r = \frac{p}{1 + e \cos \varphi}. \quad (2.2)$$

Here,  $e$  denotes the eccentricity and  $\varphi$  the true anomaly, which is the angle between the pericentre, i.e. the position of the minimum distance between the two masses, and the current position of mass  $m$  relative to  $M_\star$ . The parameter  $p$  is called semi-latus rectum. Depending on the orbital energy, we can distinguish three types of orbits:

1. ellipses for  $0 \leq e < 1$ ,  $p = q(1 + e)$ , and  $q = a(1 - e)$ ,
2. parabolas for  $e = 1$  and  $p = 2q$ ,
3. hyperbolas for  $e > 1$ ,  $p = q(e - 1)$ , and  $q = a(1 + e)$ ,

where  $a$  denotes the semi-major axis and  $q$  the pericentric distance.

The orbital elements  $a$ ,  $e$ , and  $\varphi$  define the current position of an object in the orbital plane. To describe a Keplerian orbit in three dimensions, additional orbital elements are needed. These can be the inclination  $i$ , which is the angle between the orbital plane and a reference plane, the longitude of the ascending node  $\Omega$ , which is the orientation of the intersection line of both planes (line of nodes) with respect to a reference direction, and the argument of pericentre  $\omega$ , which is the angle between the ascending node and the pericentre. This set of elements is not the only possible choice, but best suited to describe the dynamical problems presented in the following sections.

## 2.2 Physical processes in debris discs

### 2.2.1 Collisions

Destructive collisions are an important process operating in debris discs and responsible for the production of collisional debris. This is in contrast to their progenitors, the protoplanetary discs, where a large amount of gas (Hildebrand, 1983) damps the relative velocities in the discs, and collisions therefore result in bouncing or sticking (Blum & Wurm, 2008). However, the primordial gas is removed within a few Myr after the birth of the protostar. As a consequence, gas-poor systems remain where damping is not efficient. Although this provides the necessary condition for high relative velocities, destructive collisions only occur if they are ignited by stirring, i.e. a mechanism that pushes planetesimals on more eccentric and inclined orbits. This can be self-stirring, where the gravitational perturbation of the largest disc bodies starts to excite the orbits of the surrounding bodies (Kenyon & Bromley, 2004a, 2008), or planet stirring, where planets orbiting inside the inner edge of the disc stir it through long-distant, secular perturbations (Wyatt, 2005a; Mustill & Wyatt, 2009). External events like stellar flybys (Kenyon & Bromley, 2002) or a stellar-mass companion in an eccentric or inclined orbit (Th ebault et al., 2010; Th ebault, 2012; Nesvold et al., 2016) can also be responsible for stirring. The stirring marks the beginning of the collisional evolution of the disc where kilometre-sized planetesimals are ground to dust sizes ( $< 1$  mm) in a collisional cascade.

In a collision of two particles, both colliders are disrupted if their impact velocity,  $v_{\text{imp}}$ , exceeds the critical value

$$v^* = \sqrt{2 \frac{(m_p + m_t)^2}{m_p m_t} Q_D^*}, \quad (2.3)$$

where  $m_p$  and  $m_t$  being the masses of projectile and target respectively. The quantity  $Q_D^*$  is the critical energy for fragmentation and dispersal per total mass,  $m_p + m_t$ . This specific energy is needed to disperse a particle into fragments with the largest fragment containing at most half the total mass. Numerical experiments show that  $Q_D^*$  depends on the particle sizes and the impact velocity (Benz & Asphaug, 1999; Stewart & Leinhardt, 2009). The material strength is mainly determined by inter-molecular sticking forces (e.g., van-der-Waals bindings) for objects smaller than  $\sim 100$  m, while

self-gravity dominates for larger sizes. Thus,  $Q_D^*$  can be written as the sum of two power laws

$$Q_D^* = \left[ Q_{D,s} \left( \frac{s}{1 \text{ m}} \right)^{b_s} + Q_{D,g} \left( \frac{s}{1 \text{ km}} \right)^{b_g} \right] \left( \frac{v_{\text{imp}}}{3 \text{ km s}^{-1}} \right)^\kappa, \quad (2.4)$$

where  $(Q_{D,s}, b_s)$  and  $(Q_{D,g}, b_g)$  are pairs of constants, which characterise the strength and gravity regime. The results of this thesis were computed with material parameters which follow the Benz & Asphaug (1999) basalt and which are close to the values presented by many authors (Farinella et al., 1982; Davis et al., 1985; Housen & Holsapple, 1990; Housen et al., 1991; Ryan, 1992; Holsapple, 1994; Melosh & Ryan, 1997; Love & Ahrens, 1996; Benz, 2000; Leinhardt & Stewart, 2009; Jutzi et al., 2010). More precisely, we assumed  $b_s = -0.37$  and  $b_g = 1.38$ , while the  $Q_D$ 's were varied in the ranges  $5 \dots 10 \times 10^6 \text{ erg g}^{-1}$  for  $Q_{D,s}$  and  $5 \dots 20 \times 10^6 \text{ erg g}^{-1}$  for  $Q_{D,g}$ . The velocity exponent  $\kappa$  is a material constant, which was set to 0.5 (Stewart & Leinhardt, 2009).

Laboratory measurements show that the mass of the largest fragment produced in disruptive collisions is

$$m_x = \frac{1}{2} (m_p + m_t) \left( 2 \frac{(m_p + m_t)^2}{m_p m_t} \frac{Q_D^*}{v_{\text{imp}}^2} \right)^c. \quad (2.5)$$

Fujiwara et al. (1977) measured  $c \approx 1.24$  for basalt while Arakawa (1999) obtained  $c \approx 0.91$  for ice. However, there are some uncertainties since the results from Benz & Asphaug (1999) indicate lower values for basalt and higher ones for ice. We assumed  $c = 1$  for the studies shown in this thesis.

If  $v_{\text{imp}} < v^*$ , the impact energy is not sufficient to destroy the bulk of the colliders. However, some parts of the material can be excavated, leading to the ejection of fragments, which is called cratering. According to the models of Wyatt & Dent (2002) and Thébault & Augereau (2007), the ejected mass in such a collisional event reads

$$m_{\text{crat}} = \frac{1}{4} \frac{m_p m_t}{m_p + m_t} \frac{v_{\text{imp}}^2}{Q_D^*}. \quad (2.6)$$

This relation originally considers the production of large craters, comparable with the size of the targets. Löhne (2015) shows that the excavated mass of small-scale craters has approximately the same dependence on the impact energy as for large craters if  $b_s$  is close to zero.

The outcome of disruptive and cratering collisions can be described with the mass

## 2 Fundamentals

distribution of fragments (Krivov et al., 2005) given by

$$g(m) = (2 - \eta) \left( \frac{m}{m_x} \right)^{-\eta} \frac{m_{\text{frag}}}{m_x^2}, \quad (2.7)$$

where  $g(m) dm$  is the number of fragments within  $[m, m + dm]$  for  $m \leq m_x$ , and  $m_{\text{frag}}$  denotes the total mass of all fragments. Depending on the collisional type, we have  $m_{\text{frag}} = m_p + m_t$  for disruption or  $m_{\text{frag}} = m_{\text{crat}}$  for cratering. Equation (2.7) is a simplification since the fragment distribution is assumed to follow a single-exponent power law, which may not reflect the complex collisional physics. However, a more realistic bimodal fragment distribution, supported by experimental and theoretical studies, does only moderately affect the resulting overall size distribution in collisional equilibrium (Thébault et al., 2003). Thus, the choice of a single power-law fragment distribution is reasonable.

The mass  $m_x$  for cratering follows from the assumption that there is only one body among the ejected fragments which is the largest:

$$\int_{m_x}^{\infty} g(m) dm = \frac{2 - \eta}{\eta - 1} \frac{m_{\text{frag}}}{m_x} \stackrel{!}{=} 1. \quad (2.8)$$

Equation (2.8) holds for  $\eta > 1$ . In fact, the index of the mass distribution is in the range  $\eta = 1.5 \dots 2$  (Fujiwara, 1986, and references therein).

Collisions will end up in sticking and agglomeration at very low impact velocities ( $v_{\text{imp}} \lesssim 10 \text{ m s}^{-1}$ , Blum & Wurm, 2008). Except for some few peculiar systems (Krivov et al., 2013), this is not expected for “canonical” debris discs. No sticking collisions are considered throughout this work.

### 2.2.2 Pressure forces

Small particles in a debris disc experience pressure forces, which are directed radially outwards, because of the absorption of stellar photons (in case of radiation pressure) and charged particles (in case of stellar wind pressure). Since both forces are proportional to  $r^{-2}$ , one defines distance-independent ratios through

$$\beta_{\text{rp}} = \frac{|\vec{F}_{\text{rp}}|}{|\vec{F}_{\text{g}}|}, \quad \beta_{\text{sw}} = \frac{|\vec{F}_{\text{sw}}|}{|\vec{F}_{\text{g}}|}, \quad (2.9)$$

where  $\vec{F}_{\text{rp}}$  and  $\vec{F}_{\text{sw}}$  are the direct radiation and stellar wind pressure forces, respectively. Under the assumption that the particles are compact spheres with radius  $s$  and bulk



density  $\rho$ , the  $\beta$  ratios can be expressed by

$$\beta_{\text{rp}} = \frac{3}{16\pi} \frac{L_\star}{G M_\star c \rho} \frac{Q_{\text{rp}}}{s}, \quad \beta_{\text{sw}} = \frac{3}{16\pi} \frac{\dot{M}_\star v_{\text{sw}} C_{\text{D}}/2}{G M_\star \rho s}, \quad (2.10)$$

which follows Burns et al. (1979) and Gustafson (1994). Here,  $L_\star$  is the stellar luminosity,  $c$  the speed of light,  $v_{\text{sw}}$  the speed of stellar wind particles, and  $\dot{M}_\star$  the stellar mass-loss rate.<sup>3)</sup> The quantities  $Q_{\text{rp}}$  and  $C_{\text{D}}$  are measures of the momentum transfer from a photon or a stellar wind particle to a dust grain and also depend on the grain radius  $s$ .

In case of spherical particles, Mie's (1908) calculations provide the analytic solution

$$Q_{\text{rp}} = \langle Q_{\text{abs}} + (1 - g)Q_{\text{sca}} \rangle, \quad (2.11)$$

where  $Q_{\text{abs}}$  and  $Q_{\text{sca}}$  are the efficiencies for absorption and scattering. The asymmetry parameter  $g$  indicates whether a particle scatters isotropically ( $g = 0$ ), or more light towards the forward ( $0 < g \leq 1$ ) or backward ( $-1 \leq g < 0$ ) direction. The angle brackets in Equation (2.11) mean averaging over the wavelength of light, weighted by the stellar flux.<sup>4)</sup> If a particle is a perfect absorber, i.e. a blackbody,  $Q_{\text{rp}} = 1$ . This is also a good approximation for non-blackbody absorbers as long as the particle size is large compared to the peak wavelength of the stellar spectrum. To specify  $C_{\text{D}}$ , we assume the reflection of stellar wind particles on the surface of dust grains, resulting in  $C_{\text{D}} = 2$  (Mukai & Yamamoto, 1982).

Typical  $\beta$  ratios for stars of different spectral types and with different values of  $\dot{M}_\star$ , as a measure of the stellar wind strength, are depicted in Figure 2.1. The mass-loss rates are given in terms of multiples of the solar mass-loss rate,  $\dot{M}_\odot = 2 \times 10^{-14} M_\odot \text{ yr}^{-1}$  (Feldman et al., 1977). The pressure forces counteract the stellar gravity and effectively reduce  $\vec{F}_{\text{g}}$  by a factor of  $(1 - \beta_{\text{rp}} - \beta_{\text{sw}})$ . Since  $\beta$  ratios include a  $1/s$  dependence, the smallest dust grains are mostly affected by the pressure forces. In a debris disc, the orbits of collisionally produced fragments become more and more eccentric with decreasing fragment size, or equivalently, increasing  $\beta$  ratios (Burns et al., 1979). If fragments are released from parent bodies on circular orbits, the eccentricities of the fragments exceed 1 for  $\beta_{\text{rp}} + \beta_{\text{sw}} > 0.5$ , and the fragments leave the system on hyperbolic trajectories. Accordingly, the value  $\beta_{\text{rp}} + \beta_{\text{sw}} = 0.5$  is referred to as the blowout limit

<sup>3)</sup>Owing to radial variations in the stellar wind speed,  $\beta_{\text{sw}}$  is still dependent on  $r$ . However, this dependence was shown to be weak (Augereau & Beust, 2006). Therefore,  $\beta_{\text{sw}}$  is treated as a constant with distance from the star in this work.

<sup>4)</sup>In formula:  $\langle Q \rangle = \int_\lambda Q F_\lambda(T_\star) d\lambda / \int_\lambda F_\lambda(T_\star) d\lambda$ , where  $F_\lambda(T_\star)$  is the stellar spectrum.

## 2 Fundamentals

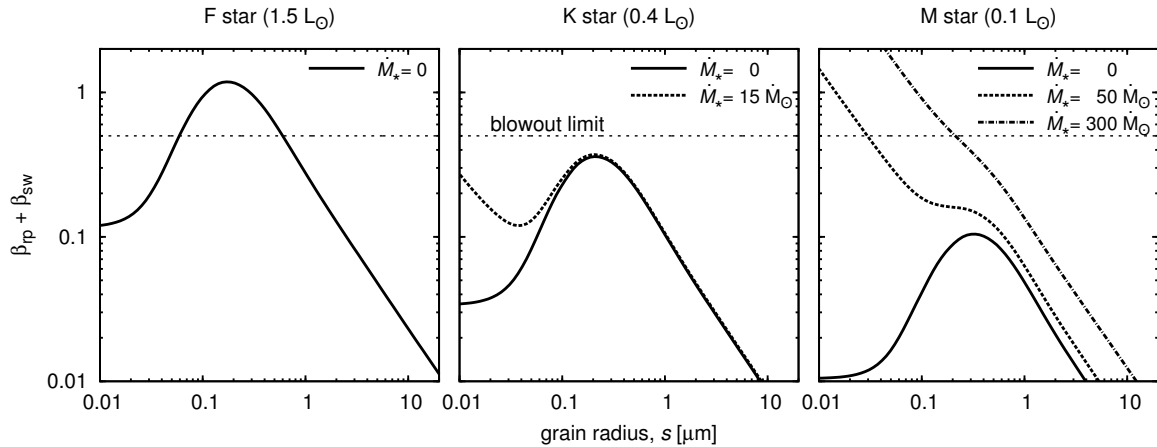


**Figure 2.1:** Dependence of  $\beta_{\text{rp}} + \beta_{\text{sw}}$  on  $s$  for dust around stars of different spectral types and with different values of the stellar mass-loss rate  $\dot{M}_*$ . There is no stellar wind pressure for  $\dot{M}_* = 0$  because it implies  $\beta_{\text{sw}} = 0$ . Dust grains were made of pure astronomical silicate (Draine, 2003). The stellar wind speed was set to  $400 \text{ km s}^{-1}$ .

and the corresponding particle size is named blowout radius  $s_{\text{blow}}$ .<sup>5)</sup>

If the star has a sufficiently high luminosity, a blowout limit will be reached by radiation pressure, as illustrated in the F-star panel of Figure 2.1. This is not the case for the two later spectral types shown, where radiation pressure is too weak. However, late-type stars are likely to possess coronal-driven stellar winds (e.g., Lamers & Cassinelli, 1999; Wood, 2004), which can yet expel micron-sized grains. Even in systems where no blowout limit exists by radiative or corpuscular forces, the tiniest grains are eliminated through other mechanisms. These can be additional dynamical effects, as described in Section 2.2.4, or various erosive processes, like photo-sputtering (Grigorieva et al., 2007b) or stellar wind sputtering (Czechowski & Mann, 2010). In addition, the microphysical surface energy constraint can limit the size of the smallest collisional fragments (Krijt & Kama, 2014).

### 2.2.3 Drag forces

Owing to the aberration effect, a dust grain orbiting a star “sees” the incoming stellar radiation and the stellar wind from a slightly forward direction. Accordingly, a part of the momenta from the stellar photons and wind particles is transferred to the moving

<sup>5)</sup>If fragments are released from eccentric orbits, the blowout occurs somewhere between  $\beta_{\text{rp}} + \beta_{\text{sw}} = (1 - e)/2$  at the periastron and  $(1 + e)/2$  at the apastron (Burns et al., 1979), where  $e$  is the typical eccentricity of the parent bodies that eject the dust. Throughout this work, parent planetesimals are not assumed to be on highly eccentric orbits. Thus,  $\beta_{\text{rp}} + \beta_{\text{sw}} = 0.5$  serves as a good criterion to define the blowout size.

dust grain that leads to forces against the direction of its orbital motion (“headwind”). These forces are known as Poynting-Robertson drag (P-R force or P-R effect, Poynting, 1904; Robertson, 1937) and stellar wind drag

$$\vec{F}_{\text{PR}} = -|\vec{F}_g| \frac{\beta_{\text{rp}}}{c} \left( \frac{\vec{r} \cdot \vec{v}}{r} \frac{\vec{r}}{r} + \vec{v} \right), \quad \vec{F}_{\text{sw}} = -|\vec{F}_g| \frac{\beta_{\text{sw}}}{v_{\text{sw}}} \left( \frac{\vec{r} \cdot \vec{v}}{r} \frac{\vec{r}}{r} + \vec{v} \right), \quad (2.12)$$

where  $\vec{v}$  is the velocity vector of the dust particle.

Like the pressure forces, the drag forces increase with decreasing particle size. The stellar wind drag can be much stronger than the P-R drag because of  $v_{\text{sw}} < c$ . The drag forces cause a particle to gradually lose angular momentum. It thus spirals slowly towards the star by reducing its semi-major axis and eccentricity (Wyatt & Whipple, 1950). Assuming a particle starts from a circular orbit at distance  $r$ , the timescale to spiral inwards is

$$T_{\text{transport}} = \frac{r^2}{4G M_\star} \frac{c}{\beta_{\text{rp}}} \left( 1 + \frac{\beta_{\text{sw}}}{\beta_{\text{rp}}} \frac{c}{v_{\text{sw}}} \right)^{-1}. \quad (2.13)$$

Summing up, the total force, including gravity, pressure and drag effects, working on a circumstellar particle, can be written as

$$\vec{F}_{\text{total}} = (1 - \beta_{\text{rp}} - \beta_{\text{sw}}) \vec{F}_g - |\vec{F}_g| \left( \frac{\beta_{\text{rp}}}{c} + \frac{\beta_{\text{sw}}}{v_{\text{sw}}} \right) \left( \frac{\vec{r} \cdot \vec{v}}{r} \frac{\vec{r}}{r} + \vec{v} \right). \quad (2.14)$$

### 2.2.4 Other forces

Circumstellar dust grains can be charged, e.g. due to the emission of photo-electrons, when they are irradiated by stellar light, or due to the capture of ions from the stellar wind (Wyatt, 1969; Horanyi, 1996; Kimura & Mann, 1998). The grains therefore experience the Lorentz force induced by stellar or planetary magnetic fields. This causes changes of their orbital elements, which have been intensively investigated for the Solar system (Morfill & Grün, 1979; Consolmagno, 1980; Barge et al., 1982; Wallis & Hassan, 1985). The Lorentz force mostly affects only small grains  $\lesssim 0.1 \mu\text{m}$  in size (Leinert & Grün, 1990). Furthermore, it plays only a dominant role in close vicinity of the magnetic field sources (Czechowski & Mann, 2010). Thus, close-in, very small grains – known as hot or exozodiacal dust (Absil et al. 2013; Ertel et al. 2014a; Mennesson et al. 2014; Kirchschrager et al., submitted) – can be trapped in stellar magnetic fields (Su et al., 2013; Rieke et al., 2016). Beside forces on dust, some additional forces

## 2 Fundamentals

exist that influence the dynamics of larger objects, e.g. related to their rotation and anisotropic thermal emission (Yarkovsky effect, “rediscovered” by Öpik, 1951). The interstellar medium flow can also affect the dust distribution, which has been identified for a couple of debris discs (e.g., Artymowicz & Clampin, 1997; Debes et al., 2009; Maness et al., 2009; Buenzli et al., 2010). However, all these forces seem to have no generic relevance for the debris discs discussed in this thesis, and we did not take them into account in the modelling.

### 2.2.5 Planetary perturbations

Planets, which are the most massive objects in a debris disc, can gravitationally interact with the disc. One effect, induced by such an interaction, is stirring, mentioned in Section 2.2.1. Other effects are the formation of gaps, offsets between the disc and the star, or warping and clumping the disc. While warps, which are variations in the disc inclination with distance from the star, could be due to secular perturbations caused by planets in inclined orbits (Mouillet et al., 1997; Augereau et al., 2001), clumps likely arise from the capture of disc objects into mean-motion resonances (Wyatt, 2006; Krivov et al., 2007). Observations of such features in the dust distribution provide strong evidence of the presence of unseen planets (e.g., Ertel et al., 2012b). A prominent example is the  $\beta$  Pic disc, where an observed warp within  $\approx 100$  au (first reported by Burrows et al. 1995, confirmed with high-resolution images by Golimowski et al. 2006) gave reason to the prediction of a planetary companion, which was subsequently found (Lagrange et al., 2010).

## 2.3 Kinetic theory

The following sections briefly summarise the statistical approach of kinetic theory and its numerical implementation described in Krivov et al. (2000, 2005, 2006, 2013), Löhne (2008), and Löhne et al. (2008, 2012).

### 2.3.1 General description

We consider an ensemble of circumstellar objects that is fully characterised by the distribution function  $n(m, \vec{p})$ , where  $\vec{p}$  is a vector of orbital elements. This means that  $n(m, \vec{p}) dm d\vec{p}$  is the number of particles with arguments  $[m, m + dm]$  and  $[\vec{p}, \vec{p} + d\vec{p}]$  present in a debris disc at certain instant of time  $t$ . For brevity, the argument  $t$  will be omitted, but is always implied, also in all quantities derived from the distribution

function. Changes of  $n(m, \vec{p})$  are calculated with the master equation (Krivov et al., 2000):

$$\frac{d}{dt}n(m, \vec{p}) = \left( \frac{\partial}{\partial t}n(m, \vec{p}) \right)_{\text{gain}} - \left( \frac{\partial}{\partial t}n(m, \vec{p}) \right)_{\text{loss}} - \text{div} \left( n(m, \vec{p}) \frac{d}{dt}\vec{p} \right). \quad (2.15)$$

The right-hand side balances the gain and loss of  $n(m, \vec{p})$  as a result of two-particle collisions. There is also a divergence term that reflects the diffusion process through transport mechanisms (P-R and stellar wind drag).<sup>6)</sup> The gain and loss terms can be expressed as follows

$$\begin{aligned} \left( \frac{\partial}{\partial t}n(m, \vec{p}) \right)_{\text{gain}} &= \int_{m_p} \int_{m_t} \int_{\vec{p}_p} \int_{\vec{p}_t} f(m_p, \vec{p}_p; m_t, \vec{p}_t; m, \vec{p}) \\ &\quad \times n(m_p, \vec{p}_p) n(m_t, \vec{p}_t) v_{\text{rel}}(m_p, \vec{p}_p; m_t, \vec{p}_t) \\ &\quad \times \sigma(m_p, m_t) \delta(\vec{r}(\vec{p}_p) - \vec{r}(\vec{p}_t)) dm_p dm_t d\vec{p}_p d\vec{p}_t, \end{aligned} \quad (2.16)$$

$$\begin{aligned} \left( \frac{\partial}{\partial t}n(m, \vec{p}) \right)_{\text{loss}} &= n(m, \vec{p}) \int_{m_p} \int_{\vec{p}_p} n(m_p, \vec{p}_p) v_{\text{rel}}(m_p, \vec{p}_p; m, \vec{p}) \\ &\quad \times \sigma(m_p, m) \delta(\vec{r}(\vec{p}_p) - \vec{r}(\vec{p})) dm_p d\vec{p}_p, \end{aligned} \quad (2.17)$$

where one has to integrate over properties of the colliding particles, namely projectiles (subscript p) and targets (subscript t). The fragment-generating function is defined in such a way that  $f(m_p, \vec{p}_p; m_t, \vec{p}_t; m, \vec{p}) dm d\vec{p}$  is the number of fragments with  $[m, m + dm]$  and  $[\vec{p}, \vec{p} + d\vec{p}]$ , produced through a collision of particles with properties  $(m_p, \vec{p}_p)$  and  $(m_t, \vec{p}_t)$ . The collisional cross-section of both colliders is denoted with  $\sigma(m_p, m_t)$ , and the relative velocity with  $v_{\text{rel}}(m_p, \vec{p}_p; m_t, \vec{p}_t)$ . The integrands are evaluated at collisions, as indicated by Dirac's  $\delta$ .

The collisional cross-section is basically composed of the geometrical cross-sections of projectile and target. This is enhanced for larger objects because of the mutual gravitational interaction (Safronov's factor), which results in

$$\sigma(m_p, m_t) = \pi \left( \frac{3}{4\pi\rho} \right)^{2/3} \left( m_p^{1/3} + m_t^{1/3} \right)^2 \left( 1 + \frac{v_{\text{esc}}^2}{v_{\text{rel}}^2} \right) \quad (2.18)$$

with  $v_{\text{esc}}^2 = 2G(m_p + m_t)/(s_p + s_t)$ .

---

<sup>6)</sup>Without the divergence term, (2.15) is also referred to as Smoluchowski-Boltzmann equation (Boltzmann, 1896; Smoluchowski, 1916).

## 2 Fundamentals

The fragment-generating function is the product of two distributions:

$$f(m_p, \vec{p}_p; m_t, \vec{p}_t; m, \vec{p}) = g(m) h(m_p, \vec{p}_p; m_t, \vec{p}_t; m, \vec{p}), \quad (2.19)$$

where  $g(m)$  is the fragment mass distribution, defined in Equation (2.7), and  $h(m_p, \vec{p}_p; m_t, \vec{p}_t; m, \vec{p})$  is the distribution of orbital elements of the fragments. The latter ensures that fragments of mass  $m$ , produced by collisions between the particles  $(m_p, \vec{p}_p)$  and  $(m_t, \vec{p}_t)$ , have the orbital elements  $\vec{p}$ , or symbolically

$$h(m_p, \vec{p}_p; m_t, \vec{p}_t; m, \vec{p}) \propto \delta(\vec{p} - \vec{p}(m_p, \vec{p}_p; m_t, \vec{p}_t; m)). \quad (2.20)$$

In analogy to the transport timescale (Equation 2.13), a characteristic lifetime of particles against collisional depletion can be defined as follows:

$$T_{\text{collision}} = n(m, \vec{p}) \left( \frac{\partial}{\partial t} n(m, \vec{p}) \right)_{\text{loss}}^{-1}. \quad (2.21)$$

### 2.3.2 Implementation: the ACE code

To model the collisional evolution of a debris disc, Equation (2.15) has to be solved numerically. For this purpose, a C++-based code, named **ACE** (**A**nalysis of **C**ollisional **E**volution), has been developed (mainly at the AIU Jena) for more than 10 years.

The **ACE** version used for the work presented in this thesis considers rotationally-symmetric debris discs. This implies that particles are uniformly distributed with respect to their angular elements  $\Omega$ ,  $\omega$ , and  $\varphi$ . In addition, it is assumed that the distribution of orbital inclinations is uniform within a semi-opening angle  $\varepsilon$ . The phase-space density of such idealised discs can be written as

$$n(m, q, e) = \int_0^\varepsilon \int_0^{2\pi} \int_0^{2\pi} \int_0^{2\pi} n(m, q, e, i, \Omega, \omega, \varphi) d\varphi d\omega d\Omega di, \quad (2.22)$$

which should be understood as a distribution function in terms of object mass  $m$ , pericentric distance  $q$ , and orbital eccentricity  $e$  averaged over the “unimportant” elements  $\Omega$ ,  $\omega$ ,  $\varphi$ , and  $i$ . Averaging over the true anomaly is, in particular, justified by the physical nature of debris discs, where collisional lifetimes of circumstellar particles are usually significantly longer than their orbital periods. Collisions are therefore randomised with respect to  $\varphi$ .

The simplifications described above reduce the phase space to three dimensions and keep simulations at a computationally affordable level. However, this comes along with the restriction that no azimuthal and vertical asymmetries, e.g., caused by planetary perturbers (see Section 2.2.5), can be modelled.<sup>7)</sup>

**ACE** works on a logarithmic grid for  $m$ ,  $q$ , and  $e$ . It uses an exponential Euler integrator to solve Equation (2.15) and considers disruptive and erosive collisions. The latter include two cases: 1. collisions where the projectile is disruptive and the target is cratered (denoted as cratering), and 2. collisions where the projectile is cratered and the target stays intact (denoted as rebounding). Beside collisions, the particles experience the combined effect of gravity, pressure and drag forces as described by Equation (2.14). Once  $n(m, q, e)$  is calculated, **ACE** transforms it to the spatial number density  $N(m, r)$ , which is the number of particles per unit volume in  $[m, m+dm]$  at a distance  $r$  from the star ( $[N(m, r)] = \text{g}^{-1} \text{cm}^{-3}$ ). For elliptic orbits and the assumption that the number of particles per unit time interval passing the pericentre of a common elliptic orbit is constant (Haug, 1958), this transformation was evaluated by Krivov et al. (2005):

$$N(m, r) = \frac{1}{4\pi^2 r^3 \sin \epsilon} \int_e \int_q n(m, q, e) \left(\frac{r}{q}\right)^{3/2} (1-e)^{1/2} \times \left(2 - \frac{r}{q}(1-e) - \frac{q}{r}(1+e)\right)^{-1/2} dq de, \quad (2.23)$$

where the integration domain is  $q \leq r \leq q(1+e)/(1-e)$ .

**ACE** uses  $N(m, r)$  and assumes spherical bodies with radius  $s$  to infer further quantities. These are the spatial number density with respect to particle size, also denoted with the letter  $N$  but dependent on  $s$  instead of  $m$ ,

$$N(s, r) = 4\pi s^2 \rho N(m, r), \quad (2.24)$$

the mass surface density

$$\Sigma(r) = 2r \sin \epsilon \int_m m N(m, r) dm, \quad (2.25)$$

---

<sup>7)</sup> Currently, the Jena group is working on an extension of the existing **ACE** code to open up the phase space for more variables (Löhne et al., in preparation). Modelling of azimuthally and vertically asymmetric discs with a revised **ACE** code will become feasible in the near future. That work is part of the Research Unit FOR2285, funded by the DFG.

## 2 Fundamentals

the (geometrical) normal optical depth

$$\tau(r) = 2r \sin \epsilon \int_s \pi s^2 N(s, r) ds, \quad (2.26)$$

and the (geometrical) normal optical depth per unit logarithmic size interval

$$\tau_{\log s}(r, s) = 2r \sin \epsilon \pi s^3 \ln(10) N(s, r). \quad (2.27)$$

The units are  $[N(s, r)] = \text{cm}^{-1} \text{cm}^{-3}$ ,  $[\Sigma(r)] = \text{g cm}^{-2}$ , and  $[\tau(r)] = [\tau_{\log s}(s, r)] = 1$ .

Table 2.1 lists the input parameters that have to be specified for each ACE simulation. It also includes a qualitative remark how well the parameters are constrained by ob-

**Table 2.1:** Model parameters for ACE simulations

Category	Parameter	Constraints?	Assumed standard value
Star	Luminosity, $L_\star$	+++	...
	Mass, $M_\star$	+++	...
	Mass-loss rate, $\dot{M}_\star$	+	...
	Stellar wind speed, $v_{\text{sw}}$	+	400 km s <sup>-1</sup>
Planetesimals	Initial mass, $M_0$	-	...
	Semi-major axis range, $a_{\text{min}} \dots a_{\text{max}}$	+	...
	Initial index of radial distribution, $\alpha_\Sigma$	-	...
	Radius of largest object, $s_{\text{max}}$	-	...
	Initial index of size distribution, $\gamma$	-	$-\frac{7+b_s/3}{2+b_s/3}$
	Eccentricity range, $e_{\text{min}} \dots e_{\text{max}}$	-	...
	Maximum orbital inclination, $\epsilon$	-	$e_{\text{max}}/2$
Solids	Bulk density, $\rho$	-	...
	Radiation pressure to gravity ratio, $\beta_{\text{rp}}$	-	...
Collisions	Slope of fragment mass distribution, $\eta$	+	-11/6
	Material strength, $Q_{\text{D,s}}, Q_{\text{D,g}}, b_s, b_g$	-	...

**Notes.** Symbols in the third column stand for well known parameters (+++), poorly known parameters (+), and unknown parameters (-). The standard assumptions given in the fourth column were widely applied in the modelling of the systems considered in this work and were motivated by the following:  $v_{\text{sw}} = 400 \text{ km s}^{-1}$  is the averaged solar wind speed around the equatorial plane (Ferreira et al., 2003);  $\gamma = -(7 + b_s/3)/(2 + b_s/3)$  agrees with the equilibrium distribution of dust in an infinite collisional cascade (O'Brien & Greenberg, 2003);  $\epsilon = e_{\text{max}}/2$  results from the energy equipartition relation (Greenberg et al., 1991);  $\eta = -11/6$  corresponds to the equilibrium value averaged over many collisions (Thébault & Augereau, 2007).



servations. In addition to stellar and disc properties, the modeller has to define the resolution of the grid, i.e. the logarithmic bin density for masses, pericentric distances, and eccentricities. The parallelised code is able to work on a network of multi-core machines. A simulation, which predicts the collisional evolution of a debris disc over a time span corresponding to the age of the host star, typically needs a few days up to several weeks of CPU time, depending on the computational accuracy. **ACE** outputs the phase-space distribution, the planetesimals mass (which is essentially equal to the total mass of the whole disc), the mass of the dust portion, as well as the size and radial distributions of the disc objects at each calculated timestep, in terms of the quantities given in Equations (2.24)–(2.27).

## 2.4 Interaction between dust and stellar radiation

Section 2.3 describes how to compute the dust distribution of a debris disc. In order to compare with observational data, we still have to calculate the thermal and scattered light emission properties of the modelled circumstellar dust distribution. This is sketched out below.

### 2.4.1 Thermal emission

We consider an axisymmetric disc at a distance  $D$  from the observer. The disc is assumed to be optically thin, so that all disc objects are directly illuminated by the host star. Then, the thermal flux density of the whole disc at a given wavelength  $\lambda$ , reads

$$F_\lambda = \frac{2\pi}{D^2} \int_s \int_r 2r \sin \varepsilon N(s, r) \pi s^2 Q_{\text{abs}}(s, \lambda) B_\lambda(T_d) r \, dr \, ds, \quad (2.28)$$

where  $B_\lambda(T_d)$  denotes the Planck function of a dust particle with temperature  $T_d$ . The latter depends on grain size and distance to the star.

We can find an implicit equation to determine the temperature  $T_d$  by assuming thermal equilibrium (i.e., the energy per time a dust grain absorbs from stellar radiation equals the radiated power the grain re-emits over its surface):

$$\frac{\pi s^2}{4\pi r^2} \int_0^\infty Q_{\text{abs}}(s, \lambda) 4\pi R_\star^2 F_\lambda(T_\star) \, d\lambda = 4\pi s^2 \int_0^\infty Q_{\text{abs}}(s, \lambda) \pi B_\lambda(T_d) \, d\lambda \quad (2.29)$$

with  $R_\star$  being the stellar radius, and  $F_\lambda(T_\star)$  the flux density on the stellar surface at temperature  $T_\star$ .

## 2 Fundamentals

The debris discs investigated in this thesis are spatially resolved at multiple wavelengths and it is possible to measure the surface brightness as a function of distance from the star. The surface brightness of thermal emission at a given wavelength and in a narrow annulus can be approximated by

$$S_{\lambda}^{\text{therm}}(r) = \frac{2r \sin \varepsilon}{D^2} \int_s N(s, r) \pi s^2 Q_{\text{abs}}(s, \lambda) B_{\lambda}(T_d) ds. \quad (2.30)$$

In reality, discs are not necessarily seen directly face on, but can be inclined by an angle  $\theta$ . If so, the transformation of coordinates from the disc frame  $\vec{R} = (X, Y)$  to the projected sky frame  $\vec{r} = (x, y)$  reads

$$x = X, \quad y = Y \cos \theta, \quad (2.31)$$

where the  $x$  direction is assumed to coincide with the line of nodes of the inclined disc. In this definition,  $\theta$  is measured from pole on, i.e. the disc edge is seen on the sky for  $\theta = 90^\circ$ . Although the disc emission is vertically compressed because of the inclination, the total energy radiated towards the observer must be conserved and the surface brightness of the inclined disc is given by

$$\tilde{S}_{\lambda}^{\text{therm}}(\vec{r}) = \left| \frac{\partial(X, Y)}{\partial(x, y)} \right| S_{\lambda}^{\text{therm}}(R(\vec{r})) = \frac{1}{\cos \theta} S_{\lambda}^{\text{therm}}(R(\vec{r})). \quad (2.32)$$

To compare models with measurements, we need to convolve the synthetic images with an instrument-specific point spread function (PSF), which accounts for deformations through diffraction. The convolution can be expressed as

$$\tilde{S}_{\lambda}^{\text{therm}}(\vec{r}) * \text{PSF}_{\lambda}(\vec{r}) = \frac{1}{\cos \theta} \int_0^{\infty} \int_0^{2\pi} S_{\lambda}(R(\vec{r} - \vec{r}')) \text{PSF}_{\lambda}(r', \phi') r' d\phi' dr', \quad (2.33)$$

where  $\phi$  is the polar angle and

$$R(\vec{r} - \vec{r}') = \sqrt{(r \cos \phi - r' \cos \phi')^2 + (r \sin \phi - r' \sin \phi')^2 / \cos^2 \theta}. \quad (2.34)$$

### 2.4.2 Scattered light

In contrast to thermal emission, which can be assumed to be radiated uniformly over the whole surface of dust grains, the intensity of scattered light strongly depends on the scattering direction  $\vartheta$ , which is the angle between incident and scattered rays.

Taking this into account, the surface brightness for scattered light can be written as

$$S_{\lambda}^{\text{sca}}(b) = \frac{R_{\star}^2}{D^2} F_{\lambda}(T_{\star}) \int_{\ell(b)} \int_s \frac{\pi s^2}{4\pi r^2} Q_{\text{sca}}(s, \lambda) S_{11}(s, \lambda, \vartheta) N(s, r) ds d\ell, \quad (2.35)$$

where the outer integral is along the line of sight  $\ell$ , and  $b$  denotes the impact parameter, i.e. the distance between the line of sight and the position of the star. The function  $S_{11}(s, \lambda, \vartheta)$  gives the angular distribution of the light intensity scattered by a particle with radius  $s$  at a given wavelength  $\lambda$ . It can be retrieved from the  $4 \times 4$  Mueller matrix  $S_{ij}$ , which describes the relation between the Stokes vectors of the incident and the scattered electromagnetic fields (Mueller, 1948; Bohren & Huffman, 1983).

The scattered light intensity drops rapidly with wavelength since  $Q_{\text{sca}} \propto \lambda^{-4}$  for  $\lambda \gg s$  and a nearly  $\lambda$ -independent refractive index (Rayleigh scattering, Rayleigh, 1897; Bohren & Huffman, 1983). The smallest grains remaining in debris discs around late-type stars are typically less than  $1\mu\text{m}$  in size (Section 2.2.2), which implies that scattered light is only detectable at optical or at most near-IR wavelengths.

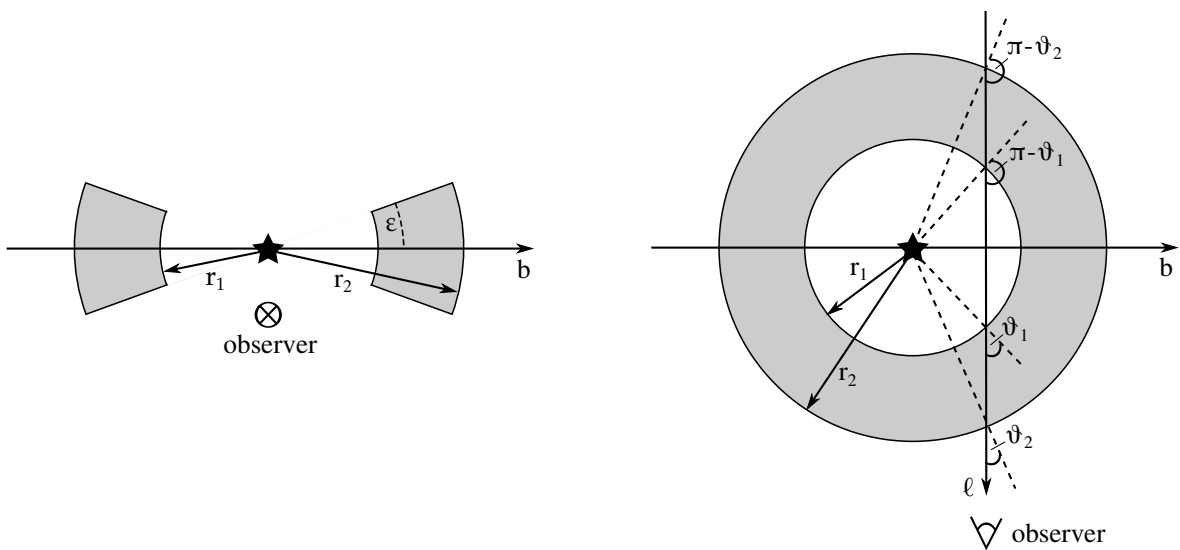


**Figure 2.2:** Edge-on disc geometry in side view (*left*) and top view (*right*)

Equation (2.35) will be now specified for a disc seen nearly edge-on, which is the only case considered in this thesis (Section 2.4.2). Figure 2.2 sketches an edge-on disc with an inner radius  $r_1$  and an outer radius  $r_2$ . We are interested in the surface brightness profile on the midplane (i.e., along the major axis). Using  $\sin \vartheta = b/r = b/\sqrt{b^2 + \ell^2}$

## 2 Fundamentals

and  $r^2 d\vartheta = -b d\ell$ , the midplane brightness profile is then calculated according to

$$S_{\lambda}^{\text{sca}}(b) = \frac{R_{\star}^2 F_{\lambda}(T_{\star})}{4b^2 D^2} \int_s \int_{\vartheta_2}^{\vartheta_1} s^2 Q_{\text{sca}}(s, \lambda) (S_{11}(s, \lambda, \vartheta) + S_{11}(s, \lambda, \pi - \vartheta)) \times N(s, b/\sin \vartheta) \sin \vartheta d\vartheta ds \quad (2.36)$$

for  $b < r_1$ , and

$$S_{\lambda}^{\text{sca}}(b) = \frac{R_{\star}^2 F_{\lambda}(T_{\star})}{4b^2 D^2} \int_s \int_{\vartheta_2}^{\pi - \vartheta_2} s^2 Q_{\text{sca}}(s, \lambda) S_{11}(s, \lambda, \vartheta) \times N(s, b/\sin \vartheta) \sin \vartheta d\vartheta ds \quad (2.37)$$

for  $r_2 \geq b \geq r_1$ , where  $\vartheta_i = \arcsin(b/r_i)$  for  $i = 1, 2$ .

In principle, the synthetic scattered light profile has to be convolved with the instrumental PSF as described for thermal emission. However, the size of the PSF may be much smaller at short wavelengths than the typical disc extent, and therefore, it is justified to neglect the convolution here.<sup>8)</sup>

Polarimetric analysis of the scattered light provides another characteristic observable: the degree of polarisation. If a dust particle is illuminated by unpolarised stellar light, the degree of linear polarisation is defined as

$$P_{\lambda} = \frac{I_{\perp} - I_{\parallel}}{I_{\perp} + I_{\parallel}}, \quad (2.38)$$

where  $I_{\perp}$  and  $I_{\parallel}$  are the scattered light intensities perpendicular and parallel to the scattering plane, i.e. the plane containing the star, the dust grain, and the observer. The degree of polarisation is positive (negative) if the scattered light is partially polarised in the perpendicular (parallel) direction to the scattering plane. Following the assumptions for an edge-on disc as described above, we obtain

$$P_{\lambda}(b) = - \frac{\int_s \int_{\vartheta_2}^{\vartheta_1} s^2 Q_{\text{sca}}(s, \lambda) (S_{12}(s, \lambda, \vartheta) + S_{12}(s, \lambda, \pi - \vartheta)) N(s, b/\sin \vartheta) \sin \vartheta d\vartheta ds}{\int_s \int_{\vartheta_2}^{\vartheta_1} s^2 Q_{\text{sca}}(s, \lambda) (S_{11}(s, \lambda, \vartheta) + S_{11}(s, \lambda, \pi - \vartheta)) N(s, b/\sin \vartheta) \sin \vartheta d\vartheta ds} \quad (2.39)$$

---

<sup>8)</sup>E.g., the *HST* resolution at 600 nm is about 0.06'' that is two orders of magnitude smaller than the angular sizes of the debris discs considered in this thesis.

for  $b < r_1$ , and

$$P_\lambda(b) = -\frac{\int_s \int_{\vartheta_2}^{\pi-\vartheta_2} s^2 Q_{\text{sca}}(s, \lambda) S_{12}(s, \lambda, \vartheta) N(s, b/\sin \vartheta) \sin \vartheta \, d\vartheta \, ds}{\int_s \int_{\vartheta_2}^{\pi-\vartheta_2} s^2 Q_{\text{sca}}(s, \lambda) S_{11}(s, \lambda, \vartheta) N(s, b/\sin \vartheta) \sin \vartheta \, d\vartheta \, ds} \quad (2.40)$$

for  $r_2 \geq b \geq r_1$ .

### 2.4.3 Numerical tools

The thermal emission of debris discs can be calculated with the codes `SEDUCE` (`SED Utility for Circumstellar Environment`) and `SUBITO` (`SURface BRightness Investigation TOol`), written by Sebastian Müller in C++ (Krivov et al., 2008; Müller et al., 2010; Müller, 2010). `SEDUCE` generates SEDs while `SUBITO` determines surface brightnesses at requested wavelengths. Furthermore, the C++ program `PHSImage` (`PHase Space Image`) can be employed for the computation of scattered light properties. `PHSImage` was originally developed by Torsten Löhne to produce synthetic disc images from `ACE` phase-space distributions. The author of this thesis modified and extended this code in order to implement a routine for the calculation of polarisation maps.

As inputs, all programs need information on the star, the dust distribution, and the material properties. In addition, several computational parameters have to be defined. The tools can read stellar photosphere models from the `PHOENIX/Gaia` grid (Brott & Hauschildt, 2005) with the specification of stellar temperature or luminosity. Through a direct interface to `ACE`, the codes receive the information about the dust distribution for the timestep considered. Disc properties can be computed for the overall disc or parts of the disc by the definition of minimum/maximum values of integrals ( $s_{\min}, s_{\max}, r_{\min}, r_{\max}$ ). Tabulated data of refractive indices and  $\beta$  values as functions of wavelength and particle radius serve as input for the characterisation of the dust material. Such tables are delivered by standard Mie routines (e.g., Wolf & Voshchinnikov, 2004).

# 3 HIP 17439

*This chapter presents our results published in Schüppler et al. (2014). I performed the collisional modelling and made major contributions to the interpretation of the simulations. Other parts of this study were done in collaboration with Torsten Löhne, Alexander V. Krivov, Steve Ertel, Jonathan P. Marshall, and Carlos Eiroa. Schüppler et al. (2014) is a follow-up study of Ertel et al. (2014b) where I contributed as co-author.*

## 3.1 System description and previous work

Koerner et al. (2010) first detected a debris disc around the nearby star HIP 17439 (HD 23484) using MIPS (Multiband Infrared Photometer for *Spitzer*, Werner et al., 2004). Later on, the system was observed as part of the *Herschel* Open Time Key Programme DUST around NEarby Stars (DUNES, Eiroa et al., 2010, 2013). The *Herschel* instruments PACS (Photodetector Array Camera and Spectrometer, Poglitsch et al., 2010) and SPIRE (Spectral and Photometric Imaging REceiver, Griffin et al., 2010; Swinyard et al., 2010) spatially resolved the disc in the far-IR. Together with HD 202628 (Krist et al., 2012), HD 207129 (Krist et al., 2010; Marshall et al., 2011; Löhne et al., 2012), and HD 107146 (Ertel et al., 2011), HIP 17439 harbours one of the most extended discs around Sun-like stars identified to date.

Observational data of the HIP 17439 system, including the SED and the radial surface brightness profiles from the *Herschel*/PACS 70, 100, and 160  $\mu\text{m}$  images, were analysed by Ertel et al. (2014b) for the first time. They used a classic modelling approach (see Section 1.3) with a dust *surface* number density proportional to  $s^\gamma r^{\alpha_\tau}$ , where  $\gamma$  and  $\alpha_\tau$  being the slopes of the size and radial distributions respectively.<sup>9)</sup> The model was fitted to the data by a multi-dimensional  $\chi^2$  minimisation. A one- or a two-component model can reproduce the observations (Table 3.1).

Ertel et al.'s (2014b) best-fit one-component model is a broad disc of dust with a radial extent of several hundreds of au and a nearly constant number density with distance ( $\alpha_\tau = -0.1$ ). Contrary, the two-component model consists of two dust belts with steep radial distributions. Thus, most of the dust is located near the inner edges of the belts around 29 and 91 au, and the two components are spatially separated by a wide gap.

---

<sup>9)</sup>The corresponding spatial number density is  $N(s, r) \propto s^\gamma r^{\alpha_\tau - 1}$  (see also Section 2.3.2).

**Table 3.1:** Best-fit results obtained by fitting power-law models to observations of the HIP 17439 disc, originally published in Ertel et al. (2014b).

Parameter	Best fit [ $3\sigma$ ]	
	One-component model	Two-component model Inner comp.    Outer comp.
$r_1$ [au]	$8.3^{+5.6}_{-0.8}$	$29.2^{+6.6}_{-27.5}$ $90.9^{+79.9}_{-74.9}$
$r_2$ [au]	$394.0^{+106.0}_{-267.4}$	500.0 (fixed value)
$\alpha_\tau$	$-0.1^{+1.0}_{-1.5}$	$-4.0^{+3.6}_{-1.0}$ $-1.6^{+2.6}_{-3.4}$
$s_{\min}$ [ $\mu\text{m}$ ]	$8.1^{+2.6}_{-1.9}$	$5.2^{+10.8}_{-1.7}$ $12.4^{+17.5}_{-12.3}$
$\gamma$	$-4.0^{+1.0}_{-0.9}$	$-5.5^{+1.8}_{-0.0}$ $-4.3^{+1.3}_{-1.2}$
$\theta$ [ $^\circ$ ]	$63.9^{+18.1}_{-46.1}$	$60.0^{+10.0}_{-10.0}$
$M_d$ [ $M_\oplus$ ]	$1.3 \times 10^{-2}$	$2.1 \times 10^{-4}$ $1.1 \times 10^{-2}$
Dust material	Astron. silicate (Draine, 2003)	Astron. silicate (Draine, 2003)

**Parameters.** Inner (outer) edge of the radial dust distribution  $r_1$  ( $r_2$ ), radial distribution index  $\alpha_\tau$ , minimum grain size  $s_{\min}$ , size distribution index  $\gamma$ , disc inclination from face on  $\theta$ , dust mass for particles up to 1 mm in radius  $M_d$ .

We continued the study by Ertel et al. (2014b) with an in-depth collisional modelling analysis of the HIP 17439 system. The goal was to check whether the proposed one- and two-component solutions are physically plausible in the light of the more realistic collisional modelling, which takes the actual physical processes operating in a debris disc into account.

## 3.2 Observational data

HIP 17439 is a K2 V star (Torres et al., 2006; Gray et al., 2006) at a distance of 16 pc (van Leeuwen, 2007) with an age of 0.8...3.7 Gyr (Mamaiek & Hillenbrand, 2008; Garcés et al., 2010; Fernandes et al., 2011). We adopted the stellar atmosphere model from Ertel et al. (2014b), taken from the PHOENIX/*Gaia* grid (Brott & Hauschildt, 2005) and scaled to *WISE* and near-IR fluxes. Relevant stellar parameters for our modelling were the mass  $M_\star = 0.82 M_\odot$ , the luminosity  $L_\star = 0.4 L_\odot$ , and the effective temperature  $T_\star = 5166$  K.

Photometric data were adopted from table 3 of Ertel et al. (2014b). The SED is densely sampled between 12 and 500  $\mu\text{m}$  by measurements of *IRAS*, *Spitzer*, and *Herschel*. The PACS images show an elliptic disc with increasing extent from 131 au at 70  $\mu\text{m}$  to 253 au at 160  $\mu\text{m}$  in the direction of the major axis. We used the radial profiles derived

by Ertel et al. from the PACS images at 70, 100, and 160  $\mu\text{m}$ , but not from the SPIRE images, since the disc appears only marginally resolved at SPIRE wavelengths, and the source brightness profile is sparsely sampled, which causes larger uncertainties in the radial profiles.

### 3.3 Modelling

We performed the *ACE* runs with input parameters listed in Table 3.2. The simulations were initialised with bodies from 0.01  $\mu\text{m}$  up to 10 m in radius. Since all bodies were small enough to be outside the gravity-dominated range of the fragmentation energy, we considered only the tensile binding energy for which we assumed  $Q_{\text{D},s} = 10^7 \text{ erg g}^{-1}$  and  $b_s = -0.37$ . The initial dust and parent body populations were uniformly distributed ( $\alpha_\Sigma = 0$ ) over the radial ranges given in the third column of Table 3.2.

We assumed the solids in the disc to be composed of a 50:50 mixture of water ice and astronomical silicate (Li & Greenberg, 1998; Draine, 2003,  $\rho = 2.35 \text{ g cm}^{-3}$ ). The optical constants of this homogeneous mixture were determined via effective medium theory given by the Bruggeman (1935) mixing rule. Optical parameters to determine the radiation pressure efficiency (Equation 2.11) were calculated by means of Mie theory (Bohren & Huffman, 1983).

For all simulations, we fixed the disc inclination to  $\theta = 65^\circ$ , which is consistent with the lower limits inferred from observations and the values found by power-law fitting (Ertel et al., 2014b). We convolved the synthetic images from the *ACE* models at 70, 100, and 160  $\mu\text{m}$  with PSFs of  $\alpha$  Boo, which was taken as representative of a pure point source. The PSFs were rotated by  $-103.4^\circ$  ( $103.4^\circ$  clockwise) to align the maps with the telescope pupil orientation on the sky during the HIP 17439 observations.

In the course of the collisional evolution, the simulations reach a quasi-equilibrium state (Löhne et al., 2008) in which the relative numbers of particles with different sizes in different orbits do not change with time anymore. In other words, collisional equilibrium is reached once the shape of the size distributions stopped changing at a given distance from the star. Strictly speaking, this is only true for the main belts, which are the narrow rings where we initially placed the planetesimal distributions, and the outer disc regions, which are beyond the main belts. The situation is different for the inner regions, which get filled by small grains because of the inward transport of dust from the main belts as time elapses. As long as the inner regions are dominated by transport and not by collisions, larger and larger dust grains drift inward, and the



size distribution shapes of the inner disc particles are not constant with time. We therefore consider the model discs in collisional equilibrium when the main belts meet the criterion mentioned above.

The simulation results will not depend on the upper size cut-off  $s_{\max}$  if the largest bodies are sufficiently large to be not involved in the collisional cascade by the time when the dust population reaches the collisional equilibrium. This was ensured for the value chosen in our runs,  $s_{\max} = 10$  m. A larger  $s_{\max}$  would only slow down the simulations.

Once the equilibrium state is reached, the dust mass in the systems decreases continually with time because of two main effects: i) particles are ground down to fragments with masses smaller than the minimum mass in the ACE grid (quasi vapourisation), and ii) particles are transported close to the star so that their pericentric distances are shorter than the minimum pericentric distance in the ACE grid (quasi sublimation). We stopped the simulations as soon as the thermal emission of the dust had reduced to the observed excess strength, given by the photometric data. Since the simulation time  $t_{\text{sim}}$  depends strongly on the choice of the initial conditions,  $t_{\text{sim}}$  does not necessarily correspond to the system's actual physical age  $t_{\text{phys}}$ . For instance, if we start with a

**Table 3.2:** Descriptions of ACE simulations for the HIP 17439 disc

Model identifier	Disc component	$a_{\min} \dots a_{\max}$ [au]	$e_{\max}$	$\dot{M}_{\star}$ [ $\dot{M}_{\odot}$ ]	$M_{\text{d}}$ [ $10^{-3} M_{\oplus}$ ]	$f_{\text{d}}$ [ $10^{-5}$ ]
One planetesimal belt (1PB)						
1PB_FG	Outer belt	120...150	0.04	0	6.3	8.1
1PB_SW1	Outer belt	120...150	0.04	15	7.0	10.6
1PB_SW2	Outer belt	120...150	0.04	30	7.2	10.2
1PB_r+	Outer belt	150...180	0.04	15	9.5	9.5
Two planetesimal belts (2PBs)						
2PB_I	Inner belt	30...40	0.04	0	0.9	8.5
	Outer belt	100...130	0.001	0	5.7	2.0
2PB_II	Inner belt	30...40	0.04	0	0.4	4.6
	Outer belt	150...180	0.04	0	8.7	4.8

**Notes.**  $M_{\text{d}}$  is the dust mass (mass of all particles with radii  $< 1$  mm) and  $f_{\text{d}}$  is the fractional luminosity (IR luminosity of the dust disc divided by the stellar luminosity). The bin densities of the  $(m, q, e)$  grid used were as follows. All simulations were initialised with 1.3 bins per mass decade and 7.3 bins per eccentricity decade. The resolution of the pericentre grid differed. Here, the number of bins per distance decade was 14.5 in the 1PB runs, but 10.5 for the inner and 16.1 for the outer belts in the 2PB runs.

very massive planetesimal belt, much dust will be produced and it will take a long time for the thermal emission to reach a rather low level, which can result in  $t_{\text{sim}} \gg t_{\text{phys}}$ . We assumed initial planetesimal belt masses of  $\approx 1 M_{\oplus}$  for all simulations. The longest simulation time turned out to be  $t_{\text{sim}} \approx 8 \text{ Gyr}$  which is longer than  $t_{\text{phys}} \simeq 1...4 \text{ Gyr}$ .

## 3.4 Models with one planetesimal belt

### 3.4.1 First-guess model

In a first-guess (FG) run we placed planetesimals into a narrow belt between 120 and 150 au (semi-major axis range of planetesimals). This location was motivated by the lower  $3\text{-}\sigma$  limit of  $r_2$  in the Ertel et al. (2014b) one-component model (Table 3.1). Results of this first-guess model (1PB\_FG) are depicted in Figure 3.1.

The modelled SED reproduces the far-IR observations quite well, but underestimates the mid-IR flux probed by the spectrum from *Spitzer*/IRS (Infrared Spectrograph, Houck et al., 2004). Although the radial profiles are almost within the  $1\text{-}\sigma$  uncertainties of the observational data at  $160 \mu\text{m}$ , they are too shallow for distances  $< 100 \text{ au}$  at  $70$  and  $100 \mu\text{m}$ . This clearly illustrates a deficit of warm dust emission.

A relocation of the planetesimal belt as a whole would not lead to significant improvements. If the belt is shifted inwards, the emission at longer wavelengths will be depressed since the dust grains in the main belt become warmer. That would have a detrimental effect because the model even now underestimates the  $160 \mu\text{m}$  point. Conversely, shifting the belt outwards would hamper the collisional depletion of larger particles and thus the production of smaller ones, which are needed for the warm emission. In the following, we therefore aimed at increasing the warm emission without changing the position of the planetesimal belt. This can be achieved by strengthening the inward transport of small dust grains.

### 3.4.2 Adding stellar winds

As outlined in Section 2.2.3, the presence of stellar winds induces a significant angular momentum loss of circumstellar dust. Accordingly, the timescale for the inward transport is shortened by a factor of  $[1 + (\beta_{\text{sw}}/\beta_{\text{rp}})(c/v_{\text{sw}})]^{-1}$  compared to the P-R drag-dominated case (see Equation 2.13).

Many cool, late-type stars on the main sequence are known to possess strong stellar winds (Wood et al., 2002, 2005) that can have significant impact on the dynamics of

circumstellar dust (e.g., Plavchan et al., 2005, 2009; Strubbe & Chiang, 2006; Reide-  
 meister et al., 2011). Wood et al. (2005) find a correlation between the stellar X-ray  
 flux density,  $F_X$ , and the stellar mass-loss rate for moderately rotating K main-sequence  
 stars:  $\dot{M}_*/R_*^2 \propto F_X^{1.34 \pm 0.18}$  for  $F_X \lesssim 8 \times 10^5 \text{ erg s}^{-1} \text{ cm}^{-2}$ . Given HIP 17439's X-ray lu-  
 minosity  $\log(L_X/L_*) = -4.9$  (*ROSAT* all-sky survey bright source catalogue, Voges  
 et al., 1999) and  $R_* = 0.8 R_\odot$ , this yields a mass-loss rate of  $\dot{M}_* = 24.6_{-9.5}^{+15.6} \dot{M}_\odot$ . How-  
 ever, the stellar mass-loss rate may not increase so strongly with the coronal X-ray

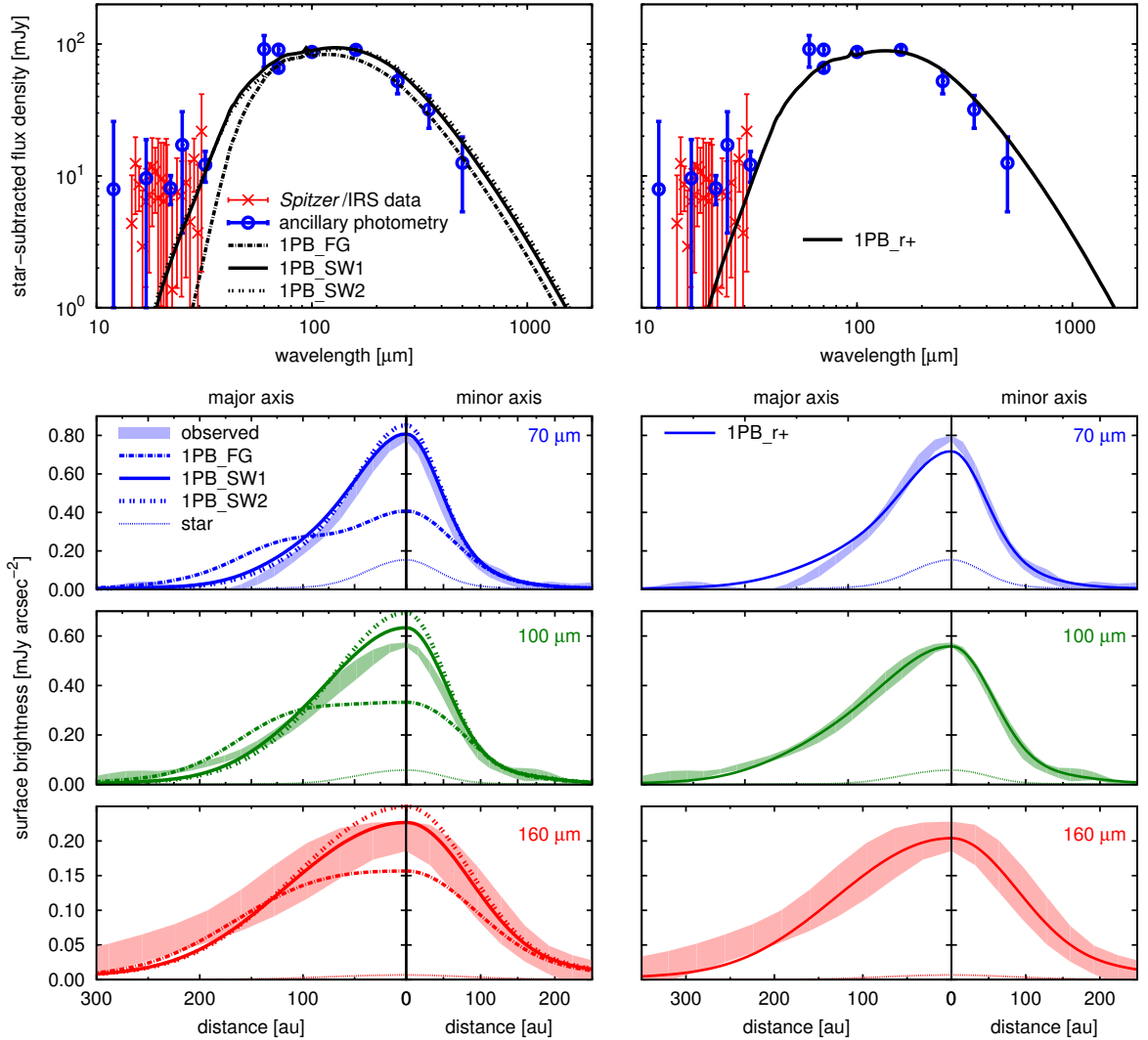


**Figure 3.1:** *Top panels:* excess radiation of HIP 17439's debris disc. Data points with a signal-to-noise ratio  $< 3$  were excluded from the available *Spitzer*/IRS spectrum. *Bottom panels:* surface brightness profiles at 70 (blue), 100 (green), and 160 μm (red). Colour-shaded areas depict the *Herschel*/PACS measurements with  $1\text{-}\sigma$  uncertainties. Cuts along the major (minor) axis are given in the left (right) parts of the panels. Lines in all diagrams show the 1PB models listed in Table 3.2.

flux density (Holzwarth & Jardine, 2007), which would result in a much lower  $\dot{M}_*$ . The model by Cranmer & Saar (2011) also predicts a significantly lower value,  $\dot{M}_* \approx 5 \dot{M}_\odot$ , for HIP 17439’s mean rotation period of 11 days (see figure 13 in Cranmer & Saar, 2011). There are also no clear observational indicators that HIP 17439 is active enough to emit strong stellar winds (J. Sanz-Forcada, private communication). Therefore, the assumption that HIP 17439 emits strong stellar winds should be treated with caution. The following simulations test whether the model can be actually improved by adding stellar winds.

We performed two stellar wind runs, 1PB\_SW1 and 1PB\_SW2, with  $\dot{M}_* = 15 \dot{M}_\odot$  and  $\dot{M}_* = 30 \dot{M}_\odot$ , respectively. The 1PB\_SW1 mass-loss rate corresponds to the lower limit of the Wood et al. criterion mentioned above. The 1PB\_SW2 rate is equal to what has been proposed for  $\varepsilon$  Eri – a star similar to HIP 17439 in mass, radius, and X-ray luminosity (Wood et al., 2002). Although there is still a lack of observations, cool K dwarfs are expected to have hot coronae and stellar winds driven by gas pressure similar to the solar wind (e.g., Lamers & Cassinelli, 1999; Wood, 2004). We therefore assumed the averaged solar wind speed,  $v_{\text{sw}} = 400 \text{ km s}^{-1}$ , for 1PB\_SW1 and 1PB\_SW2.

Figure 3.1 demonstrates that the SEDs of both stellar wind runs predict more emission between 20 and 70  $\mu\text{m}$  than our first-guess model. The new models also overcome the lack of central surface brightness emission and can reproduce the *Herschel* profiles significantly better. Furthermore, as can be seen by comparing 1PB\_SW1 and 1PB\_SW2, the brightness profiles become steeper with increasing stellar wind strength.

To better understand the reason for these modifications, we analysed how the dynamics of the dust is affected by the stellar wind activity. For this purpose, we calculated the transport and collisional lifetimes of dust particles with Equations (2.13) and (2.21). The transport timescale given by (2.13) only holds for particles launched from circular orbits. To ensure a consistent comparison with the collisional lifetimes, we also calculated  $T_{\text{collision}}$  only for the grains in lowly eccentric orbits. To this end, we considered the particles that populated the lowest eccentricity bin in our setups with eccentricities  $\lesssim 0.02$ . The particles are mostly affected by transport for  $T_{\text{collision}} \gg T_{\text{transport}}$ , whereas collisions play the dominant role for  $T_{\text{collision}} \ll T_{\text{transport}}$ . As illustrated by the timescale ratios in Figure 3.2, small particles are more effectively transported towards the star than destroyed by collisions in model 1PB\_SW1, where the grains interact with the stellar wind.

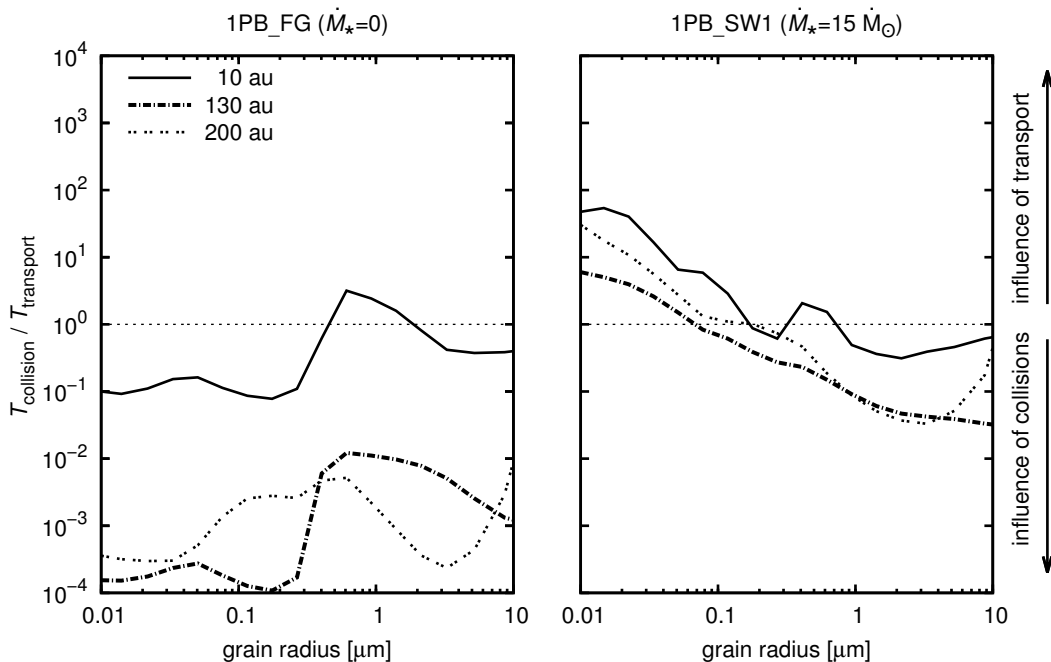


**Figure 3.2:** Influence of collisions and transport on dust for a model with (*right*) and one without (*left*) stellar wind activity. Model parameters are specified in Table 3.2. Different line styles depict the timescale ratios  $T_{\text{collision}}/T_{\text{transport}}$  inside (10 au, solid), within (130 au, dashed dotted), and outside (200 au, double dotted) the assumed planetesimal belt. Only particles with eccentricities  $e \lesssim 0.02$  are included in the calculation of  $T_{\text{collision}}$ .

Changes in the  $T_{\text{collision}}$ -to- $T_{\text{transport}}$  ratio also affect the dust distributions as shown in Figure 3.3. For a description, we consider the 1PB\_FG model without stellar wind activity first. For  $r < 130$  au, the number of particles continuously increases with decreasing grain size apart from an underabundance around  $s = 0.3 \mu\text{m}$  (Figure 3.3, top left). Although the smallest grains in the range of a few hundredths of microns are the most frequent, they barely affect the SED, because their thermal emission is negligible in the IR.<sup>10)</sup> Thus, the effective minimum grain size is given by the maximum of the size distribution at around  $10 \mu\text{m}$ . A large minimum grain size is characteristic of discs with low dynamical excitation of the planetesimals, which is parameterised by  $e_{\text{max}}$  (Thébault & Wu, 2008; Löhne et al., 2012; Krivov et al., 2013). In our model,  $e_{\text{max}}$  was set to low values (Table 3.2) that imply low collisional velocities between the largest disc bodies and inhibit the production of small dust. On the other hand, the destruction rate of dust grains is high because they have large eccentricities and collisional

<sup>10)</sup>The reason for that are spectroscopic properties of submicron-sized grains, namely a low absorption in the visible and a steeply decreasing emission efficiency at longer wavelengths (see figure 2 in Krivov et al., 2008).

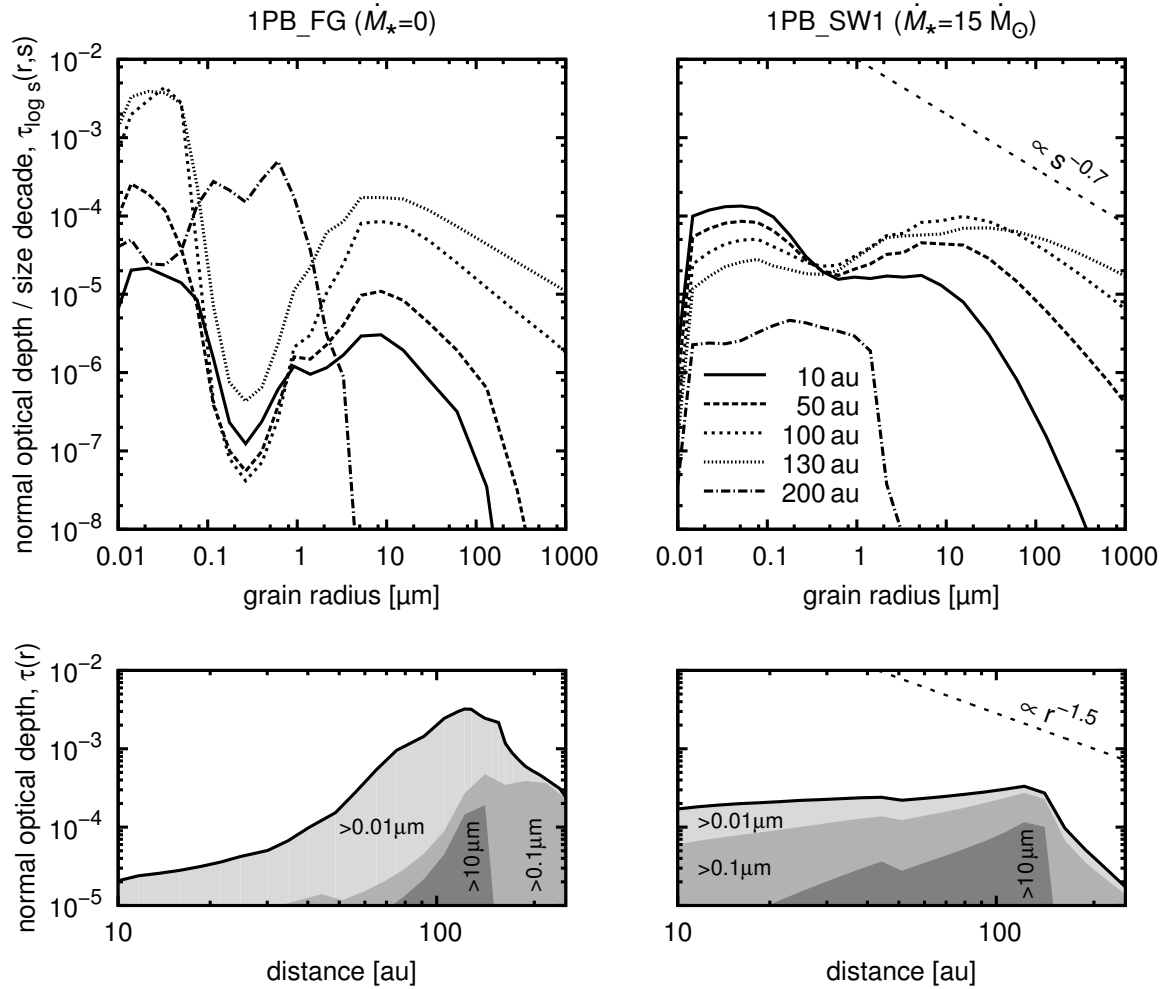


**Figure 3.3:** Dust distributions with (*right column*) and without (*left column*) stellar wind activity. *Top:* size distributions in terms of the normal optical depth per size decade,  $\tau_{\log s}(r, s)$ , for different distances from the star. The straight line in the right panel shows the theoretically predicted equilibrium slope for an infinite collisional cascade (O’Brien & Greenberg, 2003). *Bottom:* radial distributions in terms of the normal optical depth,  $\tau(r)$ , integrated over all grain sizes. The straight line in the right panel depicts the slope of the halo region predicted for collisionally active debris discs (Krivov et al., 2006; Strubbe & Chiang, 2006; Thébault & Wu, 2008). Shaded areas indicate the contributions from different size ranges.

velocities induced by radiation pressure. This imbalance cleans out the disc of small particles and leads to an increase in the typical grain size (Thébault & Wu, 2008).

The size distribution minima at around  $s = 0.3 \mu\text{m}$  correspond to the size where  $\beta_{\text{rp}}$  has a maximum (cf., Figure 2.1, middle panel). These grains are pushed to eccentric orbits by pressure forces after their collisional production, and therefore contribute little to the dust density at a given distance from the star.

The submicron-sized grains moving in eccentric orbits produce a dust halo beyond the planetesimal belt (Figure 3.3, bottom left). These grains have pericentres within the planetesimal zone and apocentres outside. Because of the low dynamical excitation, the halo is tenuous and exhibits a radial profile with an outer slope that is steeper than the  $-1.5$  predicted for collisionally very active debris discs (Krivov et al., 2006; Strubbe & Chiang, 2006; Thébault & Wu, 2008). The inner region is also tenuously filled by dust because of P-R drag.

Turning to the stellar wind simulation 1PB\_SW1, we notice more particles  $> 0.1 \mu\text{m}$  interior to the planetesimal belt, e.g. visible by the reduced depth of the minimum around  $0.3 \mu\text{m}$  (Figure 3.3, top right). The size distributions are nearly flat for the smallest grains but become significantly steeper at sizes between 10 and  $100 \mu\text{m}$ . This behaviour is caused by the enhanced inward transport due to stellar wind drag, which quickly removes small grains from the planetesimal belt (e.g., Vitense et al., 2010; Reidemeister et al., 2011; Wyatt et al., 2011; Krivov et al., 2013). As a further consequence, the inner region is filled more strongly by dust and has an almost constant optical depth profile (Figure 3.3, bottom right). It is this amount of warm dust in the inner region that produces more excess in the mid-IR and that strengthens the central emission resulting in steeper surface brightness profiles.

#### 3.4.3 Shifting the planetesimal belt

As illustrated in Figure 3.1, stellar winds can improve the model significantly. The moderate wind strength with  $\dot{M}_\star = 15 \dot{M}_\odot$  provides a better agreement than  $\dot{M}_\star = 30 \dot{M}_\odot$ . However, the major-axis profiles at 100 and  $160 \mu\text{m}$  are below the observed emission outside the planetesimal belt ( $r > 200 \text{ au}$ ) while they tend to overestimate it for  $r < 100 \text{ au}$ . To reduce the surface flux close to the star and simultaneously enhancing it farther out, we shifted the planetesimal belt by 30 au outwards (run 1PB\_r+). This flattens the 100 and  $160 \mu\text{m}$  profiles and further minimises the deviations from the observational data (Figure 3.1, right column).

We refrained from further refinements of the model because of the long simulation times (run 1PB\_r+ took about 72 CPU days). The results presented are sufficient for illustrating that a scenario including one narrow, outer planetesimal belt is only feasible with strong inward transport of dust.

### 3.5 Models with two planetesimal belts

The one-component model found by Ertel et al. (2014b) fits the observational data with reasonably low  $\chi^2$ . However, their figure 3 shows that the major-axis profile at  $100\ \mu\text{m}$  is not extended enough, leading to deviations  $> 1\sigma$ . Ertel et al. note that all modifications helping to obtain a broader emission at  $100\ \mu\text{m}$  would also result in a substantially broader emission at  $70\ \mu\text{m}$ , which is not observed. To adjust the profiles at  $70$  and  $100\ \mu\text{m}$  independently, Ertel et al. propose a two-component model where the inner component mostly contributes to  $70\ \mu\text{m}$  but marginally to  $100\ \mu\text{m}$ , and vice versa for the outer component (Table 3.1).

To check the hypothesis of a two-component disc, we assumed two narrow, well-separated planetesimal belts and simulated the evolution of the collisionally produced dust in each belt by two different ACE runs. The dust distributions for the inner and the outer component were stored as a function of the simulation time  $t_{\text{sim}}$ . After the runs had finished, we manually determined the timesteps  $t_{\text{sim}}$  where the sum of the thermal emissions from both components matches the observational data the best. Since the initial conditions of the planetesimal belts were not coupled in any way, we chose the appropriate timesteps independently, i.e.  $t_{\text{sim}}$  of inner and outer component were not to be necessarily equal.

We tested two different combinations of inner and outer planetesimal belts, denoted as 2PB\_I and 2PB\_II (Table 3.2). Although the two planetesimal belts are widely separated in each model, there is some overlap of the local dust densities, because of both the grains transported inwards by P-R drag from the outer belt and the halo grains pushed to eccentric orbits by radiation pressure from the inner belt. However, the optical depth of the outer component is more than one order of magnitude lower at the location of the inner planetesimal belt, and the optical depth of the inner component is several orders of magnitude lower at the position of the outer planetesimal belt. Figure 3.4 depicts this situation for 2PB\_II. Thus, the inner and the outer dust distribution can be seen as nearly collisionally decoupled, which justifies their independent treatment.

In model 2PB\_I, we placed the planetesimal belts close to the inner edge positions of the two components found by Ertel et al. (2014b). The outer component has to dominate the flux density at  $160\ \mu\text{m}$ , but at the same time, must contribute little to the flux density at shorter wavelengths. Consequently, the typical grain size of the dust has to be large in order to suppress the warm emission, which requires a low



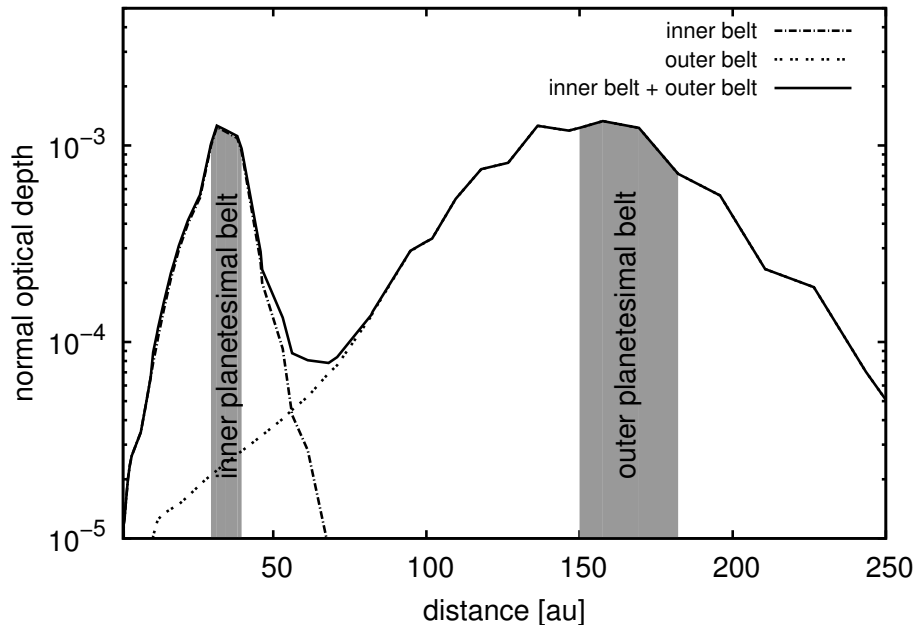


**Figure 3.4:** Radial profile of the optical depth in model 2PB\_II. Shaded regions indicate the extent of the inner and the outer planetesimal belt.

dynamical excitation of the planetesimal population (see explanations in Section 3.4.2). We assumed  $e_{\max} = 0.001$  for the outer belt, which is quite a low value inspired by the modelling of *Herschel*'s cold disc candidates (Krivov et al., 2013), and distinctly lower than  $e_{\max} = 0.04$  for the inner belt. This seems also consistent with the stirring mechanisms of debris discs (e.g., Kenyon & Bromley, 2008). Since the biggest stirrers are smaller farther out from the star, because their formation takes longer there, the dynamical excitation of planetesimals may be lower in outer regions.

The left column of Figure 3.5 presents the results for model 2PB\_I. The SEDs of both components are rather separated, because the one of the outer belt peaks beyond  $160 \mu\text{m}$  and has a minor contribution to  $70$  and  $100 \mu\text{m}$ . The overall SED clearly shows emission that is too low at  $100$  and  $160 \mu\text{m}$ , whereas it tends to overestimate the SPIRE photometry by  $\approx 1\sigma$ . Putting more weight on the outer component SED by taking the dust mass from an earlier timestep, consequently improves the agreement with the  $100$  and  $160 \mu\text{m}$  points, but has the opposite effect at longer wavelengths. The radial profiles have a steep fall-off that contradicts the observations. This is because they are mostly affected by the inner component, which is only marginally resolved.

A significant improvement in the model requires the radial profiles at  $100$  and  $160 \mu\text{m}$  to be broadened without simultaneously increasing the flux density at SPIRE wavelengths,

equivalent to a higher contribution of the outer, colder component. To this end, we departed from the Ertel et al. (2014b) setup, since it is difficult to translate their findings directly into a consistent collisional model. The components found by Ertel et al. have steep size distributions ( $\gamma < -4$ , Table 3.1), which cannot be explained by modelling with standard collisional prescriptions. The resulting size distributions from statistical codes such as ACE are typically broader, leading to broader SEDs as well. The entanglement in terms of resolvable emission from the two components in model 2PB\_I is thus greater than in Ertel et al. (2014b), reducing the ability to adjust the radial profiles at 70  $\mu\text{m}$  and 100/160  $\mu\text{m}$  independently.

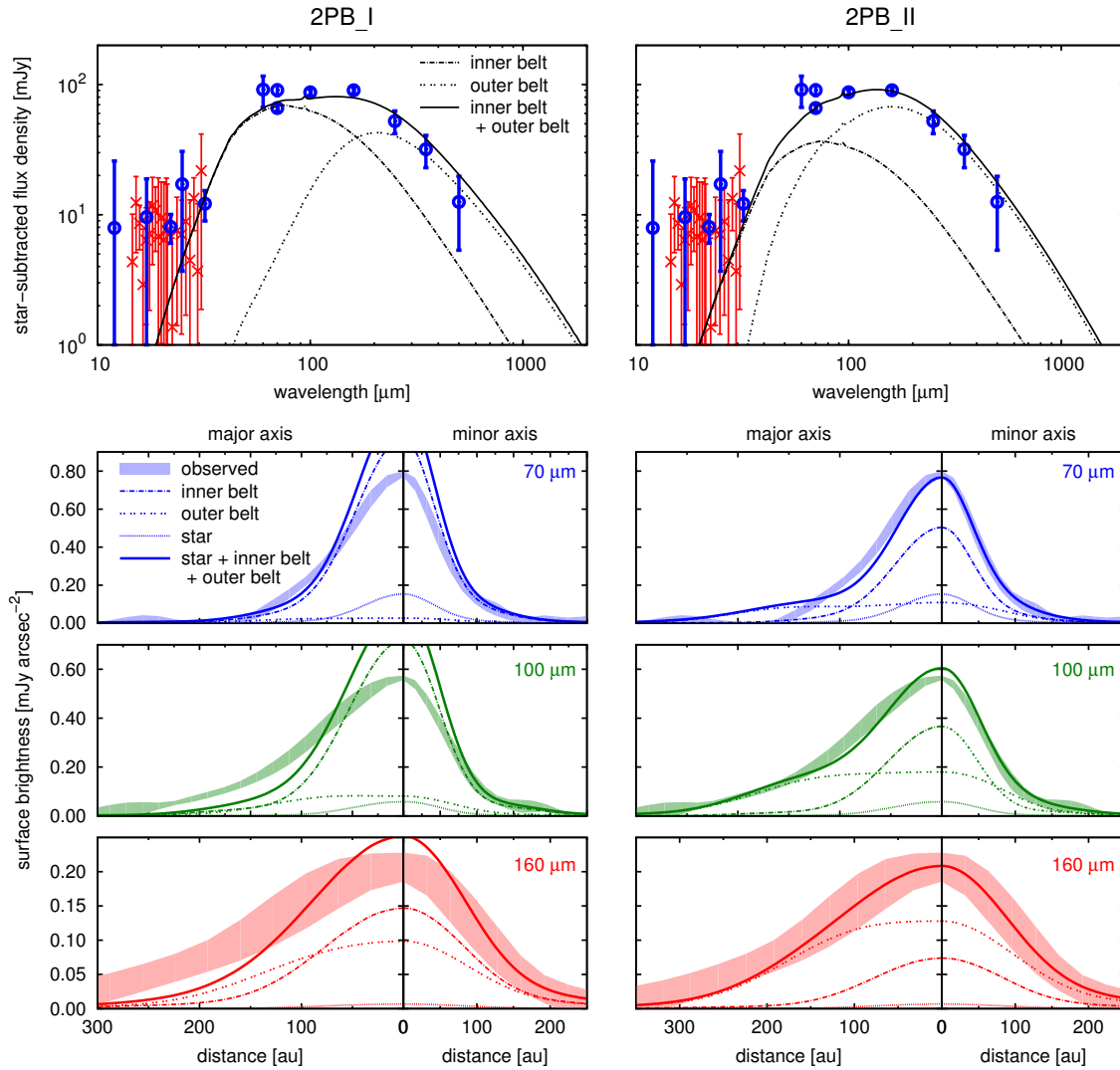


**Figure 3.5:** Same as Figure 3.1, but for the two-component models 2PB\_I (*left column*) and 2PB\_II (*right column*). Model parameters are specified in Table 3.2.

In the second two-component model 2PB\_II, we therefore shifted the outer planetesimal belt farther away from the star and increased  $e_{\max}$  up to 0.04. Compared to 2PB\_I, the outer belt now largely determines the overall SED at wavelengths  $> 100 \mu\text{m}$  (Figure 3.5, right column). Model 2PB\_II fits the PACS photometric points well, but still shows the trend of overestimating the SPIRE data. Thanks to the stronger contribution of the outer belt, all brightness profiles are sufficiently broadened.

## 3.6 Possibility of an extended planetesimal belt

The broad radial distribution of the dust revealed by the Ertel et al. (2014b) modelling suggests a further interpretation of the system architecture, which is a radially extended planetesimal belt. It implies that dust is produced everywhere in the whole disc. This is similar to a multi-component configuration where several narrow planetesimal rings reside close to each other. We used the results of our two-component model to discuss the possibility of an extended planetesimal belt.

Adding a third planetesimal ring between the two existing ones in model 2PB\_II would result in a structure that is close to an extended planetesimal belt configuration. Surely, such an additional ring would imply that all three planetesimal populations, namely the inner, the outer, and the intermediate belt, are no longer collisionally decoupled. Thébaud & Augereau (2007) consider a comparable situation. They divided an extended debris disc into several annuli and studied their collisional evolution. Inter-annuli interactions were incorporated through the orbit deformation of small grains due to radiation pressure. Particles within a certain annulus can collide with high- $\beta$  grains produced in another annulus closer in. Because the impact velocities in such events are higher than the ones between locally produced particles of the same size, the number of destructive collisions increases. The same effect appears in ACE simulations for a setup of closely adjacent planetesimal rings and is further analysed in Chapter 5. At the moment, this effect is rather unimportant for a qualitative discussion of an extended planetesimal belt around HIP 17439.

Figure 3.4 shows that the peak values of the optical depth for the inner and the outer belt are roughly the same,  $\sim 10^{-3}$ . A third intermediate planetesimal ring will help to fill the “hole” in the  $\tau$  profile between the two components. Such a quasi-extended planetesimal distribution might result in a nearly constant dust density similar to what is predicted by the stellar wind simulations (Section 3.4.2).

An extended planetesimal belt could naturally be expected, for instance, if planetesim-

als succeeded to form at a wide range of distances from the star but, for some reasons, have not grown further to gas giants. Such a belt would undergo a long-term collisional erosion which is faster closer to the star. This leads to a mass density profile  $\Sigma(r)$  rising outwards with a slope of about 7/3 (e.g., Kennedy & Wyatt, 2010; Wyatt et al., 2012), although the exact value can be different under different assumptions, e.g., for the initial radial profile of solids in the disc by the time of gas dispersal or for the critical fragmentation energy of planetesimals. We checked the radial slope  $\alpha_\Sigma$  of the mass surface density in our simulations by evaluating

$$\alpha_\Sigma = \frac{\Delta \log \Sigma(r)}{\Delta \log r} = \frac{\log \Sigma(r_o) - \log \Sigma(r_i)}{\log r_o - \log r_i}, \quad (3.1)$$

where  $r_i$  and  $r_o$  are the mean distances of the inner and outer planetesimal belts, respectively. We found  $\alpha_\Sigma \approx 1.1$  for 2PB\_I and  $\alpha_\Sigma \approx 0.7$  for 2PB\_II. These values are close to one and clearly confirm a solid density profile rising from the inside out. Thus, the HIP 17439 disc can also be consistent, at least qualitatively, with an inside-out collisional erosion of an extended planetesimal belt.

### 3.7 Prospects for observations

As demonstrated in the previous sections, several disc morphologies are able to explaining observations of the HIP 17439 system. The following addresses the question whether present-day observational facilities can reveal the actual disc architecture.

We predicted how our best one- and two-belt model would be seen by the 50-metre Large Millimetre Telescope (LMT) Alfonso Serrano, situated on the summit of Volcán Sierra Negra (Mexico, Hughes et al., 2010). The LMT is expected to operate in a 50-metre diameter aperture configuration in 2017. Then, it will be the most powerful single-dish telescope with respect to high-resolution imaging of HIP 17439's disc at millimetre wavelengths, although it is located in the northern hemisphere (latitude  $\approx +19^\circ$ ), and HIP 17439 (declination  $\approx -38^\circ$ ) is difficult to observe from this position. Inspired by the resolution of the AzTEC camera (Wilson et al., 2008) for the LMT final 50-metre configuration, we convolved images of 1PB\_r+ and 2PB\_II at 1.1 mm with a Gaussian profile that has a full width half maximum (FWHM) of  $6''$ . We assumed the signal-to-noise ratio  $S/N = 6$  and estimated the standard deviation  $\sigma$  of the background fluctuation as the peak flux in the simulated observations divided by the given  $S/N$ .

The synthetic AzTEC image of model 2PB\_II shows an inner emission above the  $5\text{-}\sigma$  level (Figure 3.6, bottom left) and gives direct evidence for the presence of an inner

planetesimal belt. However, the difference in the central emission between the one- and the two-component disc is small,  $\approx 1\sigma$ , and is not enough to clearly distinguish between the two models. To reach a significant detection of the inner belt, its emission should differ by at least  $3\sigma$  compared to the inner surface brightness dip of the one-belt model. This requires an S/N that is three times higher than assumed. Unfortunately, this

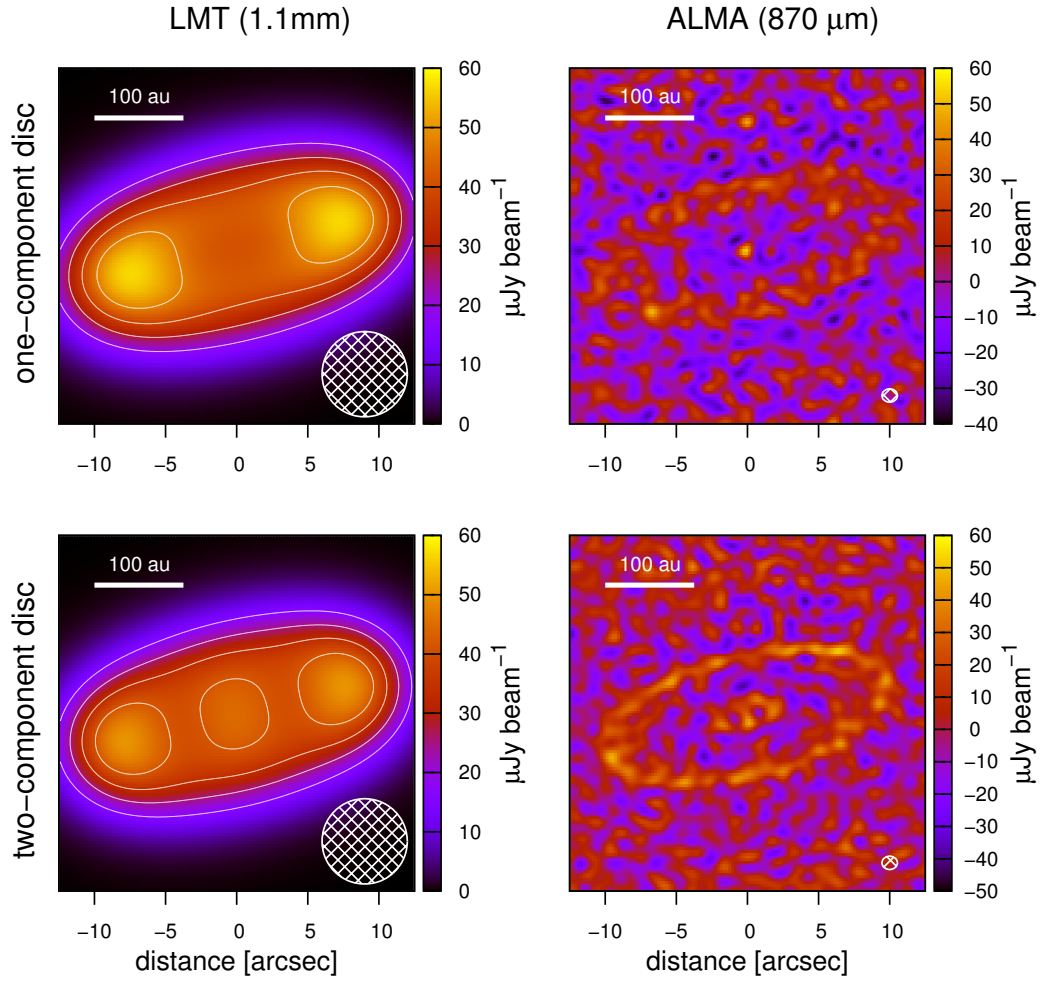


**Figure 3.6:** Discs with one component (1PB\_r+, *top*) and two components (2PB\_II, *bottom*) around HIP 17439 seen by two different telescopes. The discs have been rotated by the observed position angle. *Left column:* simulated LMT/AzTEC images generated by convolving the models at 1.1 mm with a Gaussian (FWHM =  $6''$ ). White circles in lower right corners illustrate the beam size. Contour lines show the iso-flux levels at  $2\sigma$ ,  $3\sigma$ ,  $4\sigma$ , and  $5\sigma$ . *Right column:* simulated ALMA images in Band 7 (central wavelength  $870\ \mu\text{m}$ ). Antenna configuration `alma.out01` (beam size  $1.1'' \times 0.9''$ ) and a water vapour overburden of  $0.1\ \text{mm}$  were used. A sensitivity of  $\approx 10\ \mu\text{Jy beam}^{-1}$  was achieved with an on-source integration time of 15 hours.

cannot be achieved since the AzTEC Photometry Mode Calculator<sup>11)</sup> already predicts a very long observing time of six days (including all overheads) to reach  $S/N = 6$ .

In a second attempt, we simulated interferometric ALMA observations with the ALMA image generator CASA 4.1.0<sup>12)</sup> (Common Astronomy Software Applications, McMullin et al., 2007), using the procedure `simalma`. We assumed observations in Band 7 under good weather conditions (0.1 mm precipitable water vapour) and applied a long integration time of 15 hours. Despite these excellent conditions, the inner component of the two-belt model is barely detectable (Figure 3.6, bottom right).

Our tests suggest that it would be difficult to distinguish between the one-belt and two-belt models considered within a reasonable observing time. It is important to note that other two-belt configurations, which reproduce the observations to a similar quality as the ones found, may mitigate the challenge of this work. For instance, if the inner planetesimal belt lies slightly farther away from the star as in our model 2PB\_II, the produced dust will become colder and brighter at long wavelengths, favouring its detectability with LMT or ALMA. In any way, such long-wavelength observations have high enough resolution to assess whether there is emission interior to the outer planetesimal belt. This at least helps to constrain general properties of the disc (and also of the host star) as recently demonstrated for HIP 17439's sibling  $\varepsilon$  Eri (Chavez-Dagostino et al., 2016).

### 3.8 Conclusions and discussion

The astrophysical plausibility of the different models proposed for HIP 17439's debris disc are discussed below.

We found a one-component model including a narrow planetesimal belt that requires the presence of stellar winds, which transport the particles from their birth region to the inner part of the system. This model equals Scenario II (Section 1.2). In our best run (1PB\_r+), the planetesimals reside between 150 and 180 au. Thus, they are much closer to the star than the outer edge of the disc predicted by the analytic one-component model of Ertel et al. (2014b). There, the outer edge was found at about 400 au, but could also be located much further inside because of large uncertainties. In general, planetesimals and dust production at very large distances from the host star seem to be unlikely because of the increasingly long growth and stirring timescales of planetesimals (e.g., Kenyon & Bromley, 2008). The moderate radial range of planetesimals in the

<sup>11)</sup><http://www.lmtgm.org/aztec-photometry-mode-calculator/>

<sup>12)</sup><http://casa.nrao.edu/>

one-belt model presented in this study therefore fits better in the debris disc formation theory.

Without stellar winds of sufficient strength, the data are consistent with a two-component disc, with a warm inner and a cold outer planetesimal belt, according to Scenario I (Section 1.2). In our best two-belt model (2PB\_II), the distance ratio of the planetesimal belt centre positions is  $r_o/r_i = 165 \text{ au}/35 \text{ au} \approx 5$ . To compare this with other studies, we remind that surveys of two-component discs around stars of different spectral types reveal the median temperatures of  $\approx 190 \text{ K}$  for the inner and  $\approx 60 \text{ K}$  for the outer component (e.g., Morales et al., 2011; Ballering et al., 2013). Applying blackbody assumptions gives a distance ratio of  $r_o/r_i = (190 \text{ K}/60 \text{ K})^2 \approx 10$ . Thus, our result is close to what was found for many other systems.

We discovered that both components must have similar dynamical excitation of  $e_{\text{max}} \approx 0.04$  to be in good agreement with the brightness profile data. One problem is that this level, especially in the inner belt, is lower than what is expected for the stirring by a planet (e.g., Mustill & Wyatt, 2009), suggesting that the gap between the two belts may not be populated by planets. In that case, however, it would be difficult to explain what else, if not planets, has cleared up the wide gap between the two belts. Nevertheless, the problem can be mitigated by the assumption that possible planets in the gap are in nearly circular orbits and/or have low masses.

An alternative explanation is that HIP 17439's disc has no gap, but is composed of a single radially extended planetesimal belt. This can be understood as a generalisation of a two-component configuration (Scenario I) because an extended belt can be approximated by several narrow belts adjacent to each other (multi-component disc). In principle, this could be the best model consistent with planet(esimal) formation theories.

# 4 AU Microscopii

*This chapter is based on the work published in Schüppler et al. (2015). I made major contributions to the collisional modelling, including the calculations of the thermal and scattered light emission of the dust. The reduction and description of the ALMA data and other observational data (Sections 4.2.2 and 4.2.3) as well as the parametric modelling (Section 4.6) was done by Steve Ertel. Other parts of this study were elaborated in collaboration with Torsten Löhne, Alexander V. Krivov, Jonathan P. Marshall, Sebastian Wolf, Mark C. Wyatt, Jean-Charles Augereau, and Stanimir A. Metchev.*

## 4.1 System description

The debris disc around AU Mic (GJ 803, HD 197481) is one of a few that have been found around M-type stars so far. Such discs seem to be rare for which there could be several reasons:

- The low luminosities of M-type stars imply colder circumstellar dust compared to grains in the same orbit around earlier-type stars. The M-dwarf discs therefore exhibit faint long-wavelength emission meaning a possible survey bias (e.g., Matthews et al., 2007).
- The blowout of dust around M stars may be favoured since they are likely to possess strong stellar winds (e.g., Johnstone et al., 2015a,b).
- The low stellar mass of M dwarfs makes it easy to strip planetesimals from their discs during close encounters with massive objects (e.g., in dense stellar clusters).
- If the generic temperatures for warm and cold disc components found for debris discs around earlier-type stars (see Section 1.2) also hold for M stars, the M-type discs will be close to their hosts, meaning a faster dynamic timescale and a quick depletion of the dust reservoir. This is also favoured by the fact that M dwarfs are older on average than other stars.

Around a dozen non-resolved M-star discs have been detected in the recent years (Forbrich et al., 2008; Plavchan et al., 2009; Chen et al., 2014). Theissen & West (2014) find a much larger number of M dwarfs showing mid-IR excesses, which can be interpreted as circumstellar dust emission. However, there are some hints that this is more likely attributed to giant impacts of terrestrial planetary bodies (Scenario IV, Section 1.2)



than to asteroid belt-like debris discs (Weinberger et al., 2011; Theissen & West, 2014). The discs around the M stars GJ 581 (Lestrade et al., 2012), TWA 7, TWA 25 (Choquet et al., 2016), and AU Mic are the only ones that have been spatially resolved thus far.

Since the discovery of AU Mic’s disc (Kalas et al., 2004; Liu et al., 2004), it remains remarkable among the sample of resolved debris discs in many respects. The disc is resolved from the optical to near-IR (Krist et al., 2005; Metchev et al., 2005; Fitzgerald et al., 2007), where it appears blue relative to the star. The disc is seen edge-on with an impressive radial extent of about 150 au. The surface brightness profiles show shallow inner slopes at small projected distances but steepen substantially beyond 35 au. In addition, asymmetries on small and large scales with several local brightness maxima and minima have been detected beyond 20 au (Liu, 2004; Krist et al., 2005; Fitzgerald et al., 2007). In the latest high-resolution image of *HST*/STIS (Space Telescope Imaging Spectrograph), Schneider et al. (2014) have found a distinct brightness enhancement above the disc midplane on the south-eastern (SE) side at about 13 au from the star. Furthermore, a disc warp is discernible on the north-western (NW) side between 13 and 45 au, opposite the SE brightness bump. There is also an NW-SE asymmetry, with the NW side brighter than the SE inside 20 au. These disc inhomogeneities hint at the existence of planetary perturbers, causing radially localised structures such as rings, clumps, and gaps through planet-disc interactions (e.g., Ertel et al., 2012b; Nesvold & Kuchner, 2015). However, there is no confirmation of planets in the AU Mic system to date (Neuhäuser et al., 2003; Masciadri et al., 2005; Metchev et al., 2005; Hebb et al., 2007; Biller et al., 2013). Alternatively, clumpy disc structures may also be due to recent breakups of large planetesimals (e.g., Kral et al., 2015). Recently, five features on the SE side monitored over several years have been found to move away from the star, two of them with velocities even larger than the local escape velocity (Boccaletti et al., 2015). This movement on unbound trajectories, together with the appearance of such features on only one side of the disc, indicates that the observed structures are necessarily recent. A physical interpretation of these observational facts with different scenarios considering gas-dust interactions, spiral density waves, resonances with planetary-mass objects, outflows from planets, or stellar activity remains challenging.

The AU Mic disc is 60% brighter in *B* band than in *I* band (Krist et al., 2005). A potential explanation is that there are many small grains down to  $\sim 0.1 \mu\text{m}$  that scatter more light at shorter wavelengths (Augereau & Beust, 2006). Graham et al. (2007) obtained polarisation maps in *V* band using the *HST* Advanced Camera for Surveys (ACS, Clampin et al., 2000). They measured the degree of linear polarisation to be

#### 4 AU Microscopii

steeply rising from 5 to 40% within a distance of 80 au. The light has a perpendicular polarisation with respect to the disc plane, which again agrees with the expected scattering behaviour by small grains.

The disc has also been resolved at 1.3 mm with SMA (Wilner et al., 2012) and ALMA (MacGregor et al., 2013). Two distinct emission components have been identified from the ALMA observations: a dust belt that extends up to 40 au and a central emission peak that remains unresolved. The dust belt shows an emission profile that rises with the distance from the star, indicating a steep mass surface density slope. The central emission peak is about six times brighter than the stellar photosphere. MacGregor et al. (2013) surmise that this emission stems from an inner planetesimal belt, located at distances  $\lesssim 3$  au. Cranmer et al. (2013) propose that it comes solely or partly from an active stellar corona.

Some studies also searched for circumstellar gas in the AU Mic disc. Liu et al. (2004) inferred an  $\text{H}_2$  mass of  $\leq 1.3 M_\oplus$  from a non-detection of submillimetre CO emission. Roberge et al. (2005) reduced the  $\text{H}_2$  mass limit to  $0.07 M_\oplus$  since far-ultraviolet (far-UV)  $\text{H}_2$  absorption was not detected. France et al. (2007) analysed fluorescent  $\text{H}_2$  emission and obtained a total gas mass between  $4 \times 10^{-4} M_\oplus$  and  $6 \times 10^{-6} M_\oplus$ . However, they state that this detection might also come from a cloud that extends beyond the disc. From X-ray spectroscopy, Schneider & Schmitt (2010) report a maximum H column density of  $\sim 10^{19} \text{ cm}^{-2}$ , which is about five times higher than the interstellar value. Thus, the AU Mic disc belongs to about a dozen known gas-containing debris disc systems, e.g., HD 172555 (Riviere-Marichalar et al., 2012), HD 21997 (Kóspál et al., 2013), HD 32297 (Donaldson et al., 2013), HD 181296 (Riviere-Marichalar et al., 2014), 49 Ceti (Roberge et al., 2014),  $\beta$  Pic (Dent et al., 2014; Brandeker et al., 2016), HD 141569 (Flaherty et al., 2016), HD 181327 (Marino et al., 2016), and several debris disc targets in the Scorpius-Centaurus OB association (Lieman-Sifry et al., 2016). These gas detections are not all as tenuous as in the AU Mic disc. Circumstellar gas has to be recently produced because of rapid dissociation times (Visser et al., 2009). Several reasons are proposed for the presence of gas in debris discs, including vaporisation of colliding dust particles (Liseau & Artymowicz, 1998; Czechowski & Mann, 2007), photodesorption of dust grains (Chen et al., 2007; Grigorieva et al., 2007b), collisions between volatile-rich comets in massive planetesimal belts (Zuckerman & Song, 2012), and evaporation of infalling comets (Beust et al., 1990).

Much work has been done in the past to characterise and model the AU Mic system. Augereau & Beust (2006) performed a direct inversion of the visible and near-IR surface

brightness profiles to calculate the circumstellar dust density. A density peak was found at around 35 au. This is close to the location of the observed break in the brightness profiles and hints at a dust-producing planetesimal belt around that distance. Strubbe & Chiang (2006) included the dynamics of grains for the first time and reproduced the scattered light profiles and the SED with a narrow birth ring of planetesimals at about 40 au. They note that the dynamics of the disc particles is dominated by destructive inter-particle collisions rather than transport processes. Their model predicts an inner disc region devoid of submicron-sized grains, which is consistent with conclusions from Graham et al. (2007) and Fitzgerald et al. (2007). In contrast, small grains mainly populate the outer part of the disc and cause the blue colour of the scattered light.

To model the  $V$ -band scattered light intensity and the degree of polarisation, Graham et al. (2007) assumed uniformly distributed dust between two distances from the star and adopted the empirical Henyey & Greenstein (1941) phase function in combination with a parameterised polarisation function. In their best-fit model, the particles exhibit strong forward scattering and the innermost 40 au of the disc are devoid of grains. Later on, Shen et al. (2009) showed that Graham et al.'s (2007) best-fit phase and polarisation functions can be reproduced by a distribution of sphere cluster aggregates with volume-equivalent radii between 0.1 and 0.4  $\mu\text{m}$ , a size distribution index of  $-3.5$ , and a porosity of 60%. Fitzgerald et al. (2007) explained many observations with a two-zone disc model in which they used power-law descriptions for the radial and the size distribution of the dust. A first zone (35...40 au) of large particles represents a planetesimal belt and mainly accounts for the long-wavelength thermal emission, while a second halo-like zone (40...300 au) is composed of small particles and reproduces the scattered light measurements. Matthews et al. (2015) also detected a dust halo in far-IR resolved *Herschel* and JCMT images. Their best fit supports the narrow birth-ring model of Strubbe & Chiang (2006), but is also consistent with an extended planetesimal belt from 8 to 40 au, according to the model explored in Wilner et al. (2012) and MacGregor et al. (2013).

In our study, we aimed at a comprehensive understanding of the dust production as well as of the dust and planetesimal dynamics in the AU Mic system. We combined constraints from scattered light and millimetre-wavelength observations and searched for a self-consistent collisional model that explains all these data. Our modelling assumed an axisymmetric disc and therefore did not account for the formation of the substructures and the asymmetries mentioned above. Furthermore, the influence of gas on disc particles was neglected because observational data point towards a very low gas content.

## 4.2 Data used

### 4.2.1 Stellar parameters

AU Mic is an M1 V dwarf at a distance of 9.9 pc (Perryman et al., 1997; van Leeuwen, 2007). The star shows strong flaring activity at X-ray and UV wavelengths (Robinson et al., 2001; Mitra-Kraev et al., 2005; Schneider & Schmitt, 2010). We used the Augereau & Beust (2006) photosphere model with an effective temperature of 3700 K, a luminosity of  $0.09 L_{\odot}$ , and a surface gravity of  $\log(g) = 4.5$ , where  $g$  is in cgs units. We assumed the stellar mass  $M_{\star} = 0.5 M_{\odot}$ , which reflects the mean of the mass range given in the literature ( $0.3 \dots 0.6 M_{\odot}$ , Plavchan et al., 2009; Houdebine & Doyle, 1994) and which is roughly consistent with the photosphere model used.

AU Mic belongs to the  $\beta$  Pic moving group (BPMG), whose members share common space motions and are believed to have a coeval origin. This implies that AU Mic's age coincides with the BPMG age. Through the identification of the lithium depletion boundary, Binks & Jeffries (2014) and Malo et al. (2014) find BPMG ages of  $(21 \pm 4)$  Myr and  $(26 \pm 3)$  Myr respectively. This agrees with traceback ages from Makarov (2007) and Mamajek & Bell (2014). The latter used revised *Hipparcos* astrometry data and also derived an isochronal age of  $(22 \pm 3)$  Myr.

### 4.2.2 ALMA observations

ALMA observations of AU Mic in Band 6 (1.3 mm) have been carried out as part of the cycle 0 early science observations in the context of the projects 2011.0.00142.S (PI: D. Wilner) and 2011.0.00274.S (PI: S. Ertel). The data considered for our modelling were taken on 16 June 2012 and are in agreement with the MacGregor et al. (2013) SB-4 observations. A total of 20 operational 12-metre antennae were used, spanning baselines of 21 to 402 m with an effective angular resolution (FWHM of the reconstructed dirty beam) of  $0.69'' \times 0.79''$  and an effective field of view of  $\lambda/d \approx 22''$ , where  $d$  is the single-dish diameter. MacGregor et al. (2013) present a detailed description of the observations and data reduction. Our re-reduction of the data was carried out with CASA. We followed the approach used by MacGregor et al. (2013) and came to consistent conclusions.

The edge-on disc has a radial extent of about  $4''$  ( $\approx 40$  au) and a position angle of  $(128.41 \pm 0.13)^{\circ}$  (MacGregor et al., 2013). It is unresolved in its vertical direction.<sup>13)</sup>

<sup>13)</sup>Our ALMA image does not provide information beyond what is shown in figure 1 of MacGregor et al. (2013) and is therefore not presented here.

To prepare the data for our modelling, we extracted a radial profile along the major axis of the disc. To this end, we largely adopted the approach used for *Herschel* data obtained in the context of the DUNES programme (Löhne et al., 2012; Eiroa et al., 2013; Ertel et al., 2014b). We first converted the flux units in the image from  $\text{Jy beam}^{-1}$  to  $\text{Jy pixel}^{-1}$  by multiplying them with a factor of 0.0185 derived by integrating the core of the reconstructed dirty beam. Then, we rebinned the image with an original pixel scale of  $0.1'' \text{ pixel}^{-1}$  to a 10 times smaller pixel scale using a cubic spline interpolation. The disc was rotated by an angle of  $38.41^\circ$  clockwise in order to align its major axis with the image  $x$ -axis. We measured the radial surface brightness profile along the major axis by integrating over  $11 \times 11$  subpixel-wide boxes centred on the disc midplane and spaced by 74 subpixels ( $0.74''$ , about the FWHM of the reconstructed dirty beam, i.e. the resolution element of the image) left and right of the star, assumed to be located at the brightest subpixel. We averaged the SE and NW sides of the profile to fit an axisymmetric model to the data. Uncertainties were derived as a quadratic sum of the difference between the two sides of the profile and the background fluctuation measured in regions of the image where no flux is expected but where the sensitivity is comparable to the image centre. Since we were only interested in the dust distribution in the outer disc, we ignored the profile point at the image centre, which is affected by the inner, unresolved component. By extrapolating the disc profile from the outer points to the disc centre and assuming that the flux measured above the extrapolated value stems from the inner component (star and additional emission), we find a flux density for this component of  $(0.29 \pm 0.05) \text{ mJy}$ , which is consistent with  $(0.36 \pm 0.07) \text{ mJy}$  in MacGregor et al. (2013). We estimated the uncertainty of this measurement by adding in quadrature a typical uncertainty in the outer points ( $\sim 15\%$ ) and an absolute photometric calibration uncertainty of 10% (MacGregor et al., 2013). The stellar contribution to this flux density is  $0.04 \text{ mJy}$ , obtained from the stellar photosphere spectrum (Augereau & Beust, 2006) extrapolated to the ALMA wavelength using the Rayleigh-Jeans (R-J) law. However, this might significantly underestimate the stellar flux and the whole central component might come from stellar emission (Cranmer et al., 2013).

Deviating from the complex fitting approach used by MacGregor et al. (2013) to derive the disc parameters (including the total flux density), we performed photometry of the disc by integrating the flux in the rotated image in a box of  $101 \times 21$  native image pixels. The uncertainty was estimated from the scatter of the flux measured on eight positions above and below the disc, where no emission is expected. An additional calibration uncertainty of 10%, consistent with MacGregor et al. (2013), was added in

quadrature. We find a total flux density of  $(8.75 \pm 0.98)$  mJy, which is consistent with  $(7.46 \pm 0.76)$  mJy from MacGregor et al. (2013), by summing both disc components and including calibration uncertainty. For the modelling, we subtracted the flux of the inner component estimated above, so that we are only left with the flux of the disc and the star as estimated using our photosphere spectrum.

The exact flux of the inner component has no significant impact on our profile or flux measurement, since we ignore the inner profile point affected by this component and because its contribution to the total flux density is only  $0.2\sigma$ .

### 4.2.3 Auxiliary thermal emission data

In addition to the ALMA data, we considered a variety of photometric data from earlier work. Furthermore, we included archival *Herschel*/PACS and /SPIRE data, taken during Guaranteed Time Observations as part of the Disc Evolution Key Programme (PI: G. Olofsson). These data were treated following the *Herschel*/DUNES data reduction strategy (Eiroa et al., 2013). HIPE (*Herschel* Interactive Processing Environment, Ott 2010) version 11 and the calibration plan versions v56 and v11 for PACS and SPIRE, respectively, were used. PACS flux densities at 70 and 160  $\mu\text{m}$  were measured with an aperture of  $20''$  and annuli for the noise measurement of  $30'' \dots 40''$  and  $40'' \dots 60''$ , respectively. The SPIRE flux density at 250  $\mu\text{m}$  was measured with an aperture of  $30''$ , and the noise was estimated in a region of the image where no emission from the disc is expected. A nearby source is visible in all *Herschel* images, peaking at 250  $\mu\text{m}$ . It is separated from the disc well at wavelengths up to 250  $\mu\text{m}$  and easily removed by a point-source subtraction. The two sources are not well separated at longer wavelengths. SPIRE flux densities at 350 and 500  $\mu\text{m}$  were measured using SExtractor (Bertin & Arnouts, 1996) and a point-source approximation (PSF photometry), since the source is unresolved at these wavelengths. Aperture corrections were applied to the measured fluxes. Instrument calibration uncertainties of 7% for PACS and 6% for SPIRE were added in quadrature to the measured uncertainty. A more detailed reduction of the *Herschel* data is given in Matthews et al. (2015), which was published after our paper Schüppler et al. (2015). Minor differences to our data exist, but all within  $2\sigma$ . These have no impact on our modelling results.

We did not consider the spatially resolved information from the *Herschel* images since the resolution is much lower than that of our ALMA image (e.g., FWHM =  $5.8''$  for *Herschel*/PACS at 70  $\mu\text{m}$  versus FWHM =  $0.74''$  for ALMA Band 6). However, we inspected the PACS data for signs of bright, warm central emission in the form of a

significantly increasing extent of the disc from 70 to 160  $\mu\text{m}$  (Ertel et al., 2014b). Such behaviour is not visible, suggesting that the inner component seen in the ALMA images indeed makes no or only a minor contribution to the fluxes at shorter wavelengths. Doering et al. (2005) report detecting the innermost disc region up to  $\approx 16$  au in diameter via  $N$ -band imaging with the Gemini South telescope. However, the disc extent along the major axis was found to be only marginally broader than the PSF and we did not take this into account in our study. Furthermore, we did not consider *Spitzer*/MIPS images because of the low angular resolution (e.g., the resolution of *Spitzer* at 24  $\mu\text{m}$  is nearly as low as that of *Herschel* at 70  $\mu\text{m}$ ). Any confusion, such as from a background galaxy, would be difficult here to disentangle from the source.

Assuming the flux density to be proportional to  $\lambda^{-\delta}$  at long wavelengths, the mean spectral index beyond 250  $\mu\text{m}$  amounts to  $\delta = 1.7$ , close to the R-J slope of a blackbody radiator ( $\delta_{\text{RJ}} = 2$ ). We fitted a blackbody curve to the far-IR excess in order to derive spectral slopes at all wavelengths. A temperature of 50 K fits the data very well, which is consistent with Rebull et al. (2008) and Plavchan et al. (2009). Interestingly, this is in the range of generic temperatures found for the outer cold belts in many two-component systems (see Section 1.2). The temperatures that were obtained for the inner belts, 150...200 K, correspond to very small distances of  $\sim 0.6$ ...1.1 au for a putative warm component in the AU Mic system. This is well below the resolution limit and leaves room for further speculations about the presence of an inner unresolved disc component.

We took the nearest tabulated values for the colour corrections listed in the literature for the instruments used and the spectral slopes of the source (star and disc) derived from this fit. The resulting colour-corrected flux densities and references for both the measurement and the colour correction are listed in Table 4.1.

#### 4.2.4 Scattered light observations

We adopted the optical and near-IR surface brightness profiles from Fitzgerald et al. (2007) and Schneider et al. (2014) as well as the measured degree of polarisation from Graham et al. (2007). We averaged all profiles over the SE and NW disc sides to attenuate the observed spatial brightness anomalies, and thus, to alleviate the comparison with our axisymmetric disc models.

**Table 4.1:** Photometry of the AU Mic disc

Wavelength [ $\mu\text{m}$ ]	Flux density [mJy]	Telescope/ instrument	Reference for flux density	Reference for colour correction
11.6	$543 \pm 60$	<i>WISE</i>	C12	W10
12	$517 \pm 30$	<i>IRAS</i>	M90	B88
18	$246 \pm 36$	<i>Akari</i>	I10	IH
22.1	$183 \pm 21$	<i>WISE</i>	C12	W10
24	$158 \pm 3$	<i>Spitzer</i> /MIPS	P09	IH
25	$244 \pm 63$	<i>IRAS</i>	M90	B88
60	$269 \pm 46$	<i>IRAS</i>	M90	B88
70	$227 \pm 27$	<i>Spitzer</i> /MIPS	P09	IH
70	$231 \pm 16$	<i>Herschel</i> /PACS	HSA	IH
100	$680 \pm 149$	<i>IRAS</i>	M90	B88
160	$172 \pm 21$	<i>Spitzer</i> /MIPS	R08	IH
160	$243 \pm 17$	<i>Herschel</i> /PACS	HSA	IH
250	$134 \pm 8$	<i>Herschel</i> /SPIRE	HSA	IH
350	$72 \pm 21$	CSO/SHARCII	C05	...
350	$84.4 \pm 5.4$	<i>Herschel</i> /SPIRE	HSA	IH
450	$85 \pm 42$	JCMT/SCUBA	L04	...
500	$47.6 \pm 3.8$	<i>Herschel</i> /SPIRE	HSA	IH
850	$14.4 \pm 1.8$	JCMT/SCUBA	L04	...
1300	$8.5 \pm 2.0$	SMA	W12	...
1300	$8.75 \pm 0.98$	ALMA	M13	...

**References.** B88: Beichman et al. (1988), C05: Chen et al. (2005), C12: Cutri et al. (2012), HSA: *Herschel* Science Archive (Matthews et al., 2015). IH: corresponding instrument hand book. I10: Ishihara et al. (2010), L04: Liu et al. (2004), M90: Moshir et al. (1990), M13: MacGregor et al. (2013), P09: Plavchan et al. (2009), R08: Rebull et al. (2008), W10: Wright et al. (2010), W12: Wilner et al. (2012). ALMA and *Herschel* data were re-analysed as described in Sections 4.2.2 and 4.2.3.

## 4.3 Modelling parameters

### 4.3.1 Stellar winds and mass-loss rate

Previous studies propose various stellar wind strengths for the AU Mic system. Strubbe & Chiang (2006) find  $\dot{M}_\star < 10 \dot{M}_\odot$ , for which their model is in good agreement with the observed SED and the  $V - H$  colour profile of the disc. Plavchan et al. (2009) estimate  $\dot{M}_\star < 50 \dot{M}_\odot$  from *Spitzer*/IRS observations. Augereau & Beust (2006) took the active nature of AU Mic into account. They find  $\dot{M}_\star \approx 50 \dot{M}_\odot$  during quiescent states and  $\dot{M}_\star \approx 2500 \dot{M}_\odot$  during flares. AU Mic spends about 10% of the time in flare phases with a typical flare duration of several minutes (Pagano et al., 2000). Averaging over quiescent and flare phases yields the mean value  $\dot{M}_\star = 300 \dot{M}_\odot$ .



For our modelling, we considered both moderate and strong wind strengths by assuming  $50 \dot{M}_\odot$  and  $300 \dot{M}_\odot$ . According to Augereau & Beust (2006), the former is a typical model where the flares are ignored while the latter is an attempt to account for the impact of the episodic stellar activity.

### 4.3.2 Material properties

Graham et al. (2007) and Fitzgerald et al. (2007) find evidence that the AU Mic dust is composed of porous aggregates containing silicate, carbon, and ice. Guided by these results, we used porous grains composed of astronomical silicate (Draine, 2003), amorphous carbon (ACH2, Zubko et al., 1996), and water ice (Li & Greenberg, 1998). The table of the ACH2 refractive index data in Zubko et al. (1996) terminates at  $\lambda \approx 1$  mm. To model photometric measurements at longer wavelengths (SMA and ALMA points), we extrapolated the refractive index data up to  $\lambda = 2$  mm by the function  $f(\lambda) = c_1 (\lambda/1 \text{ mm})^{c_2}$  with  $c_1$  and  $c_2$  being fitting parameters. This extrapolation resulted in  $(c_1, c_2) = (16.2, 0.27)$  for the real part and in  $(c_1, c_2) = (5.6, -0.26)$  for the imaginary part of the refractive index.

We generated different porous silicate-carbon-ice mixtures, given in Table 4.2, and calculated their optical constants by applying the Bruggeman (1935) mixing rule. For brevity, we use the identifiers M1 to M5 when referring to the different compositions. The sum  $\beta_{\text{rp}} + \beta_{\text{sw}}$  follows a similar dependence on grain size as shown in the right panel of Figure 2.1 for all the materials listed in Table 4.2. In case of  $50 \dot{M}_\odot$  and  $300 \dot{M}_\odot$ , the stellar winds are sufficiently strong to induce a blowout limit that terminates the lower end of the size distribution. The blowout sizes are given in Table 4.2.

**Table 4.2:** Materials used for modelling of the AU Mic disc

Identifier	Composition	$\rho$ [g cm <sup>-3</sup> ]	$s_{\text{blow}}$ [μm]	
			$\dot{M}_\star = 50 \dot{M}_\odot$	$\dot{M}_\star = 300 \dot{M}_\odot$
M1	sil33+car33+vac33	1.78	0.07	0.48
M2	sil50+car50	2.68	0.04	0.35
M3	sil25+car25+ice25+vac25	1.64	0.07	0.51
M4	sil10+car10+ice40+vac40	1.02	0.11	0.71
M5	sil15+car15+vac70	0.80	0.16	0.93

**Notes.** Numbers after material names denote their volume fraction in per cent, e.g., sil25+car25+ice25+vac25 = 25% astron. silicate + 25% amorphous carbon + 25% water ice + 25% vacuum. The bulk densities of the composites were calculated by  $\rho = \sum \rho_i f_i$ , where  $f_i$  is the volume fraction of the species, and  $\rho_i$  their densities ( $\rho_{\text{sil}} = 3.5 \text{ g cm}^{-3}$ ,  $\rho_{\text{car}} = 1.85 \text{ g cm}^{-3}$ ,  $\rho_{\text{ice}} = 1.2 \text{ g cm}^{-3}$ ).

### 4.3.3 Setups

Table 4.3 lists the ACE simulations discussed in the following sections. We used models for an outer and an inner disc component in order to explain observations for the outer resolved disc and the central emission seen by ALMA. In all simulations, we assumed the discs to be composed of planetesimals up to at least 10 m in radius with an initial radial distribution index  $\alpha_\Sigma$  for the mass surface density. For the reason mentioned in Section 3.3, the simulation time,  $t_{\text{sim}}$ , does not necessarily coincide with AU Mic’s physical age,  $t_{\text{phys}} \approx 20 \dots 30$  Myr. In all models, except the one with planetesimals between 1 and 45 au,  $t_{\text{sim}}$  was two to four times shorter than  $t_{\text{phys}}$ , which is more than enough to bring the model discs to collisional equilibrium. The initial conditions of our model discs are, however, fiducial. Different combinations of total initial mass and initial size distribution can lead to the same observed dust configuration, though after different times.

During the reviewing process of our AU Mic paper, we realised that it would be of

**Table 4.3:** Description of ACE simulations for the AU Mic disc

Com- ponent	$a_{\text{min}} \dots a_{\text{max}}$ [au]	$\alpha_\Sigma$	$\dot{M}_\star$ [ $\dot{M}_\odot$ ]	$e_{\text{max}}$	Solids	$M_{\text{d}}$ [ $10^{-3} M_\oplus$ ]	$s'_{\text{max}}$ [km]	$M(s \leq s'_{\text{max}})$ [ $M_\oplus$ ]	See Sect.
Outer	37.5...42.5	0	0	0.03	M1	1.5	0.02	0.02	
	<b>37.5...42.5</b>	<b>0</b>	<b>50</b>	<b>0.03</b>	<b>M1</b>	<b>1.7</b>	<b>0.1</b>	<b>0.05</b>	4.4.1
	37.5...42.5	0	300	0.03	M1	2.1	0.25	0.1	
	37.5...42.5	0	50	0.03	M2	2.4	0.1	0.06	
	37.5...42.5	0	50	0.03	M3	1.5	0.1	0.05	4.4.2
	37.5...42.5	0	50	0.03	M4	1.4	0.2	0.05	
	37.5...42.5	0	50	0.01	M1	1.7	0.03	0.05	4.4.3
	37.5...42.5	0	50	0.1	M1	0.6	0.1	0.03	
1...45	-1.5	50	0.03	M1	2.1	0.1	0.2	4.4.4	
Inner	2.8...3.2	0	50	0.03	M1	0.006	100	0.02	
	2.8...3.2	0	50	0.03	M3	0.005	400	0.02	4.5
	2.8...3.2	0	50	0.03	M5	0.005	400	0.02	

**Notes.** Further simulation parameters:  $Q_{\text{D},s} = Q_{\text{D},g} = 5 \times 10^6 \text{ erg g}^{-1}$ ,  $b_s = -0.37$ ,  $b_g = 1.38$ ,  $v_{\text{sw}} = 400 \text{ km s}^{-1}$  (Strubbe & Chiang, 2006), and  $\theta = 89.5^\circ$  (Krist et al., 2005). The  $(m, e, q)$  grid was specified with 1.3 bins per mass decade, 6.7 bins per eccentricity decade, 16.9 and 10.8 bins per pericentre decade for outer and inner component runs, respectively. The model marked in bold is also denoted as reference model.

particular interest for the readers to quote the initial disc masses of our simulations that are needed to match the observations after the proper age  $t_{\text{phys}}$  of the system. To estimate these initial masses, we assumed that the collisional lifetime  $T_{\text{collision}}$  of the largest bodies equals  $t_{\text{phys}}$ , enabling them to sustain sufficient dust production over that time. However, the required sizes for the largest bodies,  $s'_{\text{max}}$ , typically exceed those assumed in our simulations. We therefore extrapolated the size distributions and collisional lifetimes to derive  $s'_{\text{max}}$  such that  $T_{\text{collision}}(s'_{\text{max}}) \approx t_{\text{phys}}$ . The power-law shapes of the distributions in the metre-to-kilometre size range facilitated that extrapolation. We then determined  $M(s \leq s'_{\text{max}})$ , i.e. the total mass for all particles smaller than  $s'_{\text{max}}$ . Results are listed in Table 4.3. The values for  $M(s \leq s'_{\text{max}})$  reflect the *minimum* disc masses needed to achieve simulation times that would approach  $t_{\text{phys}}$ . Larger planetesimals and potential exo-Plutos cannot be assessed this way because their direct contributions to the collisional cascade are negligible.

## 4.4 Probing the resolved outer disc

First, we searched for a model to explain the available observational data on the resolved outer AU Mic disc, including the SED, the ALMA radial brightness profile, and the scattered light measurements. The following illustrates the influence of different parameters and their compatibility on the data.

### 4.4.1 Stellar wind strength

We performed two stellar wind runs with  $\dot{M}_* = 50 \dot{M}_\odot$  and  $\dot{M}_* = 300 \dot{M}_\odot$ , referred to as moderate and extreme stellar wind models, respectively. In addition, we started a control run without any wind activity ( $\dot{M}_* = 0$ ). Inspired by the work of Strubbe & Chiang (2006), we assumed a radially narrow planetesimal belt (PB) centred at a distance  $r_{\text{PB}} = 40 \text{ au}$  with a 5 au width. The maximum eccentricity of the planetesimals was set to  $e_{\text{max}} = 0.03$ . For the solids, we chose the mixture M1 with volume filled in equal parts by astronomical silicate, amorphous carbon, and cavities (“vacuum inclusions”).

#### Impact on thermal emission

Figure 4.1 shows SEDs and optical depths for the three models with different  $\dot{M}_*$ . The vertical height of each SED was adapted by searching for the timestep in the ACE simulations where the dust mass has an appropriate value to reproduce the observed level of thermal emission. For the SEDs, we evaluated the differences between models

## 4 AU Microscopii

and measurements by

$$\chi_{\text{SED}}^2 = \frac{1}{N} \sum_{i=1}^N \left( \frac{F_{\lambda_i}^{\text{obs}} - F_{\lambda_i}^{\text{mod}}}{\sigma_i} \right)^2, \quad (4.1)$$

where  $F_{\lambda_i}^{\text{obs}}$  and  $F_{\lambda_i}^{\text{mod}}$  are the observed and modelled flux densities at wavelength  $\lambda_i$ , and  $\sigma_i$  is the corresponding error of the measurements. To calculate  $\chi_{\text{SED}}^2$ , we considered all

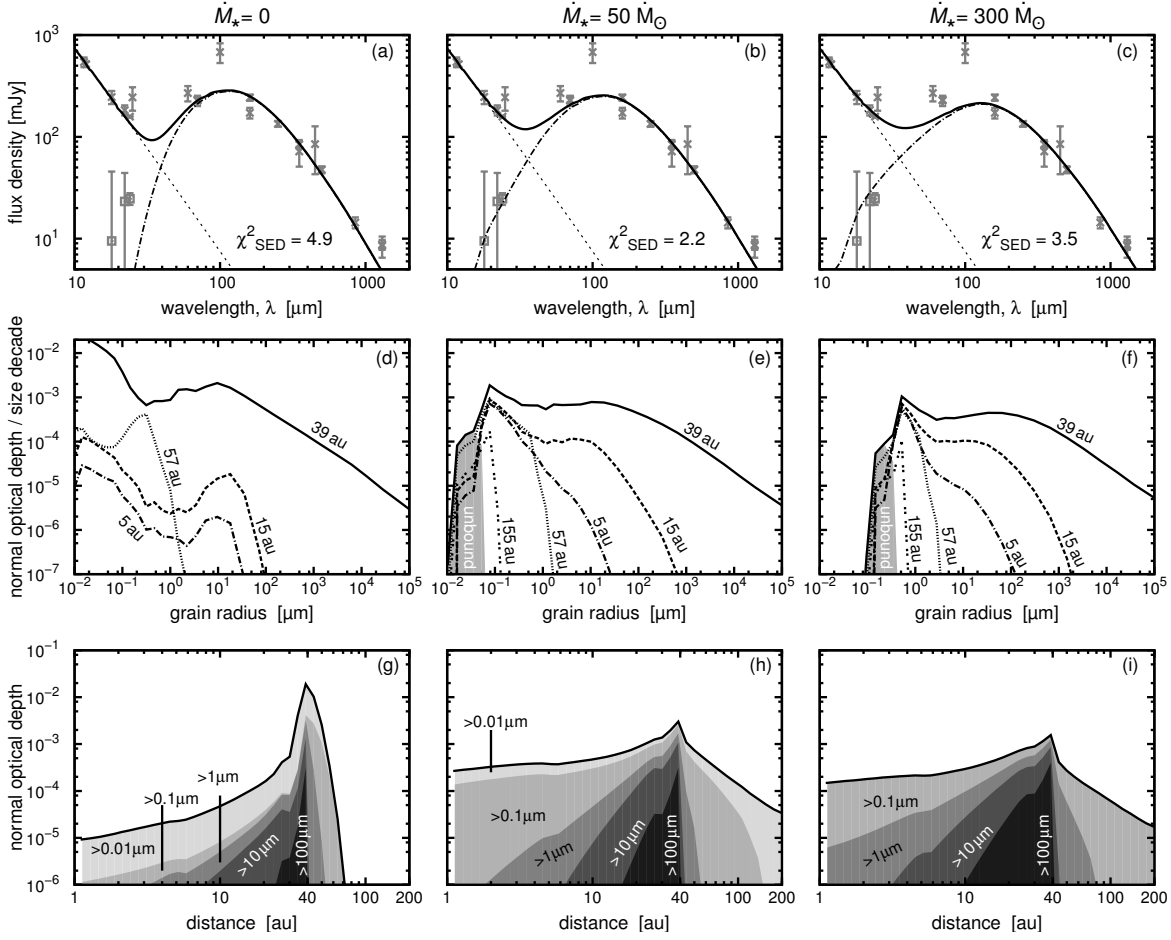


**Figure 4.1:** Disc models with different assumptions for the stellar wind strength (*from left to right*  $\dot{M}_* = 0, 50, 300 \dot{M}_\odot$ ). *Top row:* SEDs. Crosses show photometric data and squares star-subtracted photometric data. Dashed lines depict the stellar photosphere, dash-dotted lines the disc emission, and solid lines the star + disc emission. The  $\chi^2$ 's were obtained using the  $N = 20$  photometric points visible in the plotted range. *Middle row:* size distributions. Different line styles indicate different distances from the star. The solid curves ( $r = 39$  au) show the particle distribution within the planetesimal belts. Shaded regions depict the contribution of grains in unbound orbits at  $r = 39$  au. *Bottom row:* radial distributions. Shaded regions indicate the contributions from different size ranges.

measurements for  $\lambda > 10 \mu\text{m}$ , which are  $N = 20$  photometric points (Table 4.1). The  $\chi_{\text{SED}}^2$  metric merely serves as a better inter-comparison of the different SED models. It should not be understood as a sign that the models were obtained by an automatic fitting process that finds the best values for the initial disc parameters.

All models show good fidelity with the photometry between 160 and 850  $\mu\text{m}$ . They markedly underestimate or tend to underestimate the 1.3 mm data. At shorter wavelengths, moderate winds ( $\dot{M}_* = 50 \dot{M}_\odot$ ) provide a good match to the data, whereas no winds ( $\dot{M}_* = 0$ ) significantly underestimate the mid-IR points and extreme winds ( $\dot{M}_* = 300 \dot{M}_\odot$ ) the 70  $\mu\text{m}$  points.

The behaviour of the dust distributions follows the basic trends already explained in Section 3.4.2. What is new here is the occurrence of unbound grains. The size distributions for the moderate and extreme wind models show maxima near 0.07  $\mu\text{m}$  and 0.5  $\mu\text{m}$ , respectively (Figure 4.1e,f). These values are close to  $s_{\text{blow}}$  (Table 4.2). Most of the smaller grains move in unbound orbits and leave the system on short timescales. The rates of mass loss caused by blowout grains are  $\approx 1 \times 10^{-9} M_\oplus \text{ yr}^{-1}$  for moderate winds and  $\approx 3 \times 10^{-9} M_\oplus \text{ yr}^{-1}$  for extreme winds. These values roughly equal the mass-loss rates due to P-R and stellar wind drag across the grid boundaries in both simulations.

For all three runs, the mass surface density is rising with distance up to  $r_{\text{PB}}$ . Averaged over  $r = 1 \dots 30 \text{ au}$ , we measured  $\Sigma \propto r^{2.0}$  for  $\dot{M}_* = 0$ , and  $\Sigma \propto r^{2.7}$  for  $\dot{M}_* = 50 \dot{M}_\odot$  and  $300 \dot{M}_\odot$ . The latter is close to  $r^{2.8}$ , derived by MacGregor et al. (2013). The dust mass  $M_d$  is about  $2 \times 10^{-3} M_\oplus$ , consistent with previous estimates (Augereau & Beust, 2006). The three models have a fractional luminosity of  $4 \dots 5 \times 10^{-4}$ , which is not far from the  $6 \times 10^{-4}$  obtained by a modified blackbody fit (Liu et al., 2004).

Figure 4.2 shows the surface brightness profile extracted from the ALMA 1.3 mm image. The profile increases with distance up to  $\approx 30 \text{ au}$  and drops steeply beyond. Since measurements in the radio range reveal the locations of millimetre-sized particles, tracing the underlying parent bodies (e.g., Greaves et al., 2012), this break indicates the outer edge of a dust-producing planetesimal zone. For modelling the ALMA profile, we assumed the disc inclination  $\theta = 89.5^\circ$  (Krist et al., 2005) and convolved our synthetic 1.3 mm images with the ALMA reconstructed dirty beam as produced by CASA after proper rotation. We extracted the radial profiles from these images by integrating over a  $0.1''$  central strip along the disc major axis.

We allowed for vertical scaling of the gathered synthetic profiles to compensate for the imperfect reproduction of the total flux density at 1.3 mm. Significant scaling

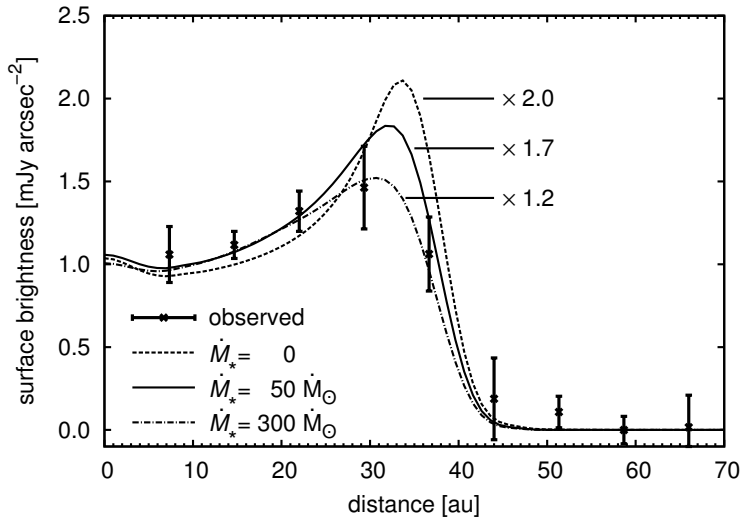


**Figure 4.2:** Brightness profiles along the major axis at 1.3 mm. Dots are measurements by ALMA, lines depict models with different  $M_*$  assumptions. Synthetic profiles have been multiplied by the factors given next to the curves to compensate for imperfections in the models and the data (see text).

factors  $\lesssim 2$  were necessary to approach the ALMA profile – a problem already visible in the SED, where the millimetre observations lie or tend to lie above the models (Figure 4.1a–c). Several different reasons might explain why the observed fluxes appear higher than predicted. First, there are issues concerning the data. This can be flux contamination by background objects. Indeed, nearby sources have been identified (Krist et al., 2005; Schneider et al., 2014), which are less easily disentangled from the actual disc at longer wavelengths. Further problems with respect to instrument calibration or data reduction can be rather excluded since measurements with two different instruments, SMA and ALMA, provide consistent results. Second, deviations may derive from an inability of our models to reproduce the millimetre flux densities. This can be due to an underprediction of the amount of dust in big particles, uncertainties in the optical properties of the dust grains (Löhne et al., 2012), or an underprediction of the stellar emission at long wavelengths by the R-J extrapolation of the PHOENIX/*Gaia* model (see also, Section 4.5).

### Impact on scattered light

We employed the formulas given in Section 2.4.2 to calculate the profiles for the scattered light and the degree of polarisation along the projected distance,  $b$ , in the disc midplane. To compare with observations from Fitzgerald et al. (2007) and Graham et al. (2007), we averaged  $S_\lambda^{\text{sca}}(b)$  and  $P_\lambda(b)$  over the  $V$ - and  $H$ -band filter transmission

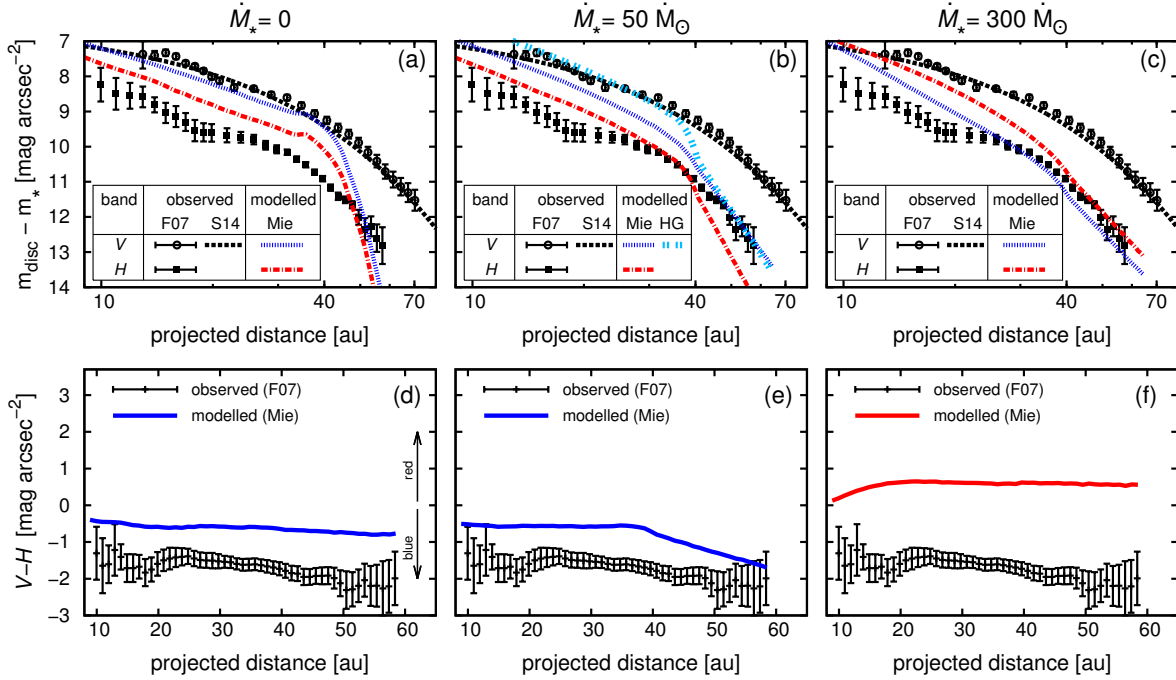
curves. We used the *HST*/ACS *V*-band filter function *F606W* (central wavelength  $\lambda_c = 0.59 \mu\text{m}$ , width  $\Delta\lambda = 0.23 \mu\text{m}$ ) and the Keck/NIRC2 (Near-Infrared Camera 2, van Dam et al., 2004) *H*-band profile ( $\lambda_c = 1.63 \mu\text{m}$ ,  $\Delta\lambda = 0.30 \mu\text{m}$ ).<sup>14)</sup> We expressed the surface brightness profiles relative to the star for which our photosphere model gives 8.55 mag in *V* band and 4.84 mag in *H* band. The flux was integrated up to  $r = 150 \text{ au}$  for each line of sight to ensure the inclusion of the extended halo. We also compared with the radial profiles extracted from the high-resolution *HST*/STIS image by Schneider et al. (2014). Their figure 39 shows the surface brightness profiles on both sides of the disc, along with exponential fits. We averaged the fits and converted the flux from  $\text{mJy arcsec}^{-2}$  to  $\text{mag arcsec}^{-2}$  using a zero-point magnitude flux density of  $3671 \text{ Jy}$ . We then subtracted a stellar *V*-band brightness of 8.837 mag, inferred from *B* and *B* – *V* values given in Schneider et al. (2014). The resulting *V*-band profile was found to be in good agreement with the Fitzgerald et al. (2007) data.

Figure 4.3 depicts the modelled and observed *V*- and *H*-band profiles, as well as the disc colour *V* – *H*. All models show significant deviations from the surface brightness data in both bands. Although roughly reproducing the observed slopes for  $b < 40 \text{ au}$ , the synthetic profiles are steeper beyond (halo zone). The profiles get shallower in the halo zone with increasing stellar wind strength. In terms of *V* – *H*, the model disc appears slightly blueish ( $V - H < 0$ ) for  $\dot{M}_\star = 0$  and  $50 \dot{M}_\odot$ , whereas it is red ( $V - H > 0$ ) for  $300 \dot{M}_\odot$ . These effects are mainly due to the distribution of small grains in the disc. Increasing the stellar wind strength pushes more small particles into the halo zone, and helps to enhance the scattered light flux beyond 40 au, thus approaching the observed level. However, the blowout size also increases and the whole disc is more and more populated by larger particles, which are stronger scatterers at longer wavelengths. The disc colour *V* – *H* therefore switches to red for winds that are too strong, clearly conflicting with the observations.

The observed increase in the degree of polarisation with distance from the star is roughly reproduced by the models with no or moderate winds (Figure 4.4). This is not seen in the extreme wind model where the polarisation is generally low. The reason for that are larger grains with radii around  $0.5 \mu\text{m}$  that dominate the size distributions (Figure 4.1f). The polarisation of such particles strongly oscillates with the scattering angle (Figure 4.5). Since we integrated the single particle polarisation function over a broad range of scattering angles along the line of sights, the integral tends to average to low values, hence  $P_\lambda(b)$  does not significantly rise with distance.

<sup>14)</sup>Filter functions were retrieved from the SVO Filter Profile Service, <http://svo2.cab.inta-csic.es/svo/theory/fps3/>

#### 4 AU Microscopii



**Figure 4.3:** Modelled and measured scattered light profiles. Models are the same as in Figure 4.1. *Top:* synthetic midplane profiles relative to the stellar brightness for  $V$  band (blue lines) and  $H$  band (red lines). Lines labelled with “Mie” were calculated with scattering phase functions from Mie theory. The double-dotted blue line in panel  $b$ ) depicts the  $V$ -band profile generated with the best-fit Henyey-Greenstein (HG) phase function model of Graham et al. (2007). Dots represent measurements with  $1\text{-}\sigma$  errors from Fitzgerald et al. (2007, F07), averaged over the SE and NW wings (circles for  $V$  band, squares for  $H$  band). Black dashed lines show the wing-averaged  $V$ -band fit, based on the Schneider et al. (2014, S14) results. *Bottom:* colour profiles  $V - H$  obtained with the F07 data and the Mie profiles shown in the top panels.

Although the moderate winds fit the measured degree of polarisation best, the data are markedly overestimated by this model for  $b < 40$  au. This is caused by particles dragged from the planetesimal belt to the inner region. Graham et al. (2007) and Fitzgerald et al. (2007) conclude that the inner region has to be relatively free of scattering grains, resulting in a low normal optical depth to scattering, defined as

$$\tau_{\lambda}^{\text{sca}}(r) = \int_s \pi s^2 Q_{\text{sca}}(s, \lambda) N(r, s) ds. \quad (4.2)$$

In  $V$  band, our moderate wind model has an inner optical depth to scattering  $\tau_{\lambda}^{\text{sca}}(r < r_{\text{PB}}) \geq 0.1 \tau_{\lambda}^{\text{sca}}(r = r_{\text{PB}})$ , which is at least two orders of magnitude greater than the limit found by Graham et al. (2007) and Fitzgerald et al. (2007).



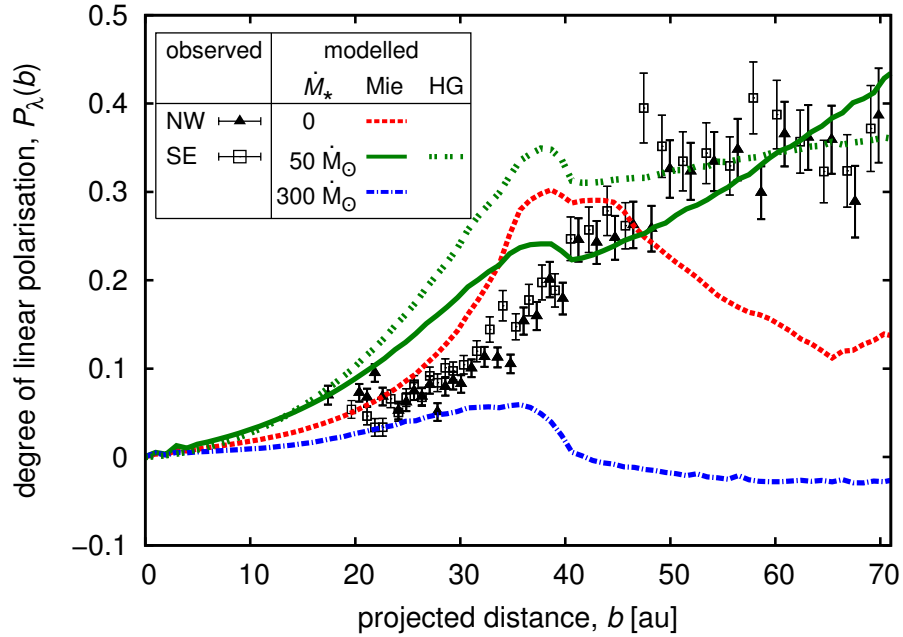


**Figure 4.4:** Degree of linear polarisation as a function of projected distance. Squares and triangles are measurements for the SE and NW ansae (Graham et al., 2007). The double-dotted green line was obtained with the Henyey-Greenstein (HG) model of Graham et al. (2007) while the other lines were calculated by Mie theory.

The inward transport of a significant amount of dust is a natural outcome in the dynamical evolution of the outer planetesimal belt. Even if planets exist at  $r < r_{\text{PB}}$ , small particles come through, because only slower, bigger particles can be efficiently scattered by planets or get trapped into mean-motion resonances (e.g., Reidemeister et al., 2011; Shannon et al., 2015). Thus, there must be another reason for the deviation between our model and the data. It might be caused by the assumption of spherical dust grains. The shapes of real circumstellar particles significantly deviate from spheres because they underwent a rich accretional and collisional history. Irregular grain shapes are well known for the Solar system’s interplanetary dust particles, which have been collected in Earth’s stratosphere (e.g., Flynn, 1994) or cometary tails (e.g., Brownlee et al., 2006). Similar particles were also produced in laboratory experiments that simulated space conditions (e.g., Wurm & Blum, 2000). Optical properties of such non-spherical grains cannot be accurately predicted by Mie theory (e.g., Pollack & Cuzzi, 1980). Although effective medium Mie spheres provide a good approximation to the total scattering cross-sections of irregular particles, they poorly fit the scattering phase function and polarisation of such grains (Shen et al., 2008, 2009). As a result, Mie theory has problems to reproduce the scattered light observations of debris discs. This was shown for HR 4796 A (Milli et al., 2015; Perrin et al., 2015) and HD 181327 disc

(Stark et al., 2014). Stark et al. (2014) also derived an empirical phase function that indicates strongly forward scattering grains. Similarly, with data taken by the *Cassini* spacecraft, Hedman & Stark (2015) find that Saturn’s rings, which are reasonable analogues to debris discs, exhibit extremely strong forward scattering. Although this can indeed be fitted by Mie theory-based calculations, it is only possible with flat size distributions and large minimum grain sizes of a few tens of microns which seem to be dubious. Hedman & Stark (2015) therefore recommend irregularly shaped particles for debris disc modelling.

In an additional test, we aimed at illustrating the effect when deviating from the simple Mie sphere dust model. To this end, we used the Graham et al. (2007) best fits for  $S_{11}$  and  $S_{12}$ , essentially inferred by applying the empirical Henyey & Greenstein (1941) model, and recomputed the  $V$ -band brightness profile and the degree of linear polarisation for  $\dot{M}_\star = 50 \dot{M}_\odot$  (double-dotted lines in Figures 4.3b and 4.4). The functions  $S_{11}$  and  $S_{12}$  of the Henyey-Greenstein (HG) model are independent of grain size, and thus all particles have the same scattering properties.

The new synthetic  $V$ -band profile fits the absolute values of the surface brightness flux better for  $b < 40$  au. The reason for this behaviour can be identified by comparing the phase functions predicted by Mie theory and the HG model (Figure 4.5, top). The HG phase function is distinctly broader than for Mie spheres with  $s > 0.5 \mu\text{m}$ . That is why bigger particles scatter more light towards the observer. This leads to the  $V$ -band flux enhancement for  $b < 40$  au and helps to approach the measurements (Figure 4.3b).

The degree of polarisation of the HG model rises too steeply for  $b < 40$  au. This is attributable to the form of the polarisation curve as a function of scattering angle (Figure 4.5, bottom). The maximum of the polarisation occurs at  $\vartheta_{\text{max}} = 90^\circ$ , so that the main contribution to the polarised light comes from particles with distances from the star nearly equal to their projected distances ( $r \approx b$ ). This overestimates  $P_\lambda(b)$  in the inner region. In contrast,  $\vartheta_{\text{max}}$  of the Mie sphere polarisation functions strongly varies with grain size, which also agrees with the trends found for irregularly shaped particles (Shen et al., 2009). With such shifts in  $\vartheta_{\text{max}}$ , the polarised light at a certain  $b$  mainly stems from particles at  $r > b$ . Furthermore, irregular grains smaller than  $0.1 \mu\text{m}$  tend to be weaker polarisers than Mie spheres in the same size range. Both may help to generate a shallower increase in  $P_\lambda(b)$ . Thus, the consideration of irregular particles in the scattered light analysis seems to be an attractive possibility for mitigating the deviations between the observed and modelled degree of polarisation.

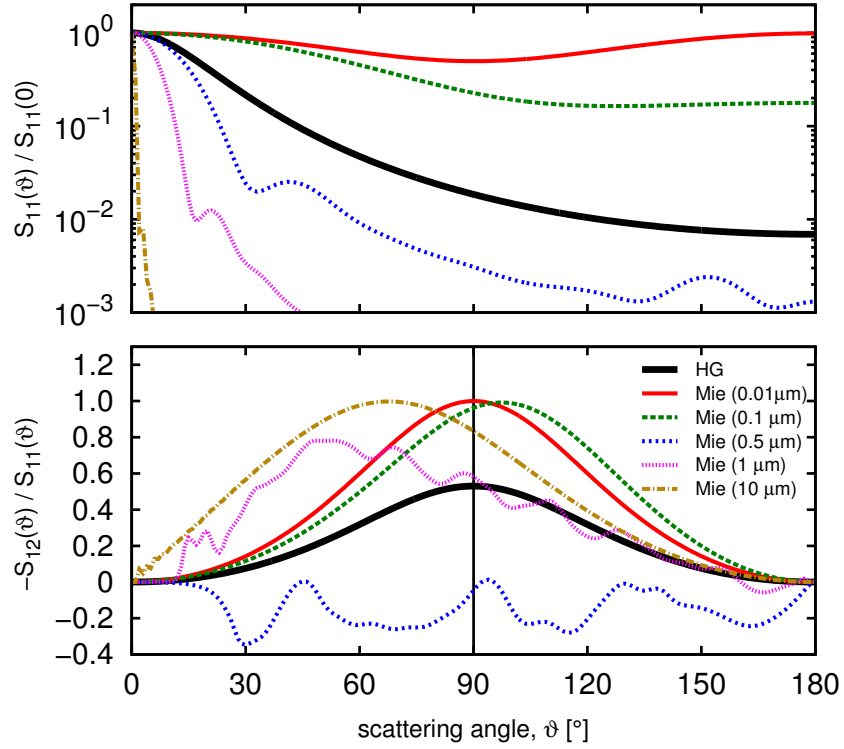


**Figure 4.5:** *V*-band scattering behaviour of single dust grains in terms of the polarisation ( $-S_{12}(\vartheta)/S_{11}(\vartheta)$ , *bottom*) and the normalised scattering phase function ( $S_{11}(\vartheta)/S_{11}(0)$ , *top*). Thick black lines have been inferred by Graham et al. (2007) via a Henyey-Greenstein (HG) model. Coloured lines are for Mie spheres of material M1. Their radii are given in parentheses.

In summary, all our models predict a larger amount of material in small grains interior to the planetesimal belt than previous studies and none of our models provides a good fit to the scattered light data. There are two ways to interpret this result: (1) Our models may predict the actual dust distribution in the disc well, but Mie theory is not valid for simulating the scattering properties of the grains. Then, our analysis shows a preference for a scattered light model where the grains are weaker polarisers than Mie spheres with  $\vartheta_{\max} \neq 90^\circ$ . (2) Mie theory is an appropriate technique for scattered light analysis, but there are shortcomings with respect to the dust density derived in the collisional modelling. The truth may also be a combination of (1) and (2). A consideration of point (1) goes along with simulating the optical properties of irregular particles – a great amount of work that was clearly beyond the scope of our study. We therefore focused on point (2) in more detail. Since the run with  $\dot{M}_* = 50\dot{M}_\odot$  was found to be in best agreement with the data, we considered it a reference model and a starting point for further parameter variations influencing the dust distribution.

#### 4.4.2 Chemical composition of solids

The chemical composition of the AU Mic disc might be similar to discs around other BPMG stars because they have formed in the same molecular cloud from the same material and are coeval. However, circumstellar objects are heavily processed during the debris disc and preceding protoplanetary disc phases. Thus, the solid composition can be changed in the course of the evolution of each individual system, depending on mass and luminosity of the host star, and may now differ from one system to another. Dust compositions have been analysed for some BPMG discs previously. Smith et al. (2009) and Churcher et al. (2011) considered grains with a silicate core and a mantle of organic refractories for SED modelling of the  $\eta$  Tel and HD 191089 systems. Particles with a porosity of 20% for  $\eta$  Tel and 60% for HD 191089 provide good fits to the observed excesses. A similar model with porous core-mantle silicate grains, additionally covered by ice when orbiting in the outer disc region, also reproduces the  $\beta$  Pic observations (Pantin et al., 1997; Li & Greenberg, 1998; Augereau et al., 2001). Lebreton et al. (2012) tested various chemical compositions for the debris around HD 181327. They find the SED to be mostly consistent with grains consisting of amorphous silicate and carbonaceous material with a dominant fraction of ice. In addition, the particles have to have a porosity of 65%.

We departed from the mixture M1, which was used in our reference run, to assess whether other materials can be viable for the AU Mic system. We repeated the ACE simulation with the compositions M2, M3, and M4 explained in Table 4.2. The material M2 represents compact particles, composed of silicate and carbon, whereas M3 and M4 also include water ice. All constituents are present in equal volume fractions in M3. The porosity and ice fraction are increased in M4 in order to bring the solid composition more in line with the highly porous and icy grains proposed for other BPMG discs. The material composition affects the dust distribution and the SED by changing the  $\beta$  values and the dust temperature (e.g., Kirchschrager & Wolf 2013, for the influence of porosity). Modifications to observables induced by the new materials are depicted in Figure 4.6.

Using M2 shifts the SED towards shorter wavelengths that deteriorates the fit in the submillimetre to radio range. The SED generated with M3 is in fairly good agreement with the observed photometry. The icier and more porous M4 produces an SED whose peak position remains rather unchanged but increases and decreases more steeply. This narrower SED distinctly deviates from the mid-IR and submillimetre measurements.

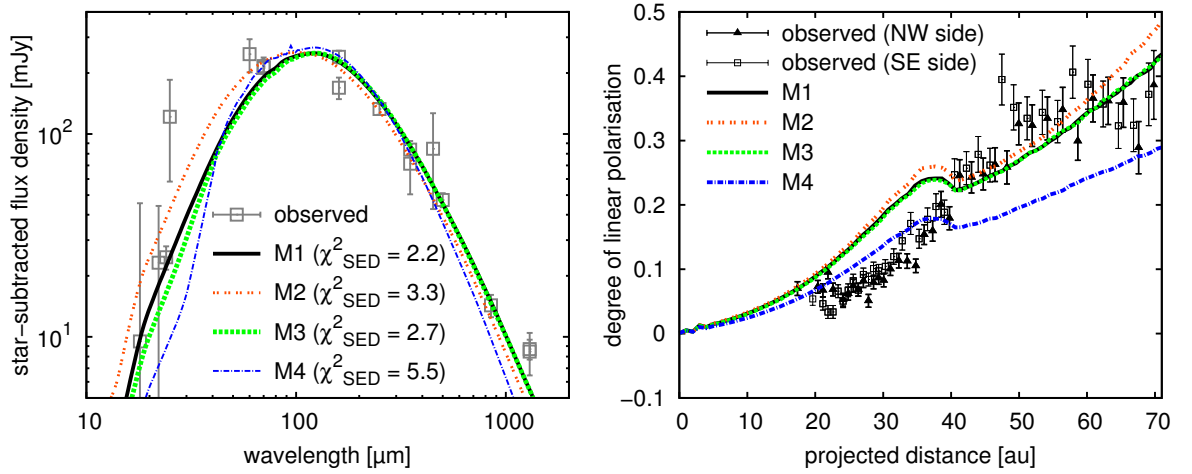


**Figure 4.6:** Influence of the dust composition on the SED (*left*) and the degree of linear polarisation (*right*). Material names are explained in Table 4.2.

No large differences in terms of the degree of polarisation are noticeable for M1–M3, whereas M4 markedly underestimates the data. The latter excludes too porous and icy dust materials. Since modelling of the degree of polarisation is possibly affected by limitations in Mie theory (Section 4.4.1), we cannot put strong constraints on the upper limit of porosity and ice content.

We noticed little changes in the radial profile at 1.3 mm for all materials considered (not shown here). This is caused by two characteristics of large grains, dominating the long-wavelength emission. First, large grains are weakly affected by stellar radiation and stellar winds, and their spatial distribution is equal for different materials. Second, the dust temperature approaches the blackbody temperature with increasing particle size at a given distance (e.g., figure 5 of Pawellek et al., 2014). Therefore, the temperatures of large grains are nearly independent from their chemical composition.

### 4.4.3 Eccentricity of planetesimal orbits

As explained in Section 3.4.2, the eccentricity of the planetesimal orbits controls the dynamical excitation of the disc and the number of small grains produced in collisions. In addition to the reference model with  $e_{\text{max}} = 0.03$ , we probed the lower value  $e_{\text{max}} = 0.01$ , reflecting the expected maximum level of pre-stirred discs (Matthews et al., 2014, and references therein), and the higher value  $e_{\text{max}} = 0.1$ , representing the dynamical excitation in the Kuiper belt (e.g., Vitense et al., 2010). Corresponding SEDs are shown in Figure 4.7.

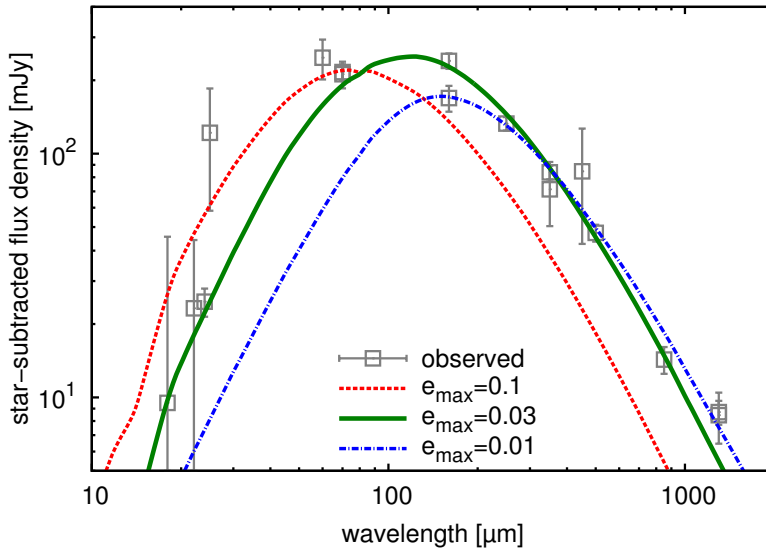


**Figure 4.7:** SED models with different assumptions for  $e_{\max}$

Increasing  $e_{\max}$  favours the production of small particles and shifts the SED maximum to shorter wavelengths. Thus, the high- $e_{\max}$  model agrees well with the excess fluxes at  $\lambda < 70 \mu\text{m}$ , but completely fails to reproduce the ones at longer wavelengths. In contrast,  $e_{\max} = 0.01$  provides a good match to the photometry beyond  $100 \mu\text{m}$ , but strongly deviates from the measurements at  $\lambda \leq 70 \mu\text{m}$ .

Improvements may be possible by additional variations of other parameters. For instance, shifting the planetesimal belt inwards (outwards) increases (decreases) the dust temperature and helps to find a better SED model for  $e_{\max} = 0.01$  ( $e_{\max} = 0.1$ ). However, any significant  $r_{\text{PB}}$ -shift would result in stronger deviations from the ALMA 1.3 mm profile, which constrains the location of a narrow planetesimal belt at around 40 au. Another possibility would be broadening the SED towards shorter wavelengths for  $e_{\max} = 0.01$ . This can be achieved by stronger stellar winds as depicted in Figure 4.1. However, stronger winds also lead to an increase in the blowout size, and therefore, make it more difficult to reproduce the observed  $V - H$  (Section 4.4.1). Furthermore, other dust materials can be used, but none of the materials investigated in Section 4.4.2 strengthens the submillimetre flux density, as required to improve the SED for  $e_{\max} = 0.1$ . Only one composition, the non-porous M2, predicts a stronger mid-IR emission from which the low- $e_{\max}$  model would benefit, but this material less agrees with the scattered light measurements. In summary, the reference run with  $e_{\max} = 0.03$  matches the entire SED the best. Although values higher or lower than 0.03 seem to be unlikely, they cannot be ruled out completely.

An observational constraint on the dynamical excitation can be put by the vertical thickness of the disc. Measuring the semi-opening angle of the disc at long wavelengths puts constraints on the maximum eccentricity of the planetesimals through the equilibrium condition  $\varepsilon = e_{\max}/2$  (Greenberg et al., 1991). However, the AU Mic disc is vertically unresolved in the SMA and ALMA images (Wilner et al., 2012; MacGregor et al., 2013), which gives only upper limits for the disc extent in this direction. We generated synthetic vertical profiles for  $e_{\max} = 0.1$  and compared them to the ones extracted from the ALMA image. The modelled profiles are marginally consistent with the ALMA data, which constrains the semi-opening angle to  $\varepsilon \lesssim 0.05$ . Interestingly, Krist et al. (2005) and Metchev et al. (2005) derived  $\varepsilon = 0.04 \dots 0.07$  from visible and near-IR images. Reading off the vertical scale height from the Schneider et al. (2014) high-resolution image (their figure 38) gives  $\varepsilon = 0.03$ . Thus, the observations yield  $e_{\max} = 0.06 \dots 0.14$  that is excluded by our modelling. Resolving this contradiction may be possible if the vertical disc thickness seen in short-wavelength images does not necessarily point towards the dynamical state of the planetesimals. Thébault (2009) proposes a model that generates a relatively high vertical disc thickness close to the observed value in the visible and near-IR, although the AU Mic disc is dynamically cold. In that model, the smallest grains have high in-plane velocities because of radiation and stellar wind pressure, and these velocities are partially converted into vertical ones in collisions with other particles. As a consequence, the disc becomes naturally thicker even without the gravitational perturbation of massive bodies, embedded in the disc. In equilibrium, the disc has a large vertical dispersion of the smallest grains, whereas big particles remain close to the midplane. Thus, a low  $e_{\max}$ , as preferred in our modelling, can still be consistent with the observed vertical disc thickness at short wavelengths.

#### 4.4.4 Planetesimal belt width

The outer edge of the planetesimal belt is well constrained by the ALMA profile. However, the edge-on orientation of the disc and the limited information on the innermost region, affected by the bright central source of unknown nature, make the position of the inner edge, hence the planetesimal belt width, very uncertain. In a further simulation, we therefore addressed the possibility that planetesimals are spread over a wide range of distances. Henceforth, we also use the notation “planetesimal disc” to reflect the broad extent of such a planetesimal distribution.

The inside-out collisional erosion of a planetesimal disc gradually clears the inner region. The disc can therefore look like a narrow belt in long-wavelength observations

(Th ebault & Augereau, 2007). This has the potential to readily explain the observed 1.3 mm profile rising with distance up to  $\approx 30$  au. The significant fall observed beyond 30 au may indicate the region where planetesimals have not formed at all or have not yet been sufficiently stirred. A truncation of the disc by external events is also a conceivable reason.

We assumed a broad radial distribution of planetesimals between 1 and 45 au. Instead of  $\alpha_\Sigma = 0$ , as assumed in our previous models with narrow planetesimal belts, we chose  $\alpha_\Sigma = -1.5$ , which reflects the mass surface density slope of the standard Minimum Mass Solar Nebula (MMSN) model (Weidenschilling, 1977; Hayashi, 1981). Furthermore, we considered bodies up to  $s_{\max} = 100$  m and assumed  $e_{\max} = 0.03$  (Section 4.4.3).

Figure 4.8 depicts the evolution of the mass surface density and the 1.3 mm profile. The mass surface density quickly drops close to the star because of particle erosion, and the initially negative slope ( $-1.5$ ) switches to a positive slope in a few ten thousand years. The collisional lifetimes of the particles are shorter than their orbital periods at the beginning of the simulation because of the high particle density at that phase. Thus, two consecutive collisions of one object are correlated, and the orbit averaging method, implemented in **ACE**, is a crude approximation for determining the phase-space density. The results for the first one hundred thousand years of simulation time should therefore be treated with caution.

Owing to the progressive inside-out depletion of the planetesimals, the maximum of the 1.3 mm profile moves towards longer distances as time elapses. After 3 Myr, we noticed that the profile peak reached a maximum distance of about 30 au, which is in good agreement with the ALMA data. The simulation has been continued until the model reproduces the observed absolute flux level. This was reached after further 26 Myr that can be understood as a settling time needed to sufficiently reduce the overall dust mass. The total simulation time therefore amounted to  $t_{\text{sim}} = 29$  Myr. We checked that the final run fits the SED, the scattered light profiles, and the degree of polarisation with nearly the same fidelity as achieved with the reference run (Section 4.4.1).

The collisional evolution of the disc was artificially shortened since the largest bodies in the disc had small sizes of 100 m. If there are larger bodies, the inside-out planetesimal depletion will be slower. As a result, it takes longer than 3 Myr to reach the observed maximum position of the 1.3 mm profile. This way, scaling the model to the proper age of the system is possible.<sup>15)</sup> However, we refrained from further simulations, because

---

<sup>15)</sup>A long-term collisional evolution model including larger planetesimal sizes is presented in Chapter 5. That model is in particular designed to reproduce observational data for  $t_{\text{sim}} = t_{\text{phys}}$ .



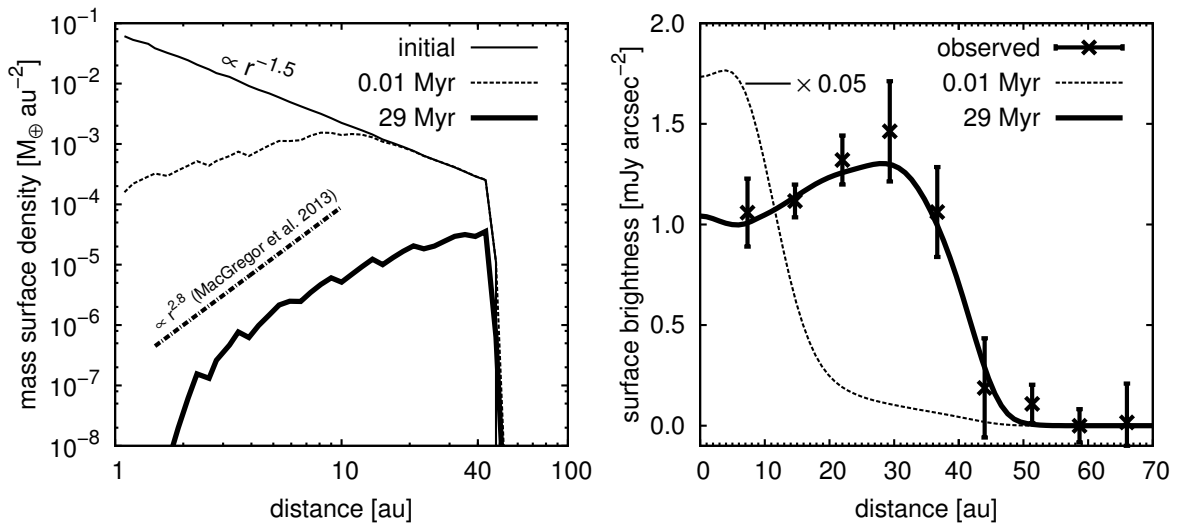


**Figure 4.8:** *Left:* mass surface density of an initially extended planetesimal distribution between 1 and 45 au at different time instants after the onset of the collisional evolution. Wavy structures of the curves are numerical artefacts. The dash-dotted line shows the slope derived by MacGregor et al. (2013) for the sake of comparison with the model. *Right:* time evolution of the 1.3 mm profile along with the ALMA data. The 0.01 Myr brightness profile was scaled by a factor of 0.05 for better visibility.

of the numerical complexity of the extended planetesimal-disc simulation.<sup>16)</sup> The run presented illustrates the possibility of an extended planetesimal disc sufficiently well. It also implies that the inner edge of the planetesimal distribution cannot be tightly constrained.

## 4.5 Probing the unresolved central emission

In Section 4.4, we did not care about the nature of the inner unresolved component detected by ALMA, and assumed that it negligibly contributes to other wavelengths. However, this might not be true if the unresolved central emission originates in an inner dust belt. Such warm dust would emit significantly at short wavelengths while adding little flux in the millimetre range. In order to test this, we considered the possibility of an additional inner planetesimal belt.

The putative inner dust belt has to emit six times more flux than the stellar photosphere at 1.3 mm (MacGregor et al., 2013, Section 4.2.2 of this thesis). Simultaneously, it has to be faint in the mid-IR in order not to contradict the measured excess there. On the other hand, the inner belt cannot be too far from the star to be compatible with

<sup>16)</sup>It took about 150 CPU days to evolve the planetesimal disc over 29 Myr.

remaining unresolved by ALMA. The ALMA resolution of  $\approx 0.6''$  ( $\approx 6$  au) constrains the inner belt location to  $r \lesssim 3$  au. We therefore placed a narrow planetesimal belt at 3 au to simulate the putative inner dust component. Almost all model parameters were the same as in our reference model for the outer disc. Only the chemical composition of the solids has been varied.

Figure 4.9 shows SEDs for several inner components. The simulations were evolved as long as needed to match the excess fluxes at  $\lambda \leq 24 \mu\text{m}$ . We assumed two inner rings with solids made of M1 and M3 – materials we found suitable for the outer component (Section 4.4.2). The belts are not bright enough to completely reproduce the central emission at 1.3 mm. Although M3 enhances the SED maximum, the long-wavelength slope is steeper and the model has the same flux density at 1.3 mm as for M1.

In another attempt, we considered highly porous grains (M5), motivated by the following. The assumed inner planetesimal belt is close to, but still beyond the ice line. Blackbody assumptions yield the ice-line distance  $r_{\text{ice}} = (L_{\star}/L_{\odot})^{0.5} (T_{\text{subl}}/277 \text{ K})^{-2}$  au. The typical ice sublimation temperature for debris discs  $T_{\text{subl}} = 100$  K (Kobayashi et al., 2008) results in  $r_{\text{ice}} \approx 2$  au. Thus, the inner belt at 3 au can produce icy dust grains that subsequently drift towards the star by drag forces. Accordingly, the grains get heated

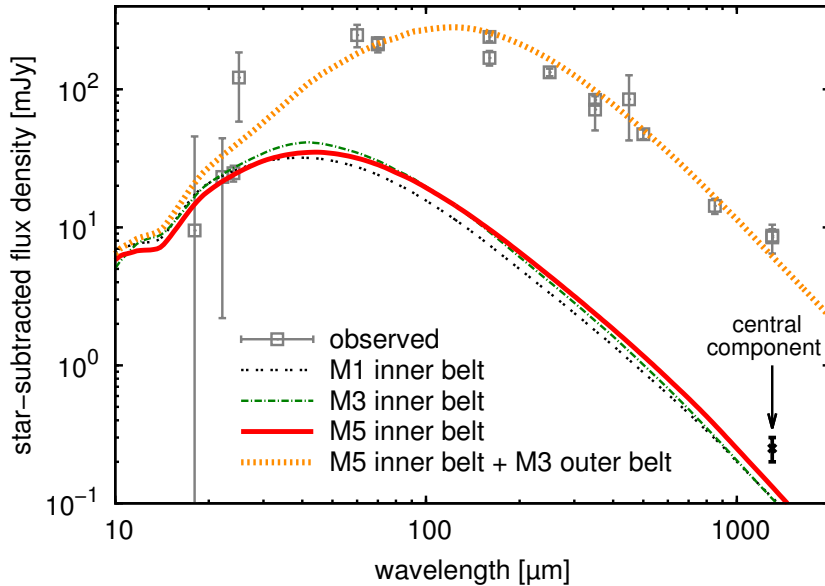


**Figure 4.9:** SED models of inner planetesimal belts centred at 3 au with the material compositions M1, M3, and M5 (Table 4.2). The data point in the right lower corner shows the emission of the 1.3 mm central emission component with  $1\text{-}\sigma$  uncertainty. The dotted orange line depicts the sum of the M3 outer belt, shown in Figure 4.6, and the M5 inner belt.

and cross the ice line. Then, their sublimated ice fractions are replaced by vacuum inclusions, meaning an increase in porosity.

The material M5 emits slightly more than M1 and M3 in the millimetre regime, but reproduces only about 60% of the observed central flux density. This constrains the maximum percentage of the central emission that can be explained by pure dust emission. Thus, the central emission must originate either totally or partially in another source. The star itself can contribute to the central emission, for instance, because of an active stellar corona (Cranmer et al., 2013). Furthermore, stars may emit more flux at long wavelengths than predicted by the purely photospheric models for their spectral class. ALMA observations of the G- and K-type stars  $\alpha$  Cen A and B show a flux enhancement by 20...30% in Band 7 and an almost doubling of the flux in Band 3 (Liseau et al., 2015, 2016). Provided such a trend continues to an M dwarf like AU Mic, we do expect a significant stellar contribution to the observed central emission.

To generate the total SED, we simply added an appropriate model for the outer disc. In doing so, we did not account for the collisional interaction between inner and outer component. This is justified because there is only a weak mutual overlap of the local densities from both components (see also explanations in Section 3.5). Combining the M3 outer belt (Section 4.4.2) and the M5 inner belt provides a good match to the whole SED (Figure 4.9, dotted orange line). This combination of an iceless inner component, which contains highly porous grains, and an icy outer component is also reasonable because of the position of the ice line, as explained above. The outer disc SED was adopted from the model described in Section 4.4.2 without any adjustments (e.g., vertical scaling). Thus, the inner emission barely affect the SED modelling of the outer disc.

## 4.6 Comparison with classic modelling

Finally, we checked the compatibility between results from collisional and classic modelling (cf. Section 1.3). For classic modelling, we applied the multi-dimensional fitting approach already described in Section 3.1. In this approach, we fixed  $s_{\max}$  to 2 mm and  $\theta$  to  $90^\circ$ . For the dust composition, we assumed compact, spherical grains composed of pure astronomical silicate. This makes a total of eight free parameters:  $r_1$ ,  $r_2$ ,  $\alpha_\tau$ ,  $s_{\min}$ ,  $\gamma$ ,  $M_d$ , the dust composition (sampled by only one value, namely 100% astronomical silicate), and the vertical scaling of the ALMA profile. For the fitting of the SED and the ALMA profile, we used the `SAnD` code (Ertel et al., 2012a; Löhne et al., 2012), which was originally developed for fitting simultaneously SED data and spatially re-

#### 4 AU Microscopii

solved *Herschel* data as part of the *Herschel*/DUNES modelling tool box. We did not include the scattered light data for this classic modelling.

In a first approach, we fitted the model to the data neglecting the contribution of the central component. The best-fit model (Table 4.4) reveals features we already found, at least qualitatively, by collisional modelling: an outward-increasing dust density with  $\alpha_\tau = 2.8$ , a well-constrained outer disc radius at about 40 au, a small lower grain size  $s_{\min} < 1 \mu\text{m}$  consistent with a moderate level of stellar winds, and a relatively shallow slope of the size distribution,  $\gamma = -3.3$ , indicating that small particles are more affected by transport than collisions. Furthermore, the results are widely consistent with previous studies (Augereau & Beust, 2006; MacGregor et al., 2013).

In a second approach, we assumed that the inner component is an additional ring of dust. The ring was placed at 2 au with an extent of 0.2 au. For this inner component, we assumed a constant surface density, and explored the lower grain size,  $s_{\min,i}$ , and the size distribution index,  $\gamma_i$ , by hand. The model was scaled to the flux density of the central component seen in the ALMA data. A very large lower grain size,  $s_{\min,i} = 5 \mu\text{m}$ , as well as a very flat grain size distribution,  $\gamma_i = -3$ , is necessary in order to keep the dust cold enough (the grains large enough) not to produce too much excess at mid-

**Table 4.4:** Power-law fitting results for the (outer) AU Mic disc

Parameter	Range explored	# values	Distr.	Best fit [ $3\sigma$ ]	+ inner
$r_1$ [au]	2...60	187	temp	3.1 <sup>†</sup> [2.0 <sup>†</sup> , 24.8]	14.5
$r_2$ [au]	3...100	155	temp	41.9 [37.3, 45.5]	41.9
$\alpha_\tau$	-5...5	101	lin	2.8 [1.8, 4.8]	3.5
$s_{\min}$ [ $\mu\text{m}$ ]	0.2...20	494	log	0.2 <sup>†</sup> [0.2 <sup>†</sup> , 0.5]	1.8
$s_{\max}$ [ $\mu\text{m}$ ]	2000	1	fixed	...	...
$\gamma$	-5...-3	21	lin	-3.3 [-3.4, -3.3]	-3.3
$\theta$	90°	1	fixed	...	...
$M_d$ [ $M_\oplus$ ]	...	...	cont	$4.7 \times 10^{-3}$	$5.7 \times 10^{-3}$

**Notes.** Distributions of the values considered in the parameter space are: *temp* – by equal steps in temperature of the grain size with the steepest radial temperature gradient, *lin* – linear, *log* – linear in the logarithm of the parameter, *fixed* – fixed value (no distribution at all), *cont* – continuous (scaling of the disc mass to minimise the  $\chi^2$  for given values of all other parameters). Values marked with <sup>†</sup> are at (or very close to) the boundaries of the parameter space explored and cannot be considered as reliable. The real values may lie outside the parameter space explored. The column “+ inner” shows best-fit values of the outer disc after subtracting a model of the inner, unresolved component, assuming it to be a debris disc. These values illustrate the uncertainties of the model parameters due to the unknown nature of the inner component.

to far-IR wavelengths. The fitting result, even the large lower  $s_{\min,i}$ , does not strictly speak against a debris disc nature of the unknown inner component. A large lower grain size is naturally expected if the grains experience a very low blowout limit as is the case for AU Mic. Then, the dominant grain size,  $s_c$ , is the one where collisional and transport lifetimes are equal, which can be reached at much larger sizes. Including the effect of stellar wind drag in equation (6) of Kuchner & Stark (2010) and assuming an optical depth of  $10^{-3}$  at 3 au, which is consistent with our M5 inner-belt model, yields a critical size  $s_c \approx 3 \mu\text{m}$  that is not far from  $s_{\min,i} = 5 \mu\text{m}$ .

In a final step, we subtracted the contribution of the inner ring from the SED data and re-fitted the remaining flux by the model used for our first approach (Table 4.4, last column). The values are almost all within the  $3\text{-}\sigma$  interval of the first fit. This demonstrates that the inner component marginally influences the modelling of the resolved outer disc, as already found by collisional modelling.

## 4.7 Conclusions and discussion

Our modelling shows good consistency with Scenario II (Section 1.2). We can explain most of the data with a single planetesimal belt with an outer edge around 40 au and subsequent inward transport of dust by moderate stellar winds. Although being narrow, the planetesimal belt may originate in an initially extended planetesimal disc whose inner region has been eroded collisionally, as demonstrated in Section 4.4.4.

The outer belt may coexist with an inner unresolved debris belt, which is suggested by the central emission component in the ALMA 1.3 mm images. As noted in MacGregor et al. (2013), future ALMA observations at higher resolution should be able to detect an inner planetesimal belt. If confirmed, this might argue against the possibility of a very extended planetesimal disc under the assumption that the innermost planetesimals cannot survive the inside-out collisional erosion of such a disc. However, this assumption remains controversial because some models would explain the presence of an inner belt even after the collisional depletion of an extended planetesimal disc. For example, the innermost bodies could have a higher mechanical strength, since they are likely to be less icy, and thus, they would resist the collisional grinding more strongly.

To test the hypothesis of an inner component, we added an inner belt at  $\approx 3$  au, which is below the ALMA resolution limit. Our inner belt models are not able to fully explain the observed central emission at 1.3 mm. Instead, it should at least partly derive from other mechanisms. A cometary population or stochastic collisional events, corresponding to

#### 4 AU Microscopii

Scenarios III and IV (Section 1.2), may deliver warm inner dust, detectable at long wavelengths. The latter is supported by the recently confirmed transient nature of some AU Mic disc features (Boccaletti et al., 2015). Furthermore, the star itself may be an additional source of emission (e.g., coronal emission, Cranmer et al., 2013). Most recently, MacGregor et al. (2016) published Very Large Array observations of the AU Mic system at 9 mm. They find a highly variable emission with an increase up to 150% compared to continuum brightness. A stellar activity model fits this relative flux enhancement and simultaneously matches the observed X-ray flare amplitudes. Thus, MacGregor et al. (2016) conclude that there is no need for an asteroid belt analogue to consistently explain the observational data.

If future observations detect planets in the AU Mic disc, this will imply an outer planetesimal distribution that is rather narrow than extended since planets at distances  $< 40$  au are likely to clear the inner region. Indeed, the disc can harbour several yet undetected planets. To make predictions of AU Mic's planetary system, we assume that there is an inner and an outer planetesimal belt separated by a gap. Although an inner belt is not the only explanation for the observed central emission component, its presence cannot be ruled out completely. We estimate the minimum mass and the number of planets between the both components needed to open a gap with equations (4) and (5) recently published by Shannon et al. (2016). Assuming a stellar age of 25 Myr, an inner disc at  $a_1 = 3$  au, and an outer one at  $a_2 = 37$  au gives a minimum planetary system that consists of three super-Neptunes having  $\approx 25 M_{\oplus}$  each. Since our modelling shows an uncertainty for the position of the inner edge of the outer planetesimal belt, it is reasonable to assume smaller values for  $a_2$ , which reduces the required minimum planetary masses. Thus, even Earth-like planets are consistent. In all cases, the planet masses are much higher than the inferred minimum mass of the planetesimal disc (Section 4.3.3). Thus, planetesimals do not cause migration of planets and Shannon et al.'s (2016) formulas are truly applicable. The present-day observational facilities allow us to detect planets down to one Jupiter mass ( $\approx 300 M_{\oplus}$ ) in the AU Mic disc (Metchev et al., 2005; Fitzgerald et al., 2007), which provides an upper mass limit. Thus, we can expect planets between a few and few hundreds of Earth masses. Putative planets are also likely to be in lowly eccentric orbits since our modelling shows a clear preference for a low dynamical excitation of planetesimals. This also agrees with conclusions of MacGregor et al. (2013). In their ALMA image, they find a small centroid offset between the outer planetesimal belt and the stellar position of  $\sim 1$  au that might be imposed by secular perturbations of a wide-orbit planet with an eccentricity of 0.05.

# 5 q<sup>1</sup> Eridani

*This chapter shows the work published in Schüppler et al. (2016). I performed the collisional modelling. Results and implications were discussed in conjunction with Alexander V. Krivov, Torsten Löhne, Mark Booth, Florian Kirchschrager, and Sebastian Wolf.*

## 5.1 System description

Among the debris discs observed with *Spitzer* and *Herschel*, the one around the nearby Gyr-old F8 V star q<sup>1</sup> Eri (HD 10647, HIP 7978) is outstanding for having a strong IR excess with a fractional luminosity of about  $2 \dots 3 \times 10^{-4}$  (Trilling et al., 2008; Eiroa et al., 2013). The disc has been spatially resolved in the far-IR (Liseau et al., 2008, 2010) and in the scattered light (K. Stapelfeldt, private communication). The images reveal a bright disc with a radius of  $\sim 100$  au. The mid-IR *Spitzer*/IRS spectrum between 20 and 30  $\mu\text{m}$  (Chen et al., 2006) clearly hints at the presence of an additional warm debris component, which is unresolved in the images. The fractional luminosity of the warm component is  $\sim 10^{-4}$ , which is only a factor of several lower than that of the main disc. Attempts to reproduce the data with a two-component model require the warm dust to be located at several au from the star (Tanner et al., 2009; Pawellek & Krivov, 2015). Apart from the two-component disc, a Jupiter-mass planet with  $a_{\text{pl}} = 2$  au and  $e_{\text{pl}} = 0.15$  has been detected by radial-velocity (RV) measurements (Butler et al., 2006; Marmier et al., 2013). The region inside the planetary orbit seems to be largely free of dust as there is no detection of near-IR excess, associated with the presence of hot exozodiacal dust (Ertel et al., 2014a).

Explaining the architecture of the q<sup>1</sup> Eri disc is a challenge. Since q<sup>1</sup> Eri is an F star, we do not expect stellar winds on a sufficiently high level to deliver the amount of material needed to explain the observed warm dust emission (Scenario II, Section 1.2). Little impact of stellar winds on circumstellar debris around F stars is also suggested by Mizusawa et al. (2012). In their investigated sample, they find no difference in excess detection rate between early-type F stars, which have radiative envelopes and probably no winds, and late-type F stars, which have convective surfaces and coronal-driven winds. Therefore, q<sup>1</sup> Eri might have a Solar system-like architecture with two planetesimal belts and invisible planets in between (Scenario I). However, this explana-

tion is questionable, too. It is well known that the fractional luminosity of a debris belt collisionally evolving in a steady-state regime cannot exceed a certain value for a given age of the system and distance from the star (Wyatt et al., 2007a; Löhne et al., 2008). That limit is more stringent for older systems and for belts closer to the star where the collisional decay is faster. Assuming plausible parameters, the model by Wyatt et al. (2007a) suggests that the warm dust in the  $q^1$  Eri disc may be indeed too bright, and the system too old, to be compatible with a steady-state collisional cascade in an asteroid-like belt. However, other mechanisms providing warm dust like a recent major collision between two big planetesimals (Scenario IV) come with the caveat that such events in Gyr-old systems may not be likely either.

The following presents a collisional evolution model to explain the formation of the  $q^1$  Eri disc components self-consistently. The goal was to see whether a sufficient amount of material can survive in the inner region of the system against collisional depletion to reproduce the available observational data.

## 5.2 Long-term collisional evolution model

### 5.2.1 Extended planetesimal disc

We first considered the long-term collisional evolution of an initially extended planetesimal disc, which we assumed to be a likely remnant of the planetesimal formation process. In this section, the focus lies on understanding of the general features predicted by our collisional evolution model. We therefore generated a representative setup by using a set of standard assumptions that are not yet adjusted to the  $q^1$  Eri system.

We assumed a planetesimal distribution between 1 and 100 au around a star with  $L_\star = 1.5 L_\odot$ . The planetesimal distribution had an MMSN-like solid surface density  $\Sigma = 1 M_\oplus \text{ au}^{-2} (r/\text{au})^{-1.5}$  (Weidenschilling, 1977; Hayashi, 1981). In contrast to our previous works (Chapters 3 and 4), the disc was filled with large planetesimals up to 100 km in radius. We set the orbital eccentricities of the planetesimals to a mean value of 0.05, in agreement with values expected for discs around solar-type stars (e.g., Pawellek & Krivov, 2015). We assumed the material parameters  $Q_{D,s} = Q_{D,g} = 5 \times 10^6 \text{ erg g}^{-1}$ ,  $b_s = -0.37$ , and  $b_g = 1.38$ . Beside planetesimals, also smaller bodies were already present within the disc at the beginning of the simulation. The initial size distribution index was  $\gamma = -3.7$ , which is the equilibrium value for an infinite collisional cascade with the dust parameter  $b_s$  (O'Brien & Greenberg, 2003). The equilibrium index for large objects is different since  $b_g \neq b_s$ . However, the particular choice of  $\gamma$  does not



really matter, since the simulation promptly drives the system to an equilibrium size distribution that does not depend much on the one assumed initially. This comes with the caveat that the kilometre-sized and larger planetesimals in the outer disc do not reach a collisional equilibrium by the end of the simulation and may retain their primordial distribution, set by their formation process (which is poorly known anyway). The smallest particles considered in the simulation had radii of  $\approx 0.5 \mu\text{m}$  that corresponds to  $s_{\text{blow}}$  of silicate grains around an F-type star (see, Figure 2.1, left panel). Since we aimed at explaining the  $q^1$  Eri disc, for which the dust transport is assumed to play a minor role, no drag forces were taken into account.

Top panels in Figure 5.1 depict the evolution of the mass surface density ( $\Sigma$ ) and the normal optical depth ( $\tau$ ), as functions of distance from the star. While  $\Sigma$  reflects the distribution of kilometre-sized, massive bodies,  $\tau$  traces the distribution of micron-sized dust grains that dominate the cross-section. This difference is best illustrated by considering the region beyond 100 au. In this zone,  $\Sigma$  is negligible, whereas  $\tau$  shows a halo that contains small grains with radii slightly above  $s_{\text{blow}}$ .

Bottom panels in Figure 5.1 depict the size distributions close to the inner (4 au) and outer (94 au) edge of the planetesimal disc. The size distributions exhibit a wavy pattern which is more pronounced towards the dust size range ( $s < 1 \text{ mm}$ ), since there are no grains below  $s_{\text{blow}}$  that could work as destructive projectiles (Campo Bagatin et al., 1994; Krivov et al., 2006; Thébault & Augereau, 2007; Wyatt et al., 2011).

Both the radial profiles and the size distributions change with time. This evolution is described and discussed in detail below, and we start with the initial stage. The top right panel of Figure 5.1 reveals an extremely high initial optical depth ( $> 10$  at 1 au), in the innermost region of the disc. It arises because ACE takes the initial slope of the  $\Sigma$  profile and populates the disc initially by small, micron-sized grains in accord with the power-law size distribution  $s^{-3.7}$ . However, as explained above, that power law tacitly assumes that the system has an equilibrium distribution of an idealised, infinite collisional cascade from the very beginning. Obviously, this assumption is not valid for a debris disc right after its birth. Instead, the initial distribution of dust in a young debris disc must be the one set by physical processes that operated in the preceding protoplanetary disc by the time of the gas dispersal. On any account, ACE gets rid of the “unphysically” overabundant dust particles swiftly and the optical depth drops to the equilibrium values after a few thousand years. Already at 1 Myr, the  $\tau$  curve in Figure 5.1 is flat, regardless of the profile assumed initially.

The subsequent disc evolution depends on the collisional lifetimes of the particles

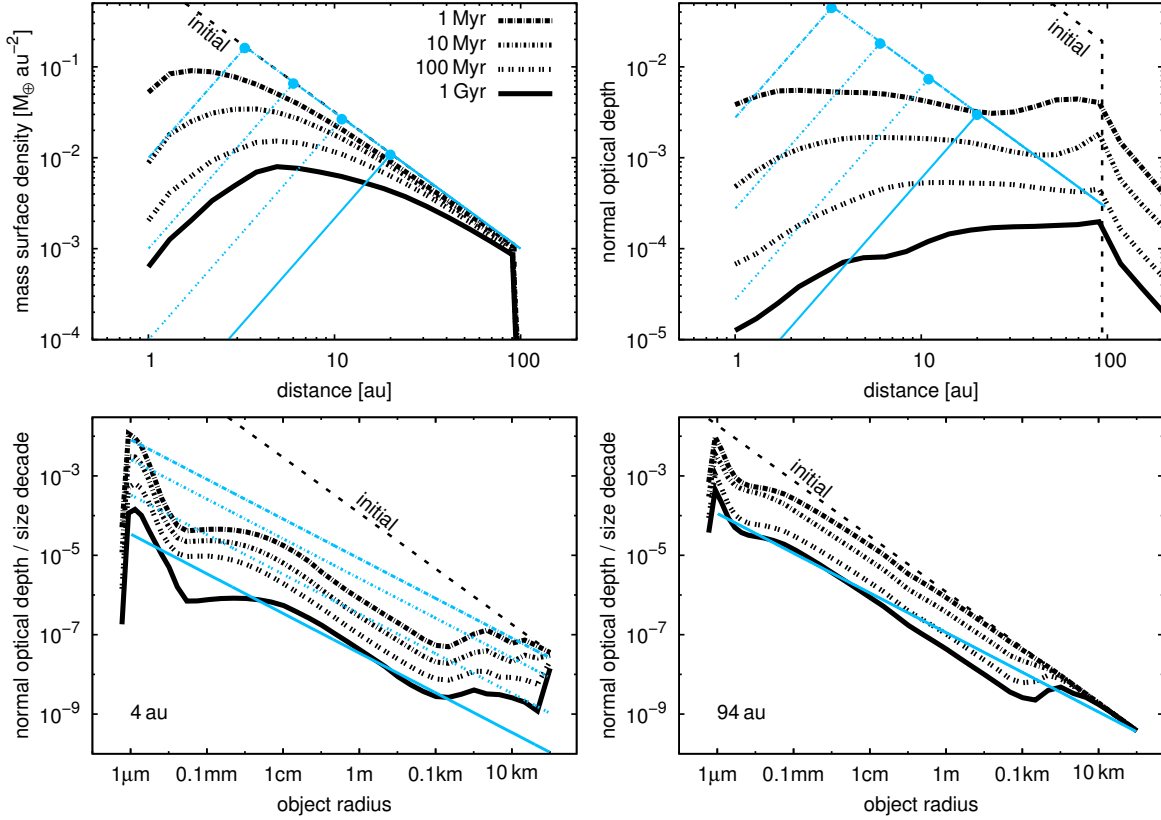


**Figure 5.1:** Radially extended planetesimal belt at different time instants after the beginning of the collisional evolution. Thick black lines are ACE results, thin blue lines represent the model of Wyatt et al. (2007a). *Top:* radial profiles of the mass surface density (*left*) and the normal optical depth (*right*). The blue dots on the straight lines indicate the distances where the collisional lifetime of the largest planetesimals equals the current system age. Beyond these distances the lines turn into the initial profiles. *Bottom:* size distributions in terms of optical depths at 4 au (*left*) and 94 au (*right*). At 94 au, the lines of the Wyatt et al. (2007a) model are the same at all time instants, since the collisional depletion of the largest planetesimals at that distance has not yet started by 1 Gyr.

and can be understood as follows. Since collisional lifetimes get longer with increasing particle size and distance from the star, modifications of the size distributions go from small to large objects and from inner to outer disc regions. The small dust that dominates the optical depth depletes and reaches collisional equilibrium first, larger objects follow. As a result, at times shorter than the collisional lifetime of the largest objects at a given distance,  $\tau$  decreases faster than  $\Sigma$  does. It is this gradual inside-out, bottom-up transition of the size distribution from the initial to the quasi-equilibrium state combined with the initial radial distribution that explains why the radial profiles of  $\tau$  are almost flat, even though the  $\Sigma$  profiles are not.

Once the lifetimes of the biggest objects are reached at a given distance, the local size distribution keeps its shape, while  $\Sigma$  and  $\tau$  both deplete with their mutual ratio staying constant. After tens of Myr, material is sufficiently eroded to generate positive slopes of both  $\Sigma$  and  $\tau$  in the inner regions.

After 1 Gyr, almost all material is reprocessed and only the largest planetesimals in the outer disc have not yet started to deplete collisionally and follow their primordial size distribution. This is seen for objects larger than 10 km at 94 au.

For the sake of comparison, the analytic steady-state evolution model of Wyatt et al. (2007a) is overplotted in Figure 5.1. Their model was designed to describe the evolution of a narrow debris ring, but can readily be applied to an extended debris disc, assuming it to consist of non-interacting concentric annuli (Kennedy & Wyatt, 2010). To enable direct comparison, we converted the maximum disc mass  $M_{\max}$  and the maximum fractional luminosity of the dust  $f_{\max}$  of Wyatt et al. (2007a) to the surface density and the normal optical depth:

$$\Sigma = \frac{M_{\max}}{2\pi r \Delta r}, \quad \tau = 2 \frac{r}{\Delta r} f_{\max}, \quad (5.1)$$

where  $\Delta r$  is the planetesimal belt width. We also calculated the evolution of the size distributions with equations (1), (13), and (14) of Wyatt et al. (2007a).

The parameters of the Wyatt et al. (2007a) model were chosen in such a way that it matches the ACE run as closely as possible. Accordingly, all parameters that are shared by the analytic model and the ACE simulation were set to the same values. These include the stellar mass and luminosity, the initial disc mass, the eccentricity of the planetesimal orbits, and the diameter  $D_c$  of the largest planetesimals in the collisional cascade.

There are two important parameters, however, for which the best choice is less obvious. One is the slope ( $2 - 3q$ ) of the size distribution, which varies with particle size in the ACE simulation (wavy pattern of the size distribution). We assumed  $q = 11/6$ , or  $2 - 3q = -7/2$ . Another parameter is the specific disruption energy  $Q_D^*$ , which must be independent of size in the Wyatt et al. (2007a) model. We chose  $Q_D^* = 10\,000 \text{ J kg}^{-1}$ , which is representative for two different particle populations. Indeed, since  $Q_D^*$  used in ACE has a V-like shape in a log-log scale with a minimum at around 100 m, any constant value above this minimum intersects the two branches in the small and large particle size range. The assumed value of  $10\,000 \text{ J kg}^{-1}$  corresponds to the material strength of planetesimals with a few tens of kilometres in radius as well as of millimetre-sized

grains. The latter are important sources for the production of yet smaller dust that mainly determines the optical depth. Thus, our choice of  $Q_D^*$  ensures that particles from the lower and upper end of the wide size range are taken into account.

As can be seen in Figure 5.1, the **ACE** simulation predicts a significantly higher mass surface density at later times than the analytic model of Wyatt et al. (2007a). This is a consequence of a slower depletion of the planetesimals best visible in the size distributions at 4 au. In contrast to the analytic reference, the **ACE** simulation involves a size-dependent  $Q_D^*$ . The lifetimes of the largest planetesimals are longer, because their  $Q_D^*$ 's exceed the value of  $10\,000\text{ J kg}^{-1}$  adopted in the analytic model by a factor of several. Furthermore, the  $Q_D^*$ 's of the planetesimals increase with object size as a result of self-gravity. The latter effect enhances the abundance of larger planetesimals relative to their disruptive projectiles. The slope of the resulting steady-state size distribution of the largest planetesimals flattens with respect to that in the strength regime (O'Brien & Greenberg, 2003). Thus, at later times, the **ACE** simulation retains a reservoir of large planetesimals that is more massive and is able to sustain a given optical depth or dust mass for a longer period of time than the analytic model.

### 5.2.2 Two narrow planetesimal belts

In a second step, we considered the evolution of a disc whose radial structure was additionally sculpted by the formation of planets. The primary effect of giant planet formation, which we only take into account here, is the opening of a planetary gap that splits up the disc. Since such a gap is already produced before the debris disc phase, it can be incorporated in our model by a suitable choice of the initial density profile.

Accordingly, we generated a debris disc with an inner and an outer planetesimal belt that are spatially separated. To this end, we cut out two regions of the extended planetesimal disc presented in the previous section. The inner disc was assumed to lie between 3 and 10 au, the outer disc between 70 and 100 au (ranges for the semi-major axes of planetesimals). Other initial parameters were the same as explained for the extended disc. In particular, the initial surface density of both belts followed the MMSN description. The two belts were then evolved with two independent **ACE** runs.

Figure 5.2 compares the two-component system with the extended disc. At any given age, the surface densities in the two models are very close (Figure 5.2, top left). There are, however, some deviations between the shape of the size distributions in the two models, especially in the outer zone (Figure 5.2, bottom right). These deviations are

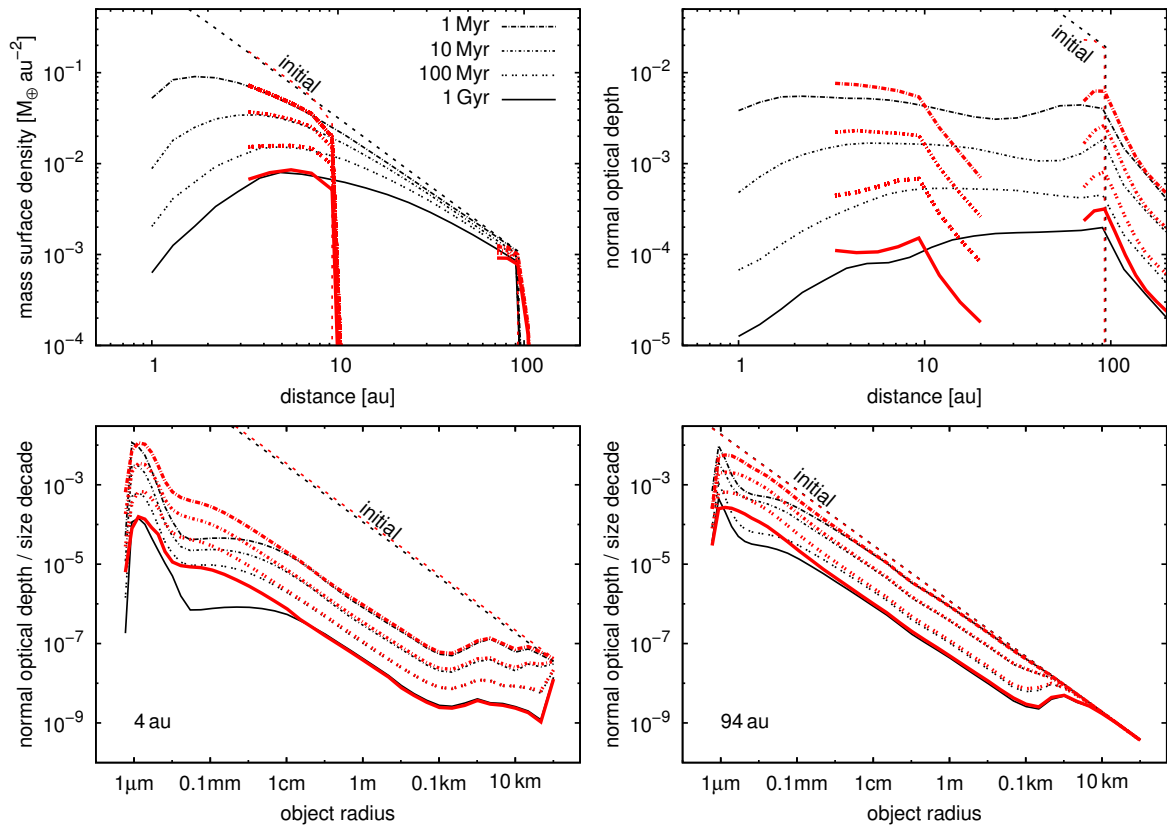


**Figure 5.2:** Evolution of a two-component disc in comparison with that of an extended one. Thin black lines correspond to the radially extended planetesimal model presented in Figure 5.1. Thick red lines show two narrow planetesimal belts between 3... 10 au and 70... 100 au.

related to the collisional interaction of different disc regions. In the extended disc model, the dust grains with sizes just above the blowout size, produced at a certain distance, are sent by radiation pressure to eccentric orbits, and therefore, enter the outer disc zones where they collide with the local material. This causes an overabundance of grains just above the blowout limit, which enhances the depletion of larger grains. This effect favours the formation of distinct dips in the size distributions, as seen around  $5 \mu\text{m}$  at 94 au. Since the two-component model simulates the two belts independently, such a collisional interaction is neglected, and so, the dips are absent. As a consequence, the planetesimal belts of the two-component model tend to have somewhat higher optical depths than in the extended disc simulation (Figure 5.2, top right).

We emphasise that our model treats the evolution of the inner and outer planetesimal belts self-consistently since both originate in a common initial surface density profile. Possible interactions with one or more planets within the gap, which separates the

two components, are not directly included. However, such interactions can be taken into account through the choice of initial disc parameters. For instance, the gap width reflects the number and mass of planets.

## 5.3 Application to $q^1$ Eri

### 5.3.1 Stellar parameters

$q^1$  Eri is at a distance of 17.4 pc (van Leeuwen, 2007). We took the following stellar parameters from the *Herschel*/DUNES final archive<sup>17)</sup> (Eiroa et al., 2013):  $L_* = 1.5 L_\odot$ ,  $T_* = 6155$  K,  $M_* = 1.12 M_\odot$ ,  $[\text{Fe}/\text{H}] = -0.04$  (metallicity),  $\log(g) = 4.48$  (cgs units). We adopted the photosphere model from Eiroa et al. (2013), obtained by an interpolation in the PHOENIX/*Gaia* model grid (Brott & Hauschildt, 2005) with a normalisation to optical and *WISE* fluxes. Age estimations of  $q^1$  Eri span a wide range, from 0.3 to 4.8 Gyr (Liseau et al., 2008, and references therein). The strength of chromospheric activity and the luminosity in X-rays suggest that the star is  $\gtrsim 1$  Gyr old.

### 5.3.2 Observational data

Photometric data were collected from the *Herschel*/DUNES archive and the literature. From the set of available data, we used the measurements that are at least  $1\sigma$  above the stellar photosphere model, thus indicating the IR excess (Table 5.1). A *Spitzer*/IRS spectrum, reduced by the c2d *Spitzer* Legacy Team Pipeline (Young et al., 2005), was also taken from the DUNES archive.

In addition, we extracted radial brightness profiles from the *Herschel*/PACS images provided in the DUNES archive. At 70, 100, and 160  $\mu\text{m}$ , cuts were performed along the minor and major axes of the observed disc, with position angles of  $144^\circ$  and  $54^\circ$  east of north, respectively. The stellar position was assumed to coincide with the intensity-weighted centroid of the disc. Profiles of the minor and major axes were obtained by averaging the two sides of the disc. Uncertainties in intensity are dominated by differences between opposing branches of both axes, added in quadrature to a minor contribution from background noise that was estimated from an annular aperture. The resulting profiles and error bars are depicted in Figure 5.3. Horizontal error bars reflect the bin widths in the underlying images:  $1''$  at 70 and 100  $\mu\text{m}$ ,  $2''$  at 160  $\mu\text{m}$ .

<sup>17)</sup><http://sdc.cab.inta-csic.es/dunes/jsp/homepage.jsp>

**Table 5.1:** Photometry of the  $q^1$  Eri disc

Wavelength [ $\mu\text{m}$ ]	Flux density [mJy]	Telescope/ instrument	Reference
18	$315.3 \pm 39.7$	<i>AKARI</i>	(1)
22	$218.1 \pm 4.0$	<i>WISE</i>	(1)
24	$184.8 \pm 3.8$	<i>Spitzer</i> /MIPS	(1)
25	$201.1 \pm 26.1$	<i>IRAS</i>	(1)
60	$617.4 \pm 80.3$	<i>IRAS</i>	(1)
70	$896.2 \pm 26.9$	<i>Herschel</i> /PACS	(1)
90	$904 \pm 60$	<i>AKARI</i>	(4)
100	$897.1 \pm 26.9$	<i>Herschel</i> /PACS	(1)
160	$635.9 \pm 31.8$	<i>Herschel</i> /PACS	(1)
250	$312.3 \pm 25.6$	<i>Herschel</i> /SPIRE	(1)
350	$179.9 \pm 14.6$	<i>Herschel</i> /SPIRE	(1)
500	$78.4 \pm 9.8$	<i>Herschel</i> /SPIRE	(1)
850	$30.3 \pm 4.1$	JCMT/SCUBA-2	(6)
870	$39.4 \pm 4.1$	APEX/LABOCA	(3)
1200	$< 17$	SIMBA/SEST	(2)
6800	$0.093 \pm 0.017$	ATCA	(5)

**References.** (1) Based on data from the DUNES Archive at Centro de Astrobiología (Eiroa et al., 2013). (2) Schütz et al. (2005). (3) Liseau et al. (2008). (4) Yamamura et al. (2010). (5) Ricci et al. (2015b). (6) Holland et al., in preparation.

### 5.3.3 Modelling results

As mentioned before, the  $q^1$  Eri system shows strong indications for harbouring a two-component debris disc. We performed additional tests to confirm that the presence of a warm component is certain. One test was to vary the effective temperature of the star by  $\pm 100$  K, which is the scatter in the literature values (Nordström et al., 2004; Chen et al., 2006). For each stellar temperature, we generated a photospheric model and then fitted two-component disc models to the SED, assuming the dust distributions to follow power laws (see model description in Section 3.1). The warm components we inferred were moderately different. However, in all the cases a warm component was clearly needed to explain the data. Another test was to overplot the  $q^1$  Eri system in figure 5 of Kennedy & Wyatt (2014) that presents a  $\chi^2$  map, which has been calculated from fitting a single-temperature blackbody (i.e., a one-component disc) to fiducial two-temperature (i.e., two-component) discs. We find  $q^1$  Eri to lie close to the contour

line  $\chi_{\text{red}}^2 \approx 20$ , meaning that this system is highly inconsistent with a one-component structure. Finally, we estimated an uncertainty in the normalisation of the photospheric model to the optical and *WISE* fluxes to be about 2%. A two-component fitting similar to that described above, but with the photospheric model made by 2% brighter, also showed that the warm component was needed to reproduce the SED.

Given these results, we applied the *ACE*-based two-component model presented in Section 5.2.2 to explain the SED and the *Herschel* surface brightness profiles of the  $q^1$  Eri system. We assumed the stellar properties as described in Section 5.3.1 and simulated a set of several two-component models where we varied the following parameters: the location, width, and initial mass (in terms of the MMSN multiples) of the inner and outer components, the eccentricities of the planetesimal orbits, the size of the largest planetesimals, and the chemical composition of the disc particles. For the purpose of surface profile modelling, we generated synthetic images from the *ACE* models at 70, 100, and 160  $\mu\text{m}$  with a position angle of  $54^\circ$  (east of north). We convolved the synthetic images with  $\alpha$  Boo PSFs, which were rotated by  $83^\circ$  counter-clockwise to align them with the telescope position angle during the observations.

We aimed at finding one plausible model that agrees with the observations reasonably well. We probed various maximum orbital eccentricities of planetesimals (0.03, 0.05, and 0.1) and their largest radii (50 and 100 km). Inner and outer edges of the inner planetesimal belt were varied between 3 and 20 au, and those of the outer belt between 65 and 135 au. We assumed dust particles to be a mixture of astronomical silicate and water ice and chose the volume fraction of ice to be a free parameter. Ice fractions of 0, 50, 70, and 90% were explored.

We finally achieved the model presented in Figure 5.3. The corresponding parameters are summarised in Table 5.2. The model profiles overpredict the 160  $\mu\text{m}$  emission in the central region by  $\approx 20\%$ . This can reflect some inaccuracy of the collisional model. Also, the modelled SED predicts (sub)millimetre flux densities to be by a factor of two to three lower than those measured by LABOCA, SCUBA-2, and ATCA. Since the images from SCUBA-2 (Holland et al, in preparation) and LABOCA (Liseau et al., 2008) are extended eastwards, the most likely reason for the discrepancy is a background galaxy. The flux densities plotted are aperture fluxes. The peak fluxes – for instance,  $(20.1 \pm 2.7)$  mJy  $\text{beam}^{-1}$  of the SCUBA-2 measurement – are more in line with the model prediction. Overall, the resulting is satisfactory for the purposes of our study.

The initial surface density of both components corresponds to 5.3 times the MMSN model. The position of the outer component is consistent with the ring-like disc found



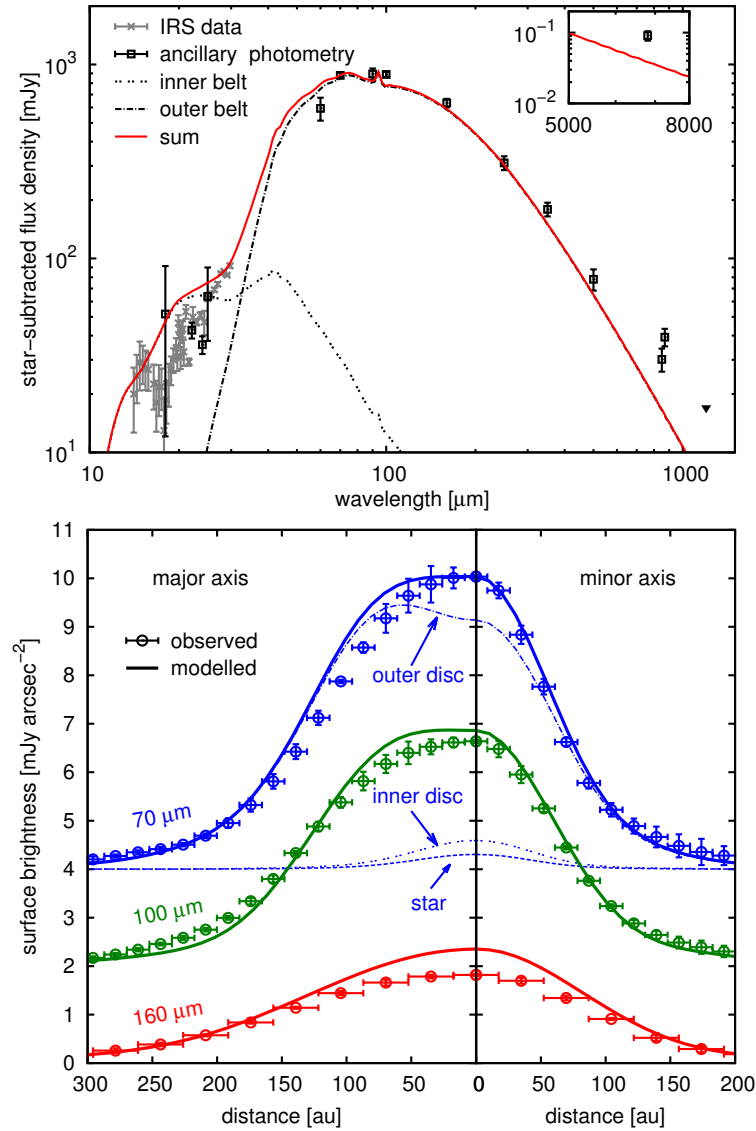


**Figure 5.3:** A two-component model found in satisfying agreement with observational data (dots). *Top:* full SED (solid) along with contributions from the inner (dotted) and outer (dash-dotted) component. The inset in the upper right corner shows how the model matches the ATCA measurement at 6.8 mm. *Bottom:* brightness profiles across the minor and major axes for 70 (blue), 100 (green), and 160  $\mu\text{m}$  (red). For 70  $\mu\text{m}$ , contributions of the star (dashed line), inner component (dotted), outer component (dash-dotted), and the sum of all three (solid) are shown. At 100 and 160  $\mu\text{m}$ , only the total profiles are depicted since they come almost entirely from the outer component. For better visibility, profiles at 70 and 100  $\mu\text{m}$  were shifted vertically by constant values of +4 and +2  $\text{mJy arcsec}^{-2}$ , respectively.

through a deconvolution of the *Herschel* 100  $\mu\text{m}$  image by Liseau et al. (2010). They quote a surface brightness maximum at 85 au and a belt width of about 35 to 45 au. The location of the inner disc is beyond the orbit of the reported RV planet HD 10647b.

**Table 5.2:** Parameters of the two-component model shown in Figure 5.3

Com- ponent	$a_{\min} \dots a_{\max}$ [au]	$s_{\max}$ [km]	$e_{\max}$	Solids [sil:ice]	$\theta$ [ $^\circ$ ]	$\tau$ [ $10^{-4}$ ]	$M_d$ [ $M_\oplus$ ]	$M_{\text{disc}} (M_0)$ [ $M_\oplus$ ]	$t_{\text{sim}}$ [Gyr]
Inner	3...10	50	0.05	30%:70%	70	1	$1.5 \times 10^{-5}$	3.4 (95)	1.3
Outer	75...125					10	$1.7 \times 10^{-2}$	81.7 (167)	

**Notes.** The optical depth in the sixth column is measured at the centres of the planetesimal belts. The eight column give the initial mass in parentheses and end mass of the whole planetesimal disc (bodies up to  $s_{\max}$  in radius). Grid resolution parameters: 1.2 bins per mass decade, 5.1 bins per eccentricity decade, 8.0 and 29.0 bins per pericentre decade for inner and outer components, respectively.

Although there is a large gap between both components, the overall synthetic surface brightness profiles show no signs of a dip and are close to the observed ones. The best disc inclination is  $70^\circ$ , which is close to  $76^\circ$ , the value inferred from the *HST* scattered light image (K. Stapelfeldt, private communication).

The planetesimal orbits have eccentricities  $\leq 0.05$ , which implies relatively low impact velocities in the disc and a rather depressed production of small dust. However, planetary stirring is likely to operate in the inner component, which is close to HD 10647b. There is also the possibility that further, yet undiscovered, planets in the gap between both planetesimal belts enhance the eccentricities in the outer component. Higher values of the eccentricity are not excluded by our modelling since there are degeneracies between the eccentricity and other model parameters (see Section 5.4).

The dust composition determines the grain temperatures and emission properties. During the modelling process, we noticed that the rise of the SED in the mid-IR shows a strong dependence on the ice fraction. This allows us to improve the agreement with the characteristic bump (“shoulder”) that is exhibited by the IRS spectrum in the 10 to 30  $\mu\text{m}$  range. Larger fractions of ice reduce the emission of the inner component, whereas the one of the outer component remains nearly unchanged. This is due to the fact that the mid-IR emission mostly comes from small grains ( $s \simeq 1 \dots 10 \mu\text{m}$ ), while the far-IR emission is produced by larger grains ( $s > 10 \mu\text{m}$ ) with an emissivity that is not strongly dependent on the chemical composition. The higher the ice fraction, the steeper the rise of the total SED. However, the distinct silicate feature around 18  $\mu\text{m}$  is still well pronounced and is able to reproduce the bump seen in the IRS spectrum. A mixture of 30% silicate and 70% water ice for inner and outer component provides a good overall match to the SED and the surface brightness profiles.

## 5.4 Conclusions and discussion

We explored the long-term collisional evolution of a two-component disc whose origin is based on Scenario I (Section 1.2). Our detailed collisional simulations revealed that the inner disc may be able to retain larger amounts of material at older ages than thought before on the basis of the analytic Wyatt et al. (2007a) model.

Our models can explain the two-component structure observed in the  $\alpha^1$  Eri disc. Other scenarios as described in Section 1.2 appear unlikely because of, e.g.,  $\alpha^1$  Eri’s old age and spectral type F8. To verify Scenario I, it will be crucial to resolve the proposed inner belt. At  $0.17'' \dots 0.57''$ , the inner belt would be difficult to see with the *HST* because of its large inner working angle. The latest extreme adaptive optics instruments, such as the “planet finder” SPHERE on the VLT (Beuzit et al., 2008), allow us to image much closer to the star. For instance, SPHERE/IRDIS (Infra-Red Dual Imaging and Spectrograph, Dohlen et al., 2008) has an inner working angle of  $0.15''$  in its standard mode, opening up these regions to scattered light observations for the first time. We performed a test by generating scattered light radial profiles of the inner belt at  $1.6 \mu\text{m}$ . We compared the profiles with the IRDIS detection limit provided by the SPHERE Exposure Time Calculator<sup>18)</sup>. The surface flux along the major axis,  $\sim 0.2 \text{ mJy arcsec}^{-2}$ , is about three orders of magnitude below the detection limit. For SPHERE/ZIMPOL (Zurich IMaging POLarimeter, Thalmann et al., 2008) with a smaller working angle at  $0.55 \mu\text{m}$ , the inner belt could be traced along the minor axis where it appears brighter in polarised light,  $\sim 4 \text{ mJy arcsec}^{-2}$ . However, even in that case we are still one order of magnitude below the detection limit. This indicates a big challenge in resolving the inner belt with present-day observational facilities. However, the coming *James Webb Space Telescope* (Gardner et al., 2006) might offer better chances for such a detection.

The proposed two-component scenario also implies a set of alleged planets between the inner and outer belts. The number of planets is unknown, as are their orbits and masses. Nevertheless, rough estimates can be made by assuming that the presumed planets are in nearly-circular, nearly-coplanar orbits with a uniform logarithmic spacing of semi-major axes (Faber & Quillen, 2007). The set of planets should be tightly packed dynamically to ensure that no dust-producing planetesimal belts have survived between the orbits, while the planets themselves should be at least marginally stable against mutual perturbations over the age of the system of  $\sim 1 \text{ Gyr}$ . Using equations (3) and

<sup>18)</sup><https://www.eso.org/observing/etc/>

(6) of Faber & Quillen (2007), we estimate that the cavity between  $\sim 10$  au and  $\sim 80$  au could be populated by four to five planets of at least Neptune mass, with a semi-major axis ratio between neighbouring planets of  $\sim 1.6$ , similar to the orbital radius ratio of Earth and Mars in the Solar system. The minimum total mass of these planets would amount to  $\sim 0.2$  Jupiter masses.

There are currently two planetary systems known to have an architecture similar to the one proposed for  $q^1$  Eri. One is our own Solar system. Another is the prominent system around HR 8799, with its four directly imaged massive planets (Marois et al., 2008, 2010), an outer massive Kuiper-like belt exterior to and an inner debris belt interior to the planetary orbits (e.g., Reidemeister et al., 2009; Su et al., 2009). However, there are also fine differences between these cases. The  $q^1$  Eri system is known to contain a close-in Jupiter-mass RV planet whereas our Solar system harbours four terrestrial planets. Around HR 8799, no planets have been discovered so far inside the inner dust belt. It is interesting to note that the known planet of  $q^1$  Eri system is orbiting at  $\sim 2$  au, whereas the proposed inner belt must be located farther out, at 3 to 10 au. Thus, the belt was likely located outside the ice line when it formed which, assuming an ice sublimation temperature at the protoplanetary phase of 170 K (Lecar et al., 2006), must have been at  $\sim 3.3$  au from the star. This means that the planet could have comfortably formed in the zone interior to the asteroid-like belt. No migration through the belt is required here – unlike in the systems such as HD 69830 where the planets and the belt are all located inside the ice line (Payne et al., 2009).

Owing to numerous degeneracies, the model found in our study is by far not unique. For instance, we cannot constrain tightly a set of gas or icy giants that separates the two components, and consequently, it is unknown to what degree these would stir the components. However, we expect that at least the inner component is rather strongly affected by the known nearby giant planet HD 10647b which is on a close-in ( $a_{\text{pl}} \approx 2$  au), eccentric orbit ( $e_{\text{pl}} \approx 0.2$ ). Equation (6) of Mustill & Wyatt (2009) yields a forced eccentricity of  $\sim 0.1$  that could be imposed by HD 10647b on planetesimals at 5 au. This is a rough estimate since only one planetary perturber is assumed, but it shows that the inner planetesimal disc may have a distinctly higher level of dynamical excitation than assumed in our model. If so, there would be a faster collisional depletion, resulting in a lower amount of material in the inner disc. However, the size of the largest planetesimals and their  $Q_{\text{D}}^*$  are not well constrained, too. If there are larger and harder planetesimals within the disc, the collisional depletion will be slower, which might ensure that the inner system contains sufficient dust after  $\sim 1$  Gyr to explain

the observations. The collisional timescales can also be prolonged if the inner disc were located farther out and/or had a larger width.

Furthermore, the slope of the assumed initial density profile of a protoplanetary disc is completely uncertain (e.g., Kuchner, 2004; Raymond et al., 2005; Chiang & Laughlin, 2013). Steeper profiles are preferred for in-situ formation scenarios of close-in giant planets, where the disc mass is more centrally concentrated.

In our model, the dust of both components contains 30% silicates and 70% water ice, which is another crucial point. Since, in contrast to protoplanetary discs, the gas pressure in debris discs is negligible, ice sublimates at lower temperatures of  $\sim 100$  K (Kobayashi et al., 2008), suggesting the ice line for blackbody grains to lie at  $\sim 10$  au. However, the predicted inner component lies between 3 and 10 au. Thus, the presence of icy grains in the inner component is questionable. Other materials, e.g. porous silicate, for the inner component may be a better choice. This agrees, at least qualitatively, with the compositional model of Tanner et al. (2009).

# 6 Conclusive remarks

## 6.1 Summary

This thesis presents the modelling of spatially resolved debris discs with the statistical approach of kinetic theory, referred to as collisional modelling. This approach starts from a circumstellar distribution of parent planetesimals and predicts their subsequent collisional evolution, i.e. the way how planetesimals are ground down to tiny dust grains as a function of time. The resulting dust distributions at a given time instant are used to compute the observables, which are then compared with actual observational data. In this way, one can access undetectable planetesimals which bear the imprints of the planet formation process. This is opposed to the classic modelling that merely probes the dust portion of debris discs by means of analytic expressions from empirical considerations.

We used the collisional modelling code **ACE** that provides generic radial and size distributions of debris disc material. Beside mutual collisions, it considers the effects of pressure and drag forces from stellar radiation and stellar winds working on circumstellar debris. The code was applied to reproduce and interpret the observed features of the debris discs around HIP 17439, AU Mic, and  $\alpha^1$  Eri for the first time. Adapting the model to observational data was challenging since we varied the parameters of the parent planetesimals and not the ones of the observed dust. In general, several time-consuming **ACE** simulations on a trial-and-error basis were necessary to change the dust distribution in a desired way. The models presented in this thesis required a total simulation time of  $\sim 1300$  CPU days. However, this value does by far not include the calculation time for the numerous test runs, which did not lead to satisfying results and which are not shown in this work.

Observations hint at a two-component configuration for all three systems. We considered two scenarios capable of explaining the origin of two-component configurations: 1. an inner and an outer component of planetesimals as asteroid and Kuiper belt analogues (Scenario I), and 2. an inner component composed of dust transported towards the star from an outer planetesimal belt (Scenario II). The three selected debris discs have been tested for consistency with these scenarios. Furthermore, we obtained information not only on dust and planetesimals, but also on stellar properties that could not have been derived from classic modelling. The main results are summarised in Table 6.1 and subsequent paragraphs.

**Table 6.1:** Summary of modelling results presented in this thesis

	HIP 17439	AU Mic	q <sup>1</sup> Eri
Modelled data			
• Photometric measurements	Excess emission ( $\sim 10 \dots 500 \mu\text{m}$ ) <i>Spitzer/IRS</i>	Excess emission ( $\sim 10 \dots 1\,300 \mu\text{m}$ )	Excess emission ( $\sim 10 \dots 6\,800 \mu\text{m}$ ) <i>Spitzer/IRS</i>
• SB profiles	<i>Herschel</i> (70/100/160 $\mu\text{m}$ )	Keck ( <i>V/H</i> band) <i>HST</i> ( <i>V</i> band) ALMA (1.3 mm)	<i>Herschel</i> (70/100/160 $\mu\text{m}$ )
• Polarisation		<i>HST/ACS</i>	
Disc architecture	KBA + dust transport or KBA + ABA or Extended PB	KBA + dust transport	KBA + ABA
Planetesimals			
• Location	150...180 au (KBA) 30...40 au (ABA)	$\lesssim 38 \dots \sim 43$ au (KBA)	75...125 au (KBA) 3...10 au (ABA)
• Eccentricities	$\leq 0.04$	$\leq 0.03$	$\leq 0.05$
Solid composition			
• Material (VF)	Silicate (50%) Water ice (50%)	Silicate ( $\sim 25 \dots 33\%$ ) Carbon ( $\sim 25 \dots 33\%$ ) Water ice ( $\lesssim 25\%$ ) Porosity ( $\lesssim 25\%$ )	Silicate (30%) Water ice (70%)
Host star	Working dust transport model requires SWs ( $\dot{M}_\star \leq 15 \dot{M}_\odot$ )	SW activity: $\dot{M}_\star \sim 50 \dot{M}_\odot$  Chromospheric and/or coronal activity mimic inner dust component	

**Abbreviations.** Surface brightness (SB), Kuiper belt analogue (KBA), asteroid belt analogue (ABA), planetesimal belt (PB), volume fraction (VF), stellar wind (SW).

## HIP 17439

We first tested a model with one outer planetesimal belt, reflecting Scenario II. Inspired by the one-component disc of Ertel et al. (2014b), derived from classic modelling, planetesimals were placed at distances  $> 120$  au from the star. The modelling shows that dust has to be transported efficiently from the planetesimal location to the inner region because otherwise the surface brightness of the inner disc region is too low and does not match the observations. Since P-R drag alone is not sufficient, there is a need for strong stellar winds. We identified a wind strength of 15 times the solar value as the

## 6 Conclusive remarks

upper limit if the inner edge of the planetesimal belt has a maximum distance of 150 au to the star. The assumption of stellar winds of that strength is based on theoretical considerations and is not confirmed, but also not ruled out, by observations.

Without the presence of stellar winds, the data are consistent with a two-belt disc, according to Scenario I. The separation of the belts in our best model is close to what was found for many other systems. Putative planets within the gap are in nearly circular orbits and/or have low masses since the dynamical excitation of the planetesimal belts is low ( $e_{\max} \approx 0.04$ ).

Furthermore, we argue that a multi-component disc, i.e. a generalisation of Scenario I to more than two planetesimal belts, would reproduce the data as well. Such a multi-component configuration is a model for a single radially extended planetesimal belt. We qualitatively discussed this possibility by adding a notional third planetesimal ring between the two belts existing in Scenario I. This configuration hints at a nearly constant optical depth over a wide radial range, but likely has a mass surface density profile rising outwards as expected for a long-term inside-out collisional erosion.

In summary, both Scenario I and Scenario II appear physically plausible for the HIP 17439 disc and no strict conclusion can be drawn. We discussed prospects of distinguishing between the competing scenarios by future observations. LMT and ALMA are the most promising facilities for shedding light on the radial structure of HIP 17439's debris disc by resolving its inner region in thermal emission. We simulated LMT and ALMA images of our best one- and two-belt models at millimetre/submillimetre wavelengths. These tests highlight that present-day telescopes can distinguish (although possibly not significantly) between one- or two-belt configurations but only with strong observational effort.

## AU Microscopii

We considered a wealth of available observational data for the AU Mic system, including the SED, the ALMA 1.3 mm observations, the scattered light data in  $V$  and  $H$  bands, and the measured  $V$ -band polarisation profile. Our study presents the first attempt to reproduce scattered light observations of a debris disc with collisional modelling.

AU Mic's disc possesses several substructures and asymmetries, such as bumps and warps (Liu, 2004; Schneider et al., 2014) that may be caused by the perturbing effects of so far undetected planets. Since our modelling technique is limited to axisymmetric discs, the formation of such disc features was not considered.



Most of the data can be reproduced with a Scenario II-type model. This agrees with findings of Strubbe & Chiang (2006) and includes a narrow belt of planetesimals centred at about 40 au from which dust is transported inwards by strong stellar wind drag. We made inferences on the wind strength and the stellar mass-loss rate. An extreme value of a few hundred times the solar mass loss-rate can be excluded because it leads to distinct contradictions with the observed radial behaviour of the disc colour  $V - H$  and the degree of polarisation. The best model was achieved with  $\dot{M}_\star = 50 \dot{M}_\odot$ , which corresponds to the estimated moderate wind strength during quiescent phases (Augereau & Beust, 2006).

Owing to strong inward transport of dust, the inner disc region is filled with small grains, which actively scatter stellar light in the near-IR. This is contrary to what was derived previously (Graham et al., 2007; Fitzgerald et al., 2007). Even for our best model, we noticed significant deviations between the synthetic and observed  $V - H$  and degree of linear polarisation. This problem probably arises because of the idealising assumption of spherical dust grains, whose optical properties were determined by Mie theory. There are prospects of mitigating the shortcomings between model and data by incorporating irregularly shaped grains with scattering properties different from the Mie spheres used in the modelling. We expect a preference for particles that are weak polarisers and have polarisation maxima at scattering angles different from  $90^\circ$ .

We tested a handful of selected materials for the disc objects. These contained mixtures of silicate, carbon, and ice with different degrees of porosity. Our models support the presence of ice-containing particles of moderate porosity. As found by a comparison with other works, porous particles seem to be ubiquitous in discs around BPMG members.

The radial width of the planetesimal belt cannot be constrained tightly. This was shown with a setup including a very broad planetesimal belt, extended over 1...45 au. The belt was populated with particles up to 100 m in size and had an MMSN-like surface density with initial radial index of  $-1.5$ . The inside-out evolution of this belt resulted in a rising surface density with distance from the star and a 1.3 mm profile as observed by ALMA. This model explains the formation of an outer ring-like planetesimal distribution and should be preferred if the presence of planets that dynamically cleared up the inner disc region are not confirmed in the future.

We demonstrated that the unresolved central emission at 1.3 mm, first reported by MacGregor et al. (2013), cannot stem from an inner dust belt alone. An inner belt located at  $\lesssim 3$  au, which is compatible with being unresolved in the ALMA images, emits 60% of the observed central emission at most. Thus, the central emission component

## 6 Conclusive remarks

fully or at least partly derives from stellar contributions. This puts a lower limit on the level of AU Mic's coronal and chromospheric emission in the radio range.

### **q<sup>1</sup> Eridani**

We a priori excluded Scenario II for the q<sup>1</sup> Eri system, since efficient dust transport induced by stellar winds is unlikely in a disc around an F-type star. Instead, we considered Scenario I and first simulated the long-term collisional evolution of a fiducial two-component system to derive more general conclusions.

From a comparison of the collisional simulations with predictions of a simplified analytic model of Wyatt et al. (2007a), we showed that the results are quite different. The surface density provided by the collisional simulations reveals much more material close to the star after an evolution period of 1 Gyr. The optical depth does not rise as steeply with distance from the star as predicted by the analytic model. This means that discs evolving in a steady-state regime may be able to retain larger amounts of material in the inner region at older ages than thought before.

Scenario I implies the presence of as yet undiscovered planets. Since it is the only scenario proposed so far for systems without significant transport, and since there are many two-component discs around such stars, it suggests that the Solar system-like architecture with a set of planets between asteroid and Kuiper belt analogues may be quite common. If no planets populate the gap between both components, the only remaining explanation for the formation of a two-component disc will be that planetesimals, for whatever reason, did not form in a certain region of the disc.

We applied the long-term evolution model to the q<sup>1</sup> Eri system and found it consistent with a suite of thermal emission and scattered light observational data. This is achieved with an inner planetesimal belt between 3 to 10 au and an outer one between 75 to 125 au. The initial surface density of both components is approximately five times the MMSN model. The belts contain bodies up to 50 km in radius and the planetesimal orbits have a maximum eccentricity of 0.05. Silicate grains with 70% ice content reproduce the thermal emission properties. Although this is a reasonable composition for grains in the outer belt, the presence of icy grains in the inner belt, which is inside the ice line, remains questionable. To check the scenario itself and break some of the degeneracies, it would be vital to resolve the inner belt and to detect the expected planets.

In general, the work of this thesis provides a good indication of the probable architectures of the three debris disc systems considered, with respect to the spatial distributions of planetesimals and their collisionally produced dust. However, all the models presented are not unique, because a full exploration of the parameter space by collisional modelling is unfeasible. For HIP 17439 and AU Mic, we compared the collisional modelling results with outcomes from a classic multi-dimensional power-law fitting approach. We verified the consistency, at least up to some degree, which reduces the risk that the obtained collisional models are “exotic” solutions.

## 6.2 Outlook

The modelling presented in this thesis makes several simplifying assumptions that can be improved in future work. Furthermore, recent findings from theoretical studies as well as expected data from ongoing and planned observational and laboratory campaigns can be incorporated into the modelling process. Some examples are described below.

- So far, effects of planetary perturbers are included only through the maximum eccentricities of planetesimal orbits along with the radial location and width of the planetesimal belts. Thus, improvements can be made with respect to a more elaborate consideration of planet-disc interactions. This requires the modelling of azimuthal disc asymmetries and implies that further angular variables are added to the phase space. Indeed, an analysis of globally eccentric planetesimal belts, which can naturally be explained by perturbations of planets, is currently performed with a new ACE version (Löhne et al., in preparation).
- Future models can account for or test the formation mechanisms of planetesimals. Simulations of the streaming instability reveal  $\simeq -2.8$  for the slope of the planetesimal size distribution (Johansen et al., 2015; Simon et al., 2016), which is shallower than the one used for the initial setups in our models. A change of the primordial slope of planetesimals can significantly affect the outcome of long-term collisional evolution models.
- Future work should consider more realistic phase and polarisation functions of irregular grains, e.g., as measured by Hedman & Stark (2015) over a wide range of scattering angles. A good knowledge of these functions will help to break the degeneracy between the scattering properties of (sub)micron-sized grains and their supposed spatial distribution. This is in particular true for discs that

## 6 Conclusive remarks

are highly inclined against the observing direction. Improvements in modelling the scattered light are also important for the interpretation of the great high-resolution optical/near-IR disc images, which have been obtained in the recent years.

- Our models tend to mismatch far-IR photometric data. Among other effects, this might be caused by uncertainties of the stellar spectra and optical properties of the dust particles used. The former does not allow one to precisely disentangle the stellar and disc contributions to observed fluxes, the latter leads to wrong predictions of the disc emissivity. Thus, future studies should take improved models of stellar atmospheres and dust properties into account. Stellar spectra have to be adapted to each system considered, including individual chromospheric and coronal corrections, instead of being inferred by interpolations of standard PHOENIX spectra. Improved dust models are expected from further laboratory investigations of cosmic dust analogues that will analyse temperature effects and spectral ranges, which have not been explored in much detail before (e.g., Reinert et al., 2015).

# References

- Absil, O., Defrère, D., Coudé du Foresto, V., et al. (2013), “A near-infrared interferometric survey of debris-disc stars. III. First statistics based on 42 stars observed with CHARA/FLUOR”, *Astronomy and Astrophysics*, 555:A104
- Acke, B., Min, M., Dominik, C., et al. (2012), “*Herschel* images of Fomalhaut. An extrasolar Kuiper belt at the height of its dynamical activity”, *Astronomy and Astrophysics*, 540:A125
- Adams, F. C. & Lin, D. N. C. (1993), “Transport processes and the evolution of disks”, in E. H. Levy & J. I. Lunine (Editors), *Protostars and Planets III*, pp. 721–748, University of Arizona Press
- Arakawa, M. (1999), “Collisional disruption of ice by high-velocity impact”, *Icarus*, 142:34–45
- Artymowicz, P. & Clampin, M. (1997), “Dust around main-sequence stars: nature or nurture by the interstellar medium?”, *Astrophysical Journal*, 490:863–878
- Augereau, J.-C. & Beust, H. (2006), “On the AU Microscopii debris disk. Density profiles, grain properties, and dust dynamics”, *Astronomy and Astrophysics*, 455:987–999
- Augereau, J. C., Nelson, R. P., Lagrange, A. M., et al. (2001), “Dynamical modeling of large scale asymmetries in the  $\beta$  Pictoris dust disk”, *Astronomy and Astrophysics*, 370:447–455
- Backman, D. E. & Paresce, F. (1993), “Main-sequence stars with circumstellar solid material: the Vega phenomenon”, in E. H. Levy & J. I. Lunine (Editor), *Protostars and Planets III*, pp. 1253–1304, University of Arizona Press
- Ballering, N. P., Rieke, G. H., Su, K. Y. L., et al. (2013), “A trend between cold debris disk temperature and stellar type: implications for the formation and evolution of wide-orbit planets”, *Astrophysical Journal*, 775:55
- Barge, P., Pellat, R., & Millet, J. (1982), “Diffusion of Keplerian motions by a stochastic force. II. Lorentz scattering of interplanetary dusts”, *Astronomy and Astrophysics*, 115:8–19
- Beckwith, S. V. W., Henning, T., & Nakagawa, Y. (2000), “Dust properties and assembly of large particles in protoplanetary disks”, in V. Mannings, A. P. Boss, & S. S. Russell (Editors), *Protostars and Planets IV*, pp. 533–558, University of Arizona Press

## REFERENCES

- Beichman, C. A., Neugebauer, G., Habing, H. J., et al. (Editors) (1988), *IRAS catalogs and atlases. Explanatory supplement*, vol. 1, NASA Reference Publication, 1190, Washington, D.C.
- Benz, W. (2000), “Low velocity collisions and the growth of planetesimals”, *Space Science Reviews*, 92:279–294
- Benz, W. & Asphaug, E. (1999), “Catastrophic disruptions revisited”, *Icarus*, 142:5–20
- Bertin, E. & Arnouts, S. (1996), “SExtractor: software for source extraction.”, *Astronomy and Astrophysics Supplement Series*, 117:393–404
- Beust, H., Vidal-Madjar, A., Ferlet, R., et al. (1990), “The  $\beta$  Pictoris circumstellar disk. X. Numerical simulations of infalling evaporating bodies”, *Astronomy and Astrophysics*, 236:202–216
- Beuzit, J.-L., Feldt, M., Dohlen, K., et al. (2008), “SPHERE: a ‘Planet Finder’ instrument for the VLT”, in *Ground-based and Airborne Instrumentation for Astronomy II*, vol. 7014 of *Proceedings of SPIE*, p. 701418
- Biller, B. A., Liu, M. C., Wahhaj, Z., et al. (2013), “The Gemini/NICI planet-finding campaign: the frequency of planets around young moving group stars”, *Astrophysical Journal*, 777:160
- Binks, A. S. & Jeffries, R. D. (2014), “A lithium depletion boundary age of 21 Myr for the Beta Pictoris moving group”, *Monthly Notices of the Royal Astronomical Society*, 438:L11–L15
- Blum, J. & Wurm, G. (2008), “The growth mechanisms of macroscopic bodies in protoplanetary disks”, *Annual Review of Astronomy and Astrophysics*, 46:21–56
- Boccaletti, A., Thalmann, C., Lagrange, A.-M., et al. (2015), “Fast-moving features in the debris disk around AU Microscopii”, *Nature*, 526:230–232
- Bohren, C. F. & Huffman, D. R. (1983), *Absorption and scattering of light by small particles*, Wiley, New York
- Boltzmann, L. (1896), *Vorlesungen über Gastheorie*, J. A. Barth, Leipzig
- Bonsor, A., Kennedy, G. M., Crepp, J. R., et al. (2013), “Spatially resolved images of dust belt(s) around the planet-hosting subgiant  $\kappa$  CrB”, *Monthly Notices of the Royal Astronomical Society*, 431:3025–3035
- Bonsor, A., Kennedy, G. M., Wyatt, M. C., et al. (2014), “*Herschel* observations of debris discs orbiting planet-hosting subgiants”, *Monthly Notices of the Royal Astronomical Society*, 437:3288–3297
- Bonsor, A. & Wyatt, M. C. (2012), “The scattering of small bodies in planetary systems: constraints on the possible orbits of cometary material”, *Monthly Notices of the Royal Astronomical Society*, 420:2990–3002

- Booth, M., Kennedy, G., Sibthorpe, B., et al. (2013), “Resolved debris discs around A stars in the *Herschel* DEBRIS survey”, *Monthly Notices of the Royal Astronomical Society*, 428:1263–1280
- Brandeker, A., Cataldi, G., Olofsson, G., et al. (2016), “*Herschel* detects oxygen in the  $\beta$  Pictoris debris disk”, *Astronomy and Astrophysics*, 591:A27
- Broekhoven-Fiene, H., Matthews, B. C., Kennedy, G. M., et al. (2013), “The debris disk around  $\gamma$  Doradus resolved with *Herschel*”, *Astrophysical Journal*, 762:52
- Brott, I. & Hauschildt, P. H. (2005), “A PHOENIX model atmosphere grid for *Gaia*”, in C. Turon, K. S. O’Flaherty, & M. A. C. Perryman (Editors), *The Three-Dimensional Universe with Gaia*, vol. 576 of *ESA Special Publication*, p. 565
- Brownlee, D., Tsou, P., Aléon, J., et al. (2006), “Comet 81P/Wild 2 under a microscope”, *Science*, 314:1711
- Bruggeman, D. A. G. (1935), “Berechnung verschiedener physikalischer Konstanten von heterogenen Substanzen. I. Dielektrizitätskonstanten und Leitfähigkeiten der Mischkörper aus isotropen Substanzen”, *Annalen der Physik*, 416, #7:636–664
- Bryden, G., Beichman, C. A., Carpenter, J. M., et al. (2009), “Planets and debris disks: results from a *Spitzer*/MIPS search for infrared excess”, *Astrophysical Journal*, 705:1226–1236
- Buenzli, E., Thalmann, C., Vigan, A., et al. (2010), “Dissecting the Moth: discovery of an off-centered ring in the HD 61005 debris disk with high-resolution imaging”, *Astronomy and Astrophysics*, 524:L1
- Burns, J. A., Lamy, P. L., & Soter, S. (1979), “Radiation forces on small particles in the solar system”, *Icarus*, 40, #1:1–48
- Burrows, C. J., Krist, J. E., Stapelfeldt, K. R., et al. (1995), “*HST* observations of the Beta Pictoris circumstellar disk”, in *American Astronomical Society Meeting Abstracts*, vol. 27 of *Bulletin of the American Astronomical Society*, p. 1329
- Butler, R. P., Wright, J. T., Marcy, G. W., et al. (2006), “Catalog of nearby exoplanets”, *Astrophysical Journal*, 646:505–522
- Campo Bagatin, A., Cellino, A., Davis, D. R., et al. (1994), “Wavy size distributions for collisional systems with a small-size cutoff”, *Planetary Space Science*, 42:1079–1092
- Chabrier, G., Johansen, A., Janson, M., et al. (2014), “Giant planet and brown dwarf formation”, in H. Beuther, R. S. Klessen, C. P. Dullemond, & T. Henning (Editors), *Protostars and Planets VI*, pp. 619–642
- Chavez-Dagostino, M., Bertone, E., Cruz-Saenz de Miera, F., et al. (2016), “Deep LMT/AzTEC millimeter observations of  $\epsilon$  Eridani and its surroundings”, *Monthly Notices of the Royal Astronomical Society*, 462:2285–2294

## REFERENCES

- Chen, C. H., Li, A., Bohac, C., et al. (2007), “The dust and gas around  $\beta$  Pictoris”, *Astrophysical Journal*, 666:466–474
- Chen, C. H., Mittal, T., Kuchner, M., et al. (2014), “The *Spitzer* Infrared Spectrograph debris disk catalog. I. Continuum analysis of unresolved targets”, *Astrophysical Journal Supplement Series*, 211:25
- Chen, C. H., Patten, B. M., Werner, M. W., et al. (2005), “A *Spitzer* study of dusty disks around nearby, young stars”, *Astrophysical Journal*, 634:1372–1384
- Chen, C. H., Sargent, B. A., Bohac, C., et al. (2006), “*Spitzer* IRS spectroscopy of *IRAS*-discovered debris disks”, *Astrophysical Journal Supplement Series*, 166:351–377
- Chiang, E. & Laughlin, G. (2013), “The minimum-mass extrasolar nebula: in situ formation of close-in super-Earths”, *Monthly Notices of the Royal Astronomical Society*, 431:3444–3455
- Choquet, É., Perrin, M. D., Chen, C. H., et al. (2016), “First images of debris disks around TWA 7, TWA 25, HD 35650, and HD 377”, *Astrophysical Journal Letters*, 817:L2
- Churcher, L., Wyatt, M., & Smith, R. (2011), “Resolved imaging of the HD 191089 debris disc”, *Monthly Notices of the Royal Astronomical Society*, 410:2–12
- Clampin, M., Ford, H. C., Bartko, F., et al. (2000), “Advanced camera for surveys”, in J. B. Breckinridge & P. Jakobsen (Editors), *UV, Optical, and IR Space Telescopes and Instruments*, vol. 4013 of *Proceedings of SPIE*, pp. 344–351
- Consolmagno, G. J. (1980), “Influence of the interplanetary magnetic field on cometary and primordial dust orbits: applications of Lorentz scattering”, *Icarus*, 43:203–214
- Cranmer, S. R. & Saar, S. H. (2011), “Testing a predictive theoretical model for the mass loss rates of cool stars”, *Astrophysical Journal*, 741:54
- Cranmer, S. R., Wilner, D. J., & MacGregor, M. A. (2013), “Constraining a model of turbulent coronal heating for AU Microscopii with X-ray, radio, and millimeter observations”, *Astrophysical Journal*, 772:149
- Cutri, R. M., Skrutskie, M. F., van Dyk, S., et al. (2012), “*WISE* all-sky data release”, *VizieR Online Data Catalog*, II/311
- Czechowski, A. & Mann, I. (2007), “Collisional vaporization of dust and production of gas in the  $\beta$  Pictoris dust disk”, *Astrophysical Journal*, 660:1541–1555
- Czechowski, A. & Mann, I. (2010), “Formation and acceleration of nano dust in the inner heliosphere”, *Astrophysical Journal*, 714:89–99
- Davis, D. R., Chapman, C. R., Weidenschilling, S. J., et al. (1985), “Collisional history of asteroids: evidence from Vesta and the Hirayama families”, *Icarus*, 62:30–53



- Debes, J. H., Weinberger, A. J., & Kuchner, M. J. (2009), “Interstellar medium sculpting of the HD 32297 debris disk”, *Astrophysical Journal*, 702:318–326
- Decin, G., Dominik, C., Waters, L. B. F. M., et al. (2003), “Age dependence of the Vega phenomenon: observations”, *Astrophysical Journal*, 598:636–644
- Dent, W. R. F., Wyatt, M. C., Roberge, A., et al. (2014), “Molecular gas clumps from the destruction of icy bodies in the  $\beta$  Pictoris debris disk”, *Science*, 343:1490–1492
- Dipierro, G., Laibe, G., Price, D. J., et al. (2016), “Two mechanisms for dust gap opening in protoplanetary discs”, *Monthly Notices of the Royal Astronomical Society*, 459:L1–L5
- Doering, R. L., Meixner, M., Ardila, D., et al. (2005), “The dust disk of AU Mic: *N*-band imaging and radiative transfer modeling”, in *Protostars and Planets V Posters*, no. 1286
- Dohlen, K., Langlois, M., Saisse, M., et al. (2008), “The infra-red dual imaging and spectrograph for SPHERE: design and performance”, in *Ground-based and Airborne Instrumentation for Astronomy II*, vol. 7014 of *Proceedings of SPIE*, p. 70143L
- Dohnanyi, J. S. (1969), “Collisional model of asteroids and their debris”, *Journal of Geophysics Research*, 74(10):2531–2554
- Donaldson, J. K., Lebreton, J., Roberge, A., et al. (2013), “Modeling the HD 32297 debris disk with far-infrared *Herschel* data”, *Astrophysical Journal*, 772:17
- Dowell, C. D., Allen, C. A., Babu, R. S., et al. (2003), “SHARC II: a Caltech submillimeter observatory facility camera with 384 pixels”, in T. G. Phillips & J. Zmuidzinas (Editors), *Millimeter and Submillimeter Detectors for Astronomy*, vol. 4855 of *Proceedings of SPIE*, pp. 73–87
- Draine, B. T. (2003), “Scattering by interstellar dust grains. I. Optical and ultraviolet”, *Astrophysical Journal*, 598:1017–1025
- Durda, D. D. & Dermott, S. F. (1997), “The collisional evolution of the asteroid belt and its contribution to the zodiacal cloud”, *Icarus*, 130:140–164
- Eiroa, C., Fedele, D., Maldonado, J., et al. (2010), “Cold DUSt around NEArby Stars (DUNES). First results. A resolved exo-Kuiper belt around the solar-like star  $\zeta^2$  Ret”, *Astronomy and Astrophysics*, 518:L131
- Eiroa, C., Marshall, J. P., Mora, A., et al. (2011), “*Herschel* discovery of a new class of cold, faint debris discs”, *Astronomy and Astrophysics*, 536:L4
- Eiroa, C., Marshall, J. P., Mora, A., et al. (2013), “DUSt around NEArby Stars. The survey observational results”, *Astronomy and Astrophysics*, 555:A11
- Ertel, S., Absil, O., Defrère, D., et al. (2014a), “A near-infrared interferometric survey of debris-disk stars. IV. An unbiased sample of 92 southern stars observed in *H* band with VLTI/PIONIER”, *Astronomy and Astrophysics*, 570:A128

## REFERENCES

- Ertel, S., Marshall, J. P., Augereau, J.-C., et al. (2014b), “Potential multi-component structure of the debris disk around HIP 17439 revealed by *Herschel*/DUNES”, *Astronomy and Astrophysics*, 561:A114
- Ertel, S., Wolf, S., Marshall, J. P., et al. (2012a), “A peculiar class of debris disks from *Herschel*/DUNES. A steep fall off in the far infrared”, *Astronomy and Astrophysics*, 541:A148
- Ertel, S., Wolf, S., Metchev, S., et al. (2011), “Multi-wavelength modeling of the spatially resolved debris disk of HD 107146”, *Astronomy and Astrophysics*, 533:A132
- Ertel, S., Wolf, S., & Rodmann, J. (2012b), “Observing planet-disk interaction in debris disks”, *Astronomy and Astrophysics*, 544:A61
- Faber, P. & Quillen, A. C. (2007), “The total number of giant planets in debris discs with central clearings”, *Monthly Notices of the Royal Astronomical Society*, 382:1823–1828
- Farinella, P., Paolicchi, P., & Zappala, V. (1982), “The asteroids as outcomes of catastrophic collisions”, *Icarus*, 52:409–433
- Feldman, W. C., Asbridge, J. R., Bame, S. J., et al. (1977), “Plasma and magnetic fields from the Sun”, in O. R. White (Editor), *The Solar Output and its Variation*, p. 351
- Fernandes, J. M., Vaz, A. I. F., & Vicente, L. N. (2011), “Modeling nearby FGK Population I stars: A new form of estimating stellar parameters using an optimization approach”, *Astronomy and Astrophysics*, 532:A20
- Ferreira, S. E. S., Potgieter, M. S., & Moeketsi, D. M. (2003), “Modulation effects of a changing solar wind speed on low-energy electrons”, *Advances in Space Research*, 32:675–680
- Fitzgerald, M. P., Kalas, P. G., Duchêne, G., et al. (2007), “The AU Microscopii debris disk: multiwavelength imaging and modeling”, *Astrophysical Journal*, 670:536–556
- Flaherty, K. M., Hughes, A. M., Andrews, S. M., et al. (2016), “Resolved CO gas interior to the dust rings of the HD 141569 disk”, *Astrophysical Journal*, 818:97
- Fletcher, M. & Nayakshin, S. (2016), “Planets, debris and their host metallicity correlations”, *Monthly Notices of the Royal Astronomical Society*, 461:1850–1861
- Flynn, G. J. (1994), “Interplanetary dust particles collected from the stratosphere: physical, chemical, and mineralogical properties and implications for their sources”, *Planetary Space Science*, 42:1151–1161
- Forbrich, J., Lada, C. J., Muench, A. A., et al. (2008), “New M dwarf debris disk candidates in NGC 2547”, *Astrophysical Journal*, 687:1107–1116

- France, K., Roberge, A., Lupu, R. E., et al. (2007), “A low-mass H<sub>2</sub> component to the AU Microscopii circumstellar disk”, *Astrophysical Journal*, 668:1174–1181
- Fujiwara, A. (1986), “Results obtained by laboratory simulations of catastrophic impact”, *Memorie della Società Astronomica Italiana*, 57:47–64
- Fujiwara, A., Kamimoto, G., & Tsukamoto, A. (1977), “Destruction of basaltic bodies by high-velocity impact”, *Icarus*, 31:277–288
- Garaud, P., Meru, F., Galvagni, M., et al. (2013), “From dust to planetesimals: an improved model for collisional growth in protoplanetary disks”, *Astrophysical Journal*, 764:146
- Garcés, A., Ribas, I., & Catalán, S. (2010), “Characterization of high-energy emissions of GKM stars and the effects on planet habitability”, in V. Coudé du Foresto, D. M. Gelino, & I. Ribas (Editors), *Pathways Towards Habitable Planets*, vol. 430 of *Astronomical Society of the Pacific Conference Series*, p. 437
- Gardner, J. P., Mather, J. C., Clampin, M., et al. (2006), “Science with the *James Webb Space Telescope*”, in *Society of Photo-Optical Instrumentation Engineers (SPIE) Conference Series*, vol. 6265 of *Proceedings of SPIE*, p. 62650N
- Gáspár, A., Psaltis, D., Özel, F., et al. (2012), “Modeling collisional cascades in debris disks: the numerical method”, *Astrophysical Journal*, 749:14
- Gautier, III, T. N., Rieke, G. H., Stansberry, J., et al. (2007), “Far-infrared properties of M dwarfs”, *Astrophysical Journal*, 667:527–536
- Genda, H., Kobayashi, H., & Kokubo, E. (2015), “Warm debris disks produced by giant impacts during terrestrial planet formation”, *Astrophysical Journal*, 810:136
- Golimowski, D. A., Ardila, D. R., Krist, J. E., et al. (2006), “*Hubble Space Telescope* ACS multiband coronagraphic imaging of the debris disk around  $\beta$  Pictoris”, *Astronomical Journal*, 131:3109–3130
- Graham, J. R., Kalas, P. G., & Matthews, B. C. (2007), “The signature of primordial grain growth in the polarized light of the AU Microscopii debris disk”, *Astrophysical Journal*, 654:595–605
- Gray, R. O., Corbally, C. J., Garrison, R. F., et al. (2006), “Contributions to the Nearby Stars (NStars) Project: spectroscopy of stars earlier than M0 within 40 pc – The southern sample”, *Astronomical Journal*, 132:161–170
- Greaves, J. S. (2010), “Predicting the incidence of planet and debris discs as a function of stellar mass”, *Monthly Notices of the Royal Astronomical Society*, 409:L44–L48
- Greaves, J. S., Hales, A. S., Mason, B. S., et al. (2012), “Debris discs at centimetre wavelengths: planetesimal populations in young extrasolar Kuiper belts”, *Monthly Notices of the Royal Astronomical Society*, 423:L70–L74

## REFERENCES

- Greaves, J. S., Sibthorpe, B., Acke, B., et al. (2014), “Extreme conditions in a close analog to the young Solar system: *Herschel* observations of  $\varepsilon$  Eridani”, *Astrophysical Journal Letters*, 791:L11
- Greenberg, R., Bottke, W. F., Carusi, A., et al. (1991), “Planetary accretion rates: analytical derivation”, *Icarus*, 94:98–111
- Greenberg, R., Hartmann, W. K., Chapman, C. R., et al. (1978), “Planetesimals to planets: numerical simulation of collisional evolution”, *Icarus*, 35:1–26
- Griffin, M. J., Abergel, A., Abreu, A., et al. (2010), “The *Herschel*-SPIRE instrument and its in-flight performance”, *Astronomy and Astrophysics*, 518:L3
- Grigorieva, A., Artymowicz, P., & Thébault, P. (2007a), “Collisional dust avalanches in debris discs”, *Astronomy and Astrophysics*, 461:537–549
- Grigorieva, A., Thébault, P., Artymowicz, P., et al. (2007b), “Survival of icy grains in debris discs. The role of photosputtering”, *Astronomy and Astrophysics*, 475:755–764
- Guilloteau, S., Delannoy, J., Downes, D., et al. (1992), “The IRAM interferometer on Plateau de Bure”, *Astronomy and Astrophysics*, 262:624–633
- Gundlach, B. & Blum, J. (2015), “The stickiness of micrometer-sized water-ice particles”, *Astrophysical Journal*, 798:34
- Gustafson, B. A. S. (1994), “Physics of zodiacal dust”, *Annual Review of Earth and Planetary Sciences*, 22:553–595
- Güttler, C., Blum, J., Zsom, A., et al. (2010), “The outcome of protoplanetary dust growth: pebbles, boulders, or planetesimals? I. Mapping the zoo of laboratory collision experiments”, *Astronomy and Astrophysics*, 513:A56
- Haisch, Jr., K. E., Lada, E. A., & Lada, C. J. (2001), “Disk frequencies and lifetimes in young clusters”, *Astrophysical Journal Letters*, 553:L153–L156
- Haug, U. (1958), “Über die Häufigkeitsverteilung der Bahnelemente bei den interplanetaren Staubteilchen. Mit 9 Textabbildungen”, *Zeitschrift für Astrophysik*, 44:71
- Hayashi, C. (1981), “Structure of the solar nebula, growth and decay of magnetic fields and effects of magnetic and turbulent viscosities on the nebula”, *Progress of Theoretical Physics Supplement*, 70:35–53
- Hebb, L., Petro, L., Ford, H. C., et al. (2007), “A search for planets transiting the M-dwarf debris disc host, AU Microscopii”, *Monthly Notices of the Royal Astronomical Society*, 379:63–72
- Hedman, M. M. & Stark, C. C. (2015), “Saturn’s G and D rings provide nearly complete measured scattering phase functions of nearby debris disks”, *Astrophysical Journal*, 811:67

- Heng, K. & Malik, M. (2013), “Debris discs around M stars: non-existence versus non-detection”, *Monthly Notices of the Royal Astronomical Society*, 432:2562–2572
- Heney, L. G. & Greenstein, J. L. (1941), “Diffuse radiation in the Galaxy”, *Astrophysical Journal*, 93:70–83
- Hildebrand, R. H. (1983), “The determination of cloud masses and dust characteristics from submillimetre thermal emission”, *Quarterly Journal of the Royal Astronomical Society*, 24:267
- Hillenbrand, L. A., Carpenter, J. M., Kim, J. S., et al. (2008), “The complete census of 70  $\mu\text{m}$ -bright debris disks within ‘the formation and evolution of planetary systems’ *Spitzer* legacy survey of Sun-like stars”, *Astrophysical Journal*, 677:630–656
- Ho, P. T. P., Moran, J. M., & Lo, K. Y. (2004), “The Submillimeter Array”, *Astrophysical Journal Letters*, 616:L1–L6
- Holland, W., MacIntosh, M., Fairley, A., et al. (2006), “SCUBA-2: a 10,000-pixel submillimeter camera for the James Clerk Maxwell Telescope”, in *Society of Photo-Optical Instrumentation Engineers (SPIE) Conference Series*, vol. 6275 of *Proceedings of SPIE*, p. 62751E
- Holland, W. S., Robson, E. I., Gear, W. K., et al. (1999), “SCUBA: a common-user submillimetre camera operating on the James Clerk Maxwell Telescope”, *Monthly Notices of the Royal Astronomical Society*, 303:659–672
- Holsapple, K. A. (1994), “Catastrophic disruptions and cratering of solar system bodies: a review and new results”, *Planetary Space Science*, 42:1067–1078
- Holzwarth, V. & Jardine, M. (2007), “Theoretical mass loss rates of cool main-sequence stars”, *Astronomy and Astrophysics*, 463:11–21
- Horanyi, M. (1996), “Charged dust dynamics in the Solar system”, *Annual Review of Astronomy and Astrophysics*, 34:383–418
- Houck, J. R., Roellig, T. L., van Cleve, J., et al. (2004), “The Infrared Spectrograph (IRS) on the *Spitzer Space Telescope*”, *Astrophysical Journal Supplement Series*, 154:18–24
- Houdebine, E. R. & Doyle, J. G. (1994), “Observation and modelling of main sequence star chromospheres. II. Modelling of the AU Mic (dM2.5e) hydrogen spectrum”, *Astronomy and Astrophysics*, 289:185–201
- Housen, K. R. & Holsapple, K. A. (1990), “On the fragmentation of asteroids and planetary satellites”, *Icarus*, 84:226–253
- Housen, K. R., Schmidt, R. M., & Holsapple, K. A. (1991), “Laboratory simulations of large scale fragmentation events”, *Icarus*, 94:180–190

## REFERENCES

- Hughes, D. H., Jáuregui Correa, J.-C., Schloerb, F. P., et al. (2010), “The Large Millimeter Telescope”, in *Ground-based and Airborne Telescopes III*, vol. 7733 of *Proceedings of SPIE*, p. 773312
- Ida, S. & Makino, J. (1993), “Scattering of planetesimals by a protoplanet: slowing down of runaway growth”, *Icarus*, 106:210
- Ishihara, D., Onaka, T., Kataza, H., et al. (2010), “The *AKARI*/IRC mid-infrared all-sky survey”, *Astronomy and Astrophysics*, 514:A1
- Jackson, A. P. & Wyatt, M. C. (2012), “Debris from terrestrial planet formation: the Moon-forming collision”, *Monthly Notices of the Royal Astronomical Society*, 425:657–679
- Jang-Condell, H., Chen, C. H., Mittal, T., et al. (2015), “*Spitzer* IRS spectra of debris disks in the Scorpius-Centaurus OB association”, *Astrophysical Journal*, 808:167
- Johansen, A., Blum, J., Tanaka, H., et al. (2014), “The multifaceted planetesimal formation process”, in H. Beuther, R. S. Klessen, C. P. Dullemond, & T. Henning (Editors), *Protostars and Planets VI*, pp. 547–570, University of Arizona Press
- Johansen, A., Klahr, H., & Henning, T. (2006), “Gravoturbulent formation of planetesimals”, *Astrophysical Journal*, 636:1121–1134
- Johansen, A., Mac Low, M.-M., Lacerda, P., et al. (2015), “Growth of asteroids, planetary embryos, and Kuiper belt objects by chondrule accretion”, *Science Advances*, 1:1500109
- Johansen, A., Oishi, J. S., Mac Low, M.-M., et al. (2007), “Rapid planetesimal formation in turbulent circumstellar disks”, *Nature*, 448:1022–1025
- Johnstone, C. P., Güdel, M., Brott, I., et al. (2015a), “Stellar winds on the main-sequence. II. The evolution of rotation and winds”, *Astronomy and Astrophysics*, 577:A28
- Johnstone, C. P., Güdel, M., Lüftinger, T., et al. (2015b), “Stellar winds on the main-sequence. I. Wind model”, *Astronomy and Astrophysics*, 577:A27
- Jutzi, M., Michel, P., Benz, W., et al. (2010), “Fragment properties at the catastrophic disruption threshold: the effect of the parent body’s internal structure”, *Icarus*, 207:54–65
- Kains, N., Wyatt, M. C., & Greaves, J. S. (2011), “Steady-state evolution of debris discs around solar-type stars”, *Monthly Notices of the Royal Astronomical Society*, 414:2486–2497
- Kalas, P., Graham, J. R., & Clampin, M. (2005), “A planetary system as the origin of structure in Fomalhaut’s dust belt”, *Nature*, 435:1067–1070

- Kalas, P., Liu, M. C., & Matthews, B. C. (2004), “Discovery of a large dust disk around the nearby star AU Microscopii”, *Science*, 303:1990–1992
- Kataoka, A., Tanaka, H., Okuzumi, S., et al. (2013), “Fluffy dust forms icy planetesimals by static compression”, *Astronomy and Astrophysics*, 557:L4
- Kennedy, G. M. & Piette, A. (2015), “Warm exo-Zodi from cool exo-Kuiper belts: the significance of P-R drag and the inference of intervening planets”, *Monthly Notices of the Royal Astronomical Society*, 449:2304–2311
- Kennedy, G. M. & Wyatt, M. C. (2010), “Are debris disks self-stirred?”, *Monthly Notices of the Royal Astronomical Society*, 405:1253–1270
- Kennedy, G. M. & Wyatt, M. C. (2014), “Do two-temperature debris discs have multiple belts?”, *Monthly Notices of the Royal Astronomical Society*, 444:3164–3182
- Kenyon, S. J. & Bromley, B. C. (2002), “Collisional cascades in planetesimal disks. I. Stellar flybys”, *Astronomical Journal*, 123:1757–1775
- Kenyon, S. J. & Bromley, B. C. (2004a), “Collisional cascades in planetesimal disks. II. Embedded planets”, *Astronomical Journal*, 127:513–530
- Kenyon, S. J. & Bromley, B. C. (2004b), “Detecting the dusty debris of terrestrial planet formation”, *Astrophysical Journal Letters*, 602:L133–L136
- Kenyon, S. J. & Bromley, B. C. (2008), “Variations on debris disks: icy planet formation at 30 – 150 au for 1 – 3  $M_{\odot}$  main-sequence stars”, *Astrophysical Journal Supplement Series*, 179:451–483
- Kessler, M. F., Steinz, J. A., Anderegg, M. E., et al. (1996), “The *Infrared Space Observatory (ISO)* mission.”, *Astronomy and Astrophysics*, 315:L27–L31
- Kilic, M. & Redfield, S. (2007), “A dusty disk around WD 1150–153: explaining the metals in white dwarfs by accretion from the interstellar medium versus debris disks”, *Astrophysical Journal*, 660:641–650
- Kimura, H. & Mann, I. (1998), “The electric charging of interstellar dust in the solar system and consequences for its dynamics”, *Astrophysical Journal*, 499:454–462
- Kirchschlager, F. & Wolf, S. (2013), “Porous dust grains in debris disks”, *Astronomy and Astrophysics*, 552:A54
- Kobayashi, H., Watanabe, S.-i., Kimura, H., et al. (2008), “Dust ring formation due to ice sublimation of radially drifting dust particles under the Poynting Robertson effect in debris disks”, *Icarus*, 195:871–881
- Koerner, D. W., Kim, S., Trilling, D. E., et al. (2010), “New debris disk candidates around 49 nearby stars”, *Astrophysical Journal Letters*, 710:L26–L29
- Kóspál, Á., Ardila, D. R., Moór, A., et al. (2009), “On the relationship between debris disks and planets”, *Astrophysical Journal Letters*, 700:L73–L77

## REFERENCES

- Kóspál, Á., Moór, A., Juhász, A., et al. (2013), “ALMA observations of the molecular gas in the debris disk of the 30 Myr old star HD 21997”, *Astrophysical Journal*, 776:77
- Kral, Q., Thébault, P., Augereau, J.-C., et al. (2015), “Signatures of massive collisions in debris discs. A self-consistent numerical model”, *Astronomy and Astrophysics*, 573:A39
- Kral, Q., Thébault, P., & Charnoz, S. (2013), “LIDT-DD: a new self-consistent debris disc model that includes radiation pressure and couples dynamical and collisional evolution”, *Astronomy and Astrophysics*, 558:A121
- Krijt, S. & Kama, M. (2014), “A dearth of small particles in debris disks. An energy-constrained smallest fragment size”, *Astronomy and Astrophysics*, 566:L2
- Krist, J. E., Ardila, D. R., Golimowski, D. A., et al. (2005), “*Hubble Space Telescope* Advanced Camera for Surveys coronagraphic imaging of the AU Microscopii debris disk”, *Astronomical Journal*, 129:1008–1017
- Krist, J. E., Stapelfeldt, K. R., Bryden, G., et al. (2010), “*HST* and *Spitzer* observations of the HD 207129 debris ring”, *Astronomical Journal*, 140:1051–1061
- Krist, J. E., Stapelfeldt, K. R., Bryden, G., et al. (2012), “*Hubble Space Telescope* observations of the HD 202628 debris disk”, *Astronomical Journal*, 144:45
- Krivov, A. V. (2010), “Debris disks: seeing dust, thinking of planetesimals and planets”, *Research in Astronomy and Astrophysics*, 10:383–414
- Krivov, A. V., Eiroa, C., Löhne, T., et al. (2013), “*Herschel*’s ‘cold debris disks’: background galaxies or quiescent rims of planetary systems?”, *Astrophysical Journal*, 772:32
- Krivov, A. V., Löhne, T., & Sremčević, M. (2006), “Dust distributions in debris disks: effects of gravity, radiation pressure and collisions”, *Astronomy and Astrophysics*, 455:509–519
- Krivov, A. V., Mann, I., & Krivova, N. A. (2000), “Size distributions of dust in circumstellar debris discs”, *Astronomy and Astrophysics*, 362:1127–1137
- Krivov, A. V., Müller, S., Löhne, T., et al. (2008), “Collisional and thermal emission models of debris disks: toward planetesimal population properties”, *Astrophysical Journal*, 687:608–622
- Krivov, A. V., Queck, M., Löhne, T., et al. (2007), “On the nature of clumps in debris disks”, *Astronomy and Astrophysics*, 462:199–210
- Krivov, A. V., Sremčević, M., & Spahn, F. (2005), “Evolution of a Keplerian disk of colliding and fragmenting particles: a kinetic model with application to the Edgeworth Kuiper belt”, *Icarus*, 174:105–134



- Kuchner, M. J. (2004), “A minimum-mass extrasolar nebula”, *Astrophysical Journal*, 612:1147–1151
- Kuchner, M. J. & Stark, C. C. (2010), “Collisional grooming models of the Kuiper belt dust cloud”, *Astronomical Journal*, 140:1007–1019
- Lada, C. J. (2006), “Stellar multiplicity and the initial mass function: most stars are single”, *Astrophysical Journal Letters*, 640:L63–L66
- Lagrange, A.-M., Bonnefoy, M., Chauvin, G., et al. (2010), “A giant planet imaged in the disk of the young star  $\beta$  Pictoris”, *Science*, 329:57
- Lamers, H. J. G. L. M. & Cassinelli, J. P. (1999), *Introduction to Stellar Winds*, Cambridge University Press, Cambridge
- Lebreton, J., Augereau, J.-C., Thi, W.-F., et al. (2012), “An icy Kuiper belt around the young solar-type star HD 181327”, *Astronomy and Astrophysics*, 539:A17
- Lebreton, J., Beichman, C., Bryden, G., et al. (2016), “Models of the  $\eta$  Corvi debris disk from the Keck interferometer, *Spitzer*, and *Herschel*”, *Astrophysical Journal*, 817:165
- Lebreton, J., van Lieshout, R., Augereau, J.-C., et al. (2013), “An interferometric study of the Fomalhaut inner debris disk. III. Detailed models of the exozodiacal disk and its origin”, *Astronomy and Astrophysics*, 555:A146
- Lecar, M., Podolak, M., Sasselov, D., et al. (2006), “On the location of the snow line in a protoplanetary disk”, *Astrophysical Journal*, 640:1115–1118
- Leinert, C. & Grün, E. (1990), “Interplanetary dust”, in R. Schwenn & E. Marsch (Editors), *Physics of the Inner Heliosphere. I Large-scale phenomena*, pp. 207–282, Springer-Verlag, Berlin
- Leinhardt, Z. M. & Stewart, S. T. (2009), “Full numerical simulations of catastrophic small body collisions”, *Icarus*, 199:542–559
- Lestrade, J.-F., Matthews, B. C., Sibthorpe, B., et al. (2012), “A DEBRIS disk around the planet hosting M-star GJ 581 spatially resolved with *Herschel*”, *Astronomy and Astrophysics*, 548:A86
- Lestrade, J.-F., Wyatt, M. C., Bertoldi, F., et al. (2006), “Search for cold debris disks around M-dwarfs”, *Astronomy and Astrophysics*, 460:733–741
- Lestrade, J.-F., Wyatt, M. C., Bertoldi, F., et al. (2009), “Search for cold debris disks around M-dwarfs. II”, *Astronomy and Astrophysics*, 506:1455–1467
- Li, A. & Greenberg, J. M. (1998), “A comet dust model for the  $\beta$  Pictoris disk”, *Astronomy and Astrophysics*, 331:291–313

## REFERENCES

- Lieman-Sifry, J., Hughes, A. M., Carpenter, J. M., et al. (2016), “Debris disks in the Scorpius-Centaurus OB association resolved by ALMA”, *Astrophysical Journal*, 828:25
- Liseau, R. & Artymowicz, P. (1998), “High sensitivity search for molecular gas in the  $\beta$  Pic disk. On the low gas-to-dust mass ratio of the circumstellar disk around  $\beta$  Pictoris”, *Astronomy and Astrophysics*, 334:935–942
- Liseau, R., De la Luz, V., O’Gorman, E., et al. (2016), “ALMA’s view of the Sun’s nearest neighbours: The submm/mm SEDs of the  $\alpha$  Centauri binary and a new source”, *arXiv (astro-ph)*, 1608.02384
- Liseau, R., Eiroa, C., Fedele, D., et al. (2010), “Resolving the cold debris disc around a planet-hosting star. PACS photometric imaging observations of  $q^1$  Eridani (HD 10647, HR 506)”, *Astronomy and Astrophysics*, 518:L132
- Liseau, R., Risacher, C., Brandeker, A., et al. (2008), “ $q^1$  Eridani: a solar-type star with a planet and a dust belt”, *Astronomy and Astrophysics*, 480:L47–L50
- Liseau, R., Vlemmings, W., Bayo, A., et al. (2015), “ALMA observations of  $\alpha$  Centauri. First detection of main-sequence stars at 3 mm wavelength”, *Astronomy and Astrophysics*, 573:L4
- Lissauer, J. J. (1987), “Timescales for planetary accretion and the structure of the protoplanetary disk”, *Icarus*, 69:249–265
- Liu, M. C. (2004), “Substructure in the circumstellar disk around the young star AU Microscopii”, *Science*, 305:1442–1444
- Liu, M. C., Matthews, B. C., Williams, J. P., et al. (2004), “A submillimeter search of nearby young stars for cold dust: discovery of debris disks around two low-mass stars”, *Astrophysical Journal*, 608:526–532
- Löhne, T. (2008), “Models of rotationally symmetric, collision-dominated debris discs”, Ph.D. thesis, Friedrich-Schiller-Universität Jena
- Löhne, T. (2015), “The properties of dust and planetesimals in debris systems”, Habilitation thesis, Friedrich-Schiller-Universität Jena
- Löhne, T., Augereau, J.-C., Ertel, S., et al. (2012), “Modelling the huge, *Herschel*-resolved debris ring around HD 207129”, *Astronomy and Astrophysics*, 537:A110
- Löhne, T., Krivov, A. V., & Rodmann, J. (2008), “Long-term collisional evolution of debris disks”, *Astrophysical Journal*, 673:1123–1137
- Love, S. G. & Ahrens, T. J. (1996), “Catastrophic impacts on gravity dominated asteroids”, *Icarus*, 124:141–155
- MacGregor, M. A., Wilner, D. J., Chandler, C., et al. (2016), “Constraints on planetesimal collision models in debris disks”, *Astrophysical Journal*, 823:79

- MacGregor, M. A., Wilner, D. J., Rosenfeld, K. A., et al. (2013), “Millimeter emission structure in the first ALMA image of the AU Mic debris disk”, *Astrophysical Journal Letters*, 762:L21
- Makarov, V. V. (2007), “Unraveling the origins of nearby young stars”, *Astrophysical Journal Supplement Series*, 169:105–119
- Maldonado, J., Eiroa, C., Villaver, E., et al. (2012), “Metallicity of solar-type stars with debris discs and planets”, *Astronomy and Astrophysics*, 541:A40
- Malo, L., Doyon, R., Feiden, G. A., et al. (2014), “BANYAN. IV. Fundamental parameters of low-mass star candidates in nearby young stellar kinematic groups – Isochronal age determination using magnetic evolutionary models”, *Astrophysical Journal*, 792:37
- Mamajek, E. E. & Bell, C. P. M. (2014), “On the age of the  $\beta$  Pictoris moving group”, *Monthly Notices of the Royal Astronomical Society*, 445:2169–2180
- Mamajek, E. E. & Hillenbrand, L. A. (2008), “Improved age estimation for solar-type dwarfs using activity-rotation diagnostics”, *Astrophysical Journal*, 687:1264–1293
- Maness, H. L., Kalas, P., Peek, K. M. G., et al. (2009), “*Hubble Space Telescope* optical imaging of the eroding debris disk HD 61005”, *Astrophysical Journal*, 707:1098–1114
- Marino, S., Matrà, L., Stark, C., et al. (2016), “Exocometary gas in the HD 181327 debris ring”, *Monthly Notices of the Royal Astronomical Society*
- Marmier, M., Ségransan, D., Udry, S., et al. (2013), “The CORALIE survey for southern extrasolar planets. XVII. New and updated long period and massive planets”, *Astronomy and Astrophysics*, 551:A90
- Marois, C., Macintosh, B., Barman, T., et al. (2008), “Direct imaging of multiple planets orbiting the star HR 8799”, *Science*, 322:1348
- Marois, C., Zuckerman, B., Konopacky, Q. M., et al. (2010), “Images of a fourth planet orbiting HR 8799”, *Nature*, 468:1080–1083
- Marshall, J. P., Löhne, T., Montesinos, B., et al. (2011), “A *Herschel* resolved far-infrared dust ring around HD 207129”, *Astronomy and Astrophysics*, 529:A117
- Marshall, J. P., Moro-Martín, A., Eiroa, C., et al. (2014), “Correlations between the stellar, planetary, and debris components of exoplanet systems observed by *Herschel*”, *Astronomy and Astrophysics*, 565:A15
- Masciadri, E., Mundt, R., Henning, T., et al. (2005), “Searching for massive extrasolar planets around young and nearby stars: from NACO to CHEOPS”, *Memorie della Società Astronomica Italiana*, 76:416
- Matthews, B. C., Greaves, J. S., Holland, W. S., et al. (2007), “An unbiased survey of 500 nearby stars for debris disks: a JCMT legacy program”, *Publications of the Astronomical Society of the Pacific*, 119:842–854

## REFERENCES

- Matthews, B. C., Kennedy, G., Sibthorpe, B., et al. (2015), “The AU Mic debris disk: far-infrared and submillimeter resolved imaging”, *Astrophysical Journal*, 811:100
- Matthews, B. C., Krivov, A. V., Wyatt, M. C., et al. (2014), “Observations, modeling, and theory of debris disks”, in H. Beuther, R. S. Klessen, C. P. Dullemond, & T. Henning (Editors), *Protostars and Planets VI*, pp. 521–544, University of Arizona Press
- Matthews, B. C., Sibthorpe, B., Kennedy, G., et al. (2010), “Resolving debris discs in the far-infrared: early highlights from the DEBRIS survey”, *Astronomy and Astrophysics*, 518:L135
- Mayor, M. & Queloz, D. (1995), “A Jupiter-mass companion to a solar-type star”, *Nature*, 378:355–359
- McMullin, J. P., Waters, B., Schiebel, D., et al. (2007), “CASA architecture and applications”, in R. A. Shaw, F. Hill, & D. J. Bell (Editors), *Astronomical Data Analysis Software and Systems XVI*, vol. 376 of *Astronomical Society of the Pacific Conference Series*, p. 127
- Melosh, H. J. & Ryan, E. V. (1997), “Asteroids: shattered but not dispersed”, *Icarus*, 129:562–564
- Menesson, B., Millan-Gabet, R., Serabyn, E., et al. (2014), “Constraining the exozodiacal luminosity function of main-sequence stars: complete results from the Keck Nuller mid-infrared surveys”, *Astrophysical Journal*, 797:119
- Metchev, S. A., Eisner, J. A., Hillenbrand, L. A., et al. (2005), “Adaptive optics imaging of the AU Microscopii circumstellar disk: evidence for dynamical evolution”, *Astrophysical Journal*, 622:451–462
- Mie, G. (1908), “Beiträge zur Optik trüber Medien, speziell kolloidaler Metallösungen”, *Annalen der Physik*, 330, #3:377–445
- Milli, J., Mawet, D., Pinte, C., et al. (2015), “New constraints on the dust surrounding HR 4796A”, *Astronomy and Astrophysics*, 577:A57
- Mitra-Kraev, U., Harra, L. K., Güdel, M., et al. (2005), “Relationship between X-ray and ultraviolet emission of flares from dMe stars observed by *XMM-Newton*”, *Astronomy and Astrophysics*, 431:679–686
- Mizusawa, T. F., Rebull, L. M., Stauffer, J. R., et al. (2012), “Exploring the effects of stellar rotation and wind clearing: debris disks around F stars”, *Astronomical Journal*, 144:135
- Montesinos, B., Eiroa, C., Krivov, A. V., et al. (2016), “Incidence of debris discs around FGK stars in the solar neighbourhood”, *Astronomy and Astrophysics*, 593:A51

- Montmerle, T., Augereau, J.-C., Chaussidon, M., et al. (2006), “From Suns to life: a chronological approach to the history of life on Earth. 3. Solar system formation and early evolution: the first 100 million years”, *Earth Moon and Planets*, 98:39–95
- Morales, F. Y., Rieke, G. H., Werner, M. W., et al. (2011), “Common warm dust temperatures around main-sequence stars”, *Astrophysical Journal Letters*, 730:L29
- Morales, F. Y., Werner, M. W., Bryden, G., et al. (2009), “*Spitzer* mid-IR spectra of dust debris around A and late B type stars: asteroid belt analogs and power-law dust distributions”, *Astrophysical Journal*, 699:1067–1086
- Morfill, G. E. & Grün, E. (1979), “The motion of charged dust particles in interplanetary space. I. The zodiacal dust cloud. II. Interstellar grains”, *Planetary Space Science*, 27:1269–1292
- Moro-Martín, A., Carpenter, J. M., Meyer, M. R., et al. (2007), “Are debris disks and massive planets correlated?”, *Astrophysical Journal*, 658:1312–1321
- Moro-Martín, A., Marshall, J. P., Kennedy, G., et al. (2015), “Does the presence of planets affect the frequency and properties of extrasolar Kuiper belts? Results from the *Herschel* DEBRIS and DUNES surveys”, *Astrophysical Journal*, 801:143
- Morrison, S. J. & Kratter, K. M. (2016), “Orbital stability of multi-planet systems: behavior at high masses”, *Astrophysical Journal*, 823:118
- Moshir, M., Kopan, G., Conrow, T., et al. (1990), “The *IRAS* faint source catalog, version 2”, *Bulletin of the American Astronomical Society*, 22:1325
- Mouillet, D., Larwood, J. D., Papaloizou, J. C. B., et al. (1997), “A planet on an inclined orbit as an explanation of the warp in the  $\beta$  Pictoris disc”, *Monthly Notices of the Royal Astronomical Society*, 292:896
- Mueller, H. (1948), “The foundations of optics”, *Journal of the Optical Society of America*, 38:661
- Mukai, T. & Yamamoto, T. (1982), “Solar wind pressure on interplanetary dust”, *Astronomy and Astrophysics*, 107:97–100
- Müller, S. (2010), “Thermal emission modeling of circumstellar debris disks”, Ph.D. thesis, Friedrich-Schiller-Universität Jena
- Müller, S., Löhne, T., & Krivov, A. V. (2010), “The debris disk of Vega: a steady-state collisional cascade, naturally”, *Astrophysical Journal*, 708:1728–1747
- Murakami, H., Baba, H., Barthel, P., et al. (2007), “The infrared astronomical mission *AKARI*”, *Publications of the Astronomical Society of Japan*, 59:S369
- Mustill, A. J. & Wyatt, M. C. (2009), “Debris disc stirring by secular perturbations from giant planets”, *Monthly Notices of the Royal Astronomical Society*, 399:1403–1414

## REFERENCES

- Nesvold, E. R. & Kuchner, M. J. (2015), “Gap clearing by planets in a collisional debris disk”, *Astrophysical Journal*, 798:83
- Nesvold, E. R., Kuchner, M. J., Rein, H., et al. (2013), “SMACK: a new algorithm for modeling collisions and dynamics of planetesimals in debris disks”, *Astrophysical Journal*, 777:144
- Nesvold, E. R., Naoz, S., Vican, L., et al. (2016), “Circumstellar debris disks: diagnosing the unseen perturber”, *Astrophysical Journal*, 826:19
- Neugebauer, G., Habing, H. J., van Duinen, R., et al. (1984), “The *Infrared Astronomical Satellite (IRAS)* mission”, *Astrophysical Journal Letters*, 278:L1–L6
- Neuhäuser, R., Guenther, E. W., Alves, J., et al. (2003), “An infrared imaging search for low-mass companions to members of the young nearby  $\beta$  Pic and Tucana/Horologium associations”, *Astronomische Nachrichten*, 324:535–542
- Nordström, B., Mayor, M., Andersen, J., et al. (2004), “The Geneva-Copenhagen survey of the solar neighbourhood. Ages, metallicities, and kinematic properties of  $\sim 14\,000$  F and G dwarfs”, *Astronomy and Astrophysics*, 418:989–1019
- Nyman, L.-Å., Lerner, M., Nielbock, M., et al. (2001), “SIMBA explores the southern sky”, *The Messenger*, 106:40–44
- O’Brien, D. P. & Greenberg, R. (2003), “Steady-state size distributions for collisional populations: analytical solution with size-dependent strength”, *Icarus*, 164:334–345
- Öpik, E. J. (1951), “Collision probability with the planets and the distribution of planetary matter”, *Proceedings of the Royal Irish Academy, Section A*, 54:165–199
- Ott, S. (2010), “The *Herschel* data processing system – HIPE and pipelines – Up and running since the start of the mission”, in Y. Mizumoto, K.-I. Morita, & M. Ohishi (Editors), *Astronomical Data Analysis Software and Systems XIX*, vol. 434 of *ASP Conference Series*, p. 139
- Pagano, I., Linsky, J. L., Carkner, L., et al. (2000), “*HST*/STIS echelle spectra of the dM1e star AU Microscopii outside of flares”, *Astrophysical Journal*, 532:497–513
- Pantin, E., Lagage, P. O., & Artymowicz, P. (1997), “Mid-infrared images and models of the  $\beta$  Pictoris dust disk”, *Astronomy and Astrophysics*, 327:1123–1136
- Pawellek, N. (2016), “Statistical modelling of resolved debris discs”, Ph.D. thesis, Friedrich-Schiller-Universität Jena
- Pawellek, N. & Krivov, A. V. (2015), “The dust grain size-stellar luminosity trend in debris discs”, *Monthly Notices of the Royal Astronomical Society*, 454:3207–3221
- Pawellek, N., Krivov, A. V., Marshall, J. P., et al. (2014), “Disk radii and grain sizes in *Herschel*-resolved debris disks”, *Astrophysical Journal*, 792:65

- Payne, M. J., Ford, E. B., Wyatt, M. C., et al. (2009), “Dynamical simulations of the planetary system HD 69830”, *Monthly Notices of the Royal Astronomical Society*, 393:1219–1234
- Perrin, M. D., Duchene, G., Millar-Blanchaer, M., et al. (2015), “Polarimetry with the Gemini Planet Imager: methods, performance at first light, and the circumstellar ring around HR 4796A”, *Astrophysical Journal*, 799:182
- Perryman, M. A. C., Lindegren, L., Kovalevsky, J., et al. (1997), “The *Hipparcos* catalogue”, *Astronomy and Astrophysics*, 323:L49–L52
- Pfalzner, S., Steinhausen, M., & Menten, K. (2014), “Short dissipation times of protoplanetary disks: an artifact of selection effects?”, *Astrophysical Journal Letters*, 793:L34
- Pilbratt, G. L., Riedinger, J. R., Passvogel, T., et al. (2010), “*Herschel Space Observatory*. An ESA facility for far-infrared and submillimetre astronomy”, *Astronomy and Astrophysics*, 518:L1
- Plavchan, P., Jura, M., & Lipsy, S. J. (2005), “Where are the M dwarf disks older than 10 million years?”, *Astrophysical Journal*, 631:1161–1169
- Plavchan, P., Werner, M. W., Chen, C. H., et al. (2009), “New debris disks around young, low-mass stars discovered with the *Spitzer Space Telescope*”, *Astrophysical Journal*, 698:1068–1094
- Poglitsch, A., Waelkens, C., Geis, N., et al. (2010), “The Photodetector Array Camera and Spectrometer (PACS) on the *Herschel Space Observatory*”, *Astronomy and Astrophysics*, 518:L2
- Pollack, J. B. & Cuzzi, J. N. (1980), “Scattering by nonspherical particles of size comparable to wavelength: a new semi-empirical theory and its application to tropospheric aerosols”, *Journal of Atmospheric Sciences*, 37:868–881
- Poynting, J. H. (1904), “Radiation in the Solar system: its effect on temperature and its pressure on small bodies”, *Royal Society of London Philosophical Transactions Series A*, 202:525–552
- Rayleigh, L. (1897), “On the incidence of aerial and electric waves upon small obstacles in the form of ellipsoids or elliptic cylinders, and on the passage of electric waves through a circular aperture in a conducting screen”, *Philosophical Magazine*, 44:28–52
- Raymond, S. N., Kokubo, E., Morbidelli, A., et al. (2014), “Terrestrial planet formation at home and abroad”, in H. Beuther, R. S. Klessen, C. P. Dullemond, & T. Henning (Editors), *Protostars and Planets VI*, pp. 595–618, University of Arizona Press
- Raymond, S. N., Quinn, T., & Lunine, J. I. (2005), “Terrestrial planet formation in disks with varying surface density profiles”, *Astrophysical Journal*, 632:670–676

## REFERENCES

- Rebull, L. M., Stapelfeldt, K. R., Werner, M. W., et al. (2008), “*Spitzer* MIPS observations of stars in the  $\beta$  Pictoris moving group”, *Astrophysical Journal*, 681:1484–1504
- Reidemeister, M., Krivov, A. V., Schmidt, T. O. B., et al. (2009), “A possible architecture of the planetary system HR 8799”, *Astronomy and Astrophysics*, 503:247–258
- Reidemeister, M., Krivov, A. V., Stark, C. C., et al. (2011), “The cold origin of the warm dust around  $\epsilon$  Eridani”, *Astronomy and Astrophysics*, 527:A57
- Reinert, C., Mutschke, H., Krivov, A. V., et al. (2015), “Absorption of crystalline water ice in the far infrared at different temperatures”, *Astronomy and Astrophysics*, 573:A29
- Ribas, Á., Bouy, H., & Merín, B. (2015), “Protoplanetary disk lifetimes vs. stellar mass and possible implications for giant planet populations”, *Astronomy and Astrophysics*, 576:A52
- Ricci, L., Carpenter, J. M., Fu, B., et al. (2015a), “ALMA observations of the debris disk around the young solar analog HD 107146”, *Astrophysical Journal*, 798:124
- Ricci, L., Maddison, S. T., Wilner, D., et al. (2015b), “An ATCA survey of debris disks at 7 millimeters”, *Astrophysical Journal*, 813:138
- Rieke, G. H., Gáspár, A., & Ballering, N. P. (2016), “Magnetic grain trapping and the hot excesses around early-type stars”, *Astrophysical Journal*, 816:50
- Riviere-Marichalar, P., Barrado, D., Augereau, J.-C., et al. (2012), “HD 172555: detection of  $63\ \mu\text{m}$  [OI] emission in a debris disc”, *Astronomy and Astrophysics*, 546:L8
- Riviere-Marichalar, P., Barrado, D., Montesinos, B., et al. (2014), “Gas and dust in the Beta Pictoris moving group as seen by the *Herschel Space Observatory*”, *Astronomy and Astrophysics*, 565:A68
- Roberge, A., Weinberger, A. J., Redfield, S., et al. (2005), “Rapid dissipation of primordial gas from the AU Microscopii debris disk”, *Astrophysical Journal Letters*, 626:L105–L108
- Roberge, A., Welsh, B. Y., Kamp, I., et al. (2014), “Volatile-rich circumstellar gas in the unusual 49 Ceti debris disk”, *Astrophysical Journal Letters*, 796:L11
- Robertson, H. P. (1937), “Dynamical effects of radiation in the Solar system”, *Monthly Notices of the Royal Astronomical Society*, 97:423–437
- Robinson, R. D., Linsky, J. L., Woodgate, B. E., et al. (2001), “Far-ultraviolet observations of flares on the dM0e star AU Microscopii”, *Astrophysical Journal*, 554:368–382
- Rocchetto, M., Farihi, J., Gänsicke, B. T., et al. (2015), “The frequency and infrared brightness of circumstellar discs at white dwarfs”, *Monthly Notices of the Royal Astronomical Society*, 449:574–587



- Ryan, E. V. C. (1992), “Catastrophic collisions: laboratory impact experiments, hydrocode simulations, and the scaling problem”, Ph.D. thesis, University of Arizona, Tucson
- Schneider, G., Grady, C. A., Hines, D. C., et al. (2014), “Probing for exoplanets hiding in dusty debris disks: disk imaging, characterization, and exploration with *HST*/STIS multi-roll coronagraphy”, *Astronomical Journal*, 148:59
- Schneider, P. C. & Schmitt, J. H. M. M. (2010), “X-raying the AU Microscopii debris disk”, *Astronomy and Astrophysics*, 516:A8
- Schüppler, C., Krivov, A. V., Löhne, T., et al. (2016), “Origin and evolution of two-component debris discs and an application to the  $\alpha$  Eridani system”, *Monthly Notices of the Royal Astronomical Society*, 461:2146–2154
- Schüppler, C., Löhne, T., Krivov, A. V., et al. (2014), “Collisional modelling of the debris disc around HIP 17439”, *Astronomy and Astrophysics*, 567:A127
- Schüppler, C., Löhne, T., Krivov, A. V., et al. (2015), “Collisional modelling of the AU Microscopii debris disc”, *Astronomy and Astrophysics*, 581:A97
- Schütz, O., Meeus, G., & Sterzik, M. F. (2005), “Mid-IR observations of circumstellar disks. II. Vega-type stars and a post-main sequence object”, *Astronomy and Astrophysics*, 431:175–182
- Shannon, A., Bonsor, A., Kral, Q., et al. (2016), “The unseen planets of double belt debris disc systems”, *Monthly Notices of the Royal Astronomical Society*, 462:L116–L120
- Shannon, A., Mustill, A. J., & Wyatt, M. (2015), “Capture and evolution of dust in planetary mean-motion resonances: a fast, semi-analytic method for generating resonantly trapped disc images”, *Monthly Notices of the Royal Astronomical Society*, 448:684–702
- Shen, Y., Draine, B. T., & Johnson, E. T. (2008), “Modeling porous dust grains with ballistic aggregates. I. Geometry and optical properties”, *Astrophysical Journal*, 689:260–275
- Shen, Y., Draine, B. T., & Johnson, E. T. (2009), “Modeling porous dust grains with ballistic aggregates. II. Light scattering properties”, *Astrophysical Journal*, 696:2126–2137
- Shu, F., Najita, J., Galli, D., et al. (1993), “The collapse of clouds and the formation and evolution of stars and disks”, in E. H. Levy & J. I. Lunine (Editors), *Protostars and Planets III*, pp. 3–45, University of Arizona Press
- Siegler, N., Muzerolle, J., Young, E. T., et al. (2007), “*Spitzer* 24  $\mu$ m observations of open cluster IC 2391 and debris disk evolution of FGK stars”, *Astrophysical Journal*, 654:580–594

## REFERENCES

- Simon, J. B., Armitage, P. J., Li, R., et al. (2016), “The mass and size distribution of planetesimals formed by the streaming instability. I. The role of self-gravity”, *Astrophysical Journal*, 822:55
- Siringo, G., Kreysa, E., Kovács, A., et al. (2009), “The Large APEX BOlometer CAMera LABOCA”, *Astronomy and Astrophysics*, 497:945–962
- Smith, R., Churcher, L. J., Wyatt, M. C., et al. (2009), “Resolved debris disc emission around  $\eta$  Telescopii: a young solar system or ongoing planet formation?”, *Astronomy and Astrophysics*, 493:299–308
- Smoluchowski, M. V. (1916), “Drei Vorträge über Diffusion, Brown’sche Bewegung und Koagulation von Kolloidteilchen”, *Zeitschrift für Physik*, 17:557–585
- Stark, C. C., Schneider, G., Weinberger, A. J., et al. (2014), “Revealing asymmetries in the HD 181327 debris disk: a recent massive collision or interstellar medium warping”, *Astrophysical Journal*, 789:58
- Steele, A., Hughes, A. M., Carpenter, J., et al. (2016), “Resolved millimeter-wavelength observations of debris disks around solar-type stars”, *Astrophysical Journal*, 816:27
- Stewart, S. T. & Leinhardt, Z. M. (2009), “Velocity-dependent catastrophic disruption criteria for planetesimals”, *Astrophysical Journal Letters*, 691:L133–L137
- Strubbe, L. E. & Chiang, E. I. (2006), “Dust dynamics, surface brightness profiles, and thermal spectra of debris disks: the case of AU Microscopii”, *Astrophysical Journal*, 648:652–665
- Su, K. Y. L., Rieke, G. H., Malhotra, R., et al. (2013), “Asteroid belts in debris disk twins: Vega and Fomalhaut”, *Astrophysical Journal*, 763:118
- Su, K. Y. L., Rieke, G. H., Stansberry, J. A., et al. (2006), “Debris disk evolution around A stars”, *Astrophysical Journal*, 653:675–689
- Su, K. Y. L., Rieke, G. H., Stapelfeldt, K. R., et al. (2009), “The debris disk around HR 8799”, *Astrophysical Journal*, 705:314–327
- Swinyard, B. M., Ade, P., Baluteau, J.-P., et al. (2010), “In-flight calibration of the *Herschel*-SPIRE instrument”, *Astronomy and Astrophysics*, 518:L4
- Tanaka, H., Inaba, S., & Nakazawa, K. (1996), “Steady-state size distribution for the self-similar collision cascade”, *Icarus*, 123:450–455
- Tanner, A., Beichman, C., Bryden, G., et al. (2009), “Survey of nearby FGK stars at 160  $\mu\text{m}$  with *Spitzer*”, *Astrophysical Journal*, 704:109–116
- Thalmann, C., Schmid, H. M., Boccaletti, A., et al. (2008), “SPHERE ZIMPOL: overview and performance simulation”, in *Ground-based and Airborne Instrumentation for Astronomy II*, vol. 7014 of *Proceedings of SPIE*, p. 70143F

- Thébault, P. (2009), “Vertical structure of debris discs”, *Astronomy and Astrophysics*, 505:1269–1276
- Thébault, P. (2012), “A new code to study structures in collisionally active, perturbed debris discs: application to binaries”, *Astronomy and Astrophysics*, 537:A65
- Thébault, P. (2016), “Dust production in debris discs: constraints on the smallest grains”, *Astronomy and Astrophysics*, 587:A88
- Thébault, P. & Augereau, J.-C. (2007), “Collisional processes and size distribution in spatially extended debris discs”, *Astronomy and Astrophysics*, 472:169–185
- Thébault, P., Augereau, J. C., & Beust, H. (2003), “Dust production from collisions in extrasolar planetary systems. The inner Beta Pictoris disc”, *Astronomy and Astrophysics*, 408:775–788
- Thébault, P., Marzari, F., & Augereau, J.-C. (2010), “Debris discs in binaries: a numerical study”, *Astronomy and Astrophysics*, 524:A13
- Thébault, P. & Wu, Y. (2008), “Outer edges of debris discs. How sharp is sharp?”, *Astronomy and Astrophysics*, 481:713–724
- Theissen, C. A. & West, A. A. (2014), “Warm dust around cool stars: field M dwarfs with *WISE* 12 or 22  $\mu\text{m}$  excess emission”, *Astrophysical Journal*, 794:146
- Thureau, N. D., Greaves, J. S., Matthews, B. C., et al. (2014), “An unbiased study of debris discs around A-type stars with *Herschel*”, *Monthly Notices of the Royal Astronomical Society*, 445:2558–2573
- Torres, C. A. O., Quast, G. R., da Silva, L., et al. (2006), “Search for associations containing young stars (SACY). I. Sample and searching method”, *Astronomy and Astrophysics*, 460:695–708
- Trilling, D. E., Bryden, G., Beichman, C. A., et al. (2008), “Debris disks around Sun-like stars”, *Astrophysical Journal*, 674:1086–1105
- van Dam, M. A., Le Mignant, D., & Macintosh, B. A. (2004), “Performance of the Keck Observatory adaptive-optics system”, *Applied Optics*, 43:5458–5467
- van Leeuwen, F. (2007), “Validation of the new *Hipparcos* reduction”, *Astronomy and Astrophysics*, 474:653–664
- van Lieshout, R., Dominik, C., Kama, M., et al. (2014), “Near-infrared emission from sublimating dust in collisionally active debris disks”, *Astronomy and Astrophysics*, 571:A51
- Visser, R., van Dishoeck, E. F., & Black, J. H. (2009), “The photodissociation and chemistry of CO isotopologues: applications to interstellar clouds and circumstellar disks”, *Astronomy and Astrophysics*, 503:323–343

## REFERENCES

- Vitense, C., Krivov, A. V., Kobayashi, H., et al. (2012), “An improved model of the Edgeworth-Kuiper debris disk”, *Astronomy and Astrophysics*, 540:A30
- Vitense, C., Krivov, A. V., & Löhne, T. (2010), “The Edgeworth-Kuiper debris disk”, *Astronomy and Astrophysics*, 520:A32
- Voges, W., Aschenbach, B., Boller, T., et al. (1999), “The *ROSAT* all-sky survey bright source catalogue”, *Astronomy and Astrophysics*, 349:389–405
- Wallis, M. K. & Hassan, M. H. A. (1985), “Stochastic diffusion of interplanetary dust grains orbiting under Poynting-Robertson forces”, *Astronomy and Astrophysics*, 151:435–441
- Weidenschilling, S. J. (1977), “The distribution of mass in the planetary system and solar nebula”, *Astrophysics and Space Science*, 51:153–158
- Weinberger, A. J., Becklin, E. E., Song, I., et al. (2011), “The absence of cold dust and the mineralogy and origin of the warm dust encircling BD +20 307”, *Astrophysical Journal*, 726:72
- Werner, M. W., Roellig, T. L., Low, F. J., et al. (2004), “The *Spitzer Space Telescope* mission”, *Astrophysical Journal Supplement Series*, 154:1–9
- Wetherill, G. W. (1980), “Formation of the terrestrial planets”, *Annual Review of Astronomy and Astrophysics*, 18:77–113
- Wetherill, G. W. & Stewart, G. R. (1989), “Accumulation of a swarm of small planetesimals”, *Icarus*, 77:330–357
- Wilner, D. J., Andrews, S. M., MacGregor, M. A., et al. (2012), “A resolved millimeter emission belt in the AU Mic debris disk”, *Astrophysical Journal Letters*, 749:L27
- Wilson, G. W., Austermann, J. E., Perera, T. A., et al. (2008), “The AzTEC mm-wavelength camera”, *Monthly Notices of the Royal Astronomical Society*, 386:807–818
- Wilson, W. E., Ferris, R. H., Axtens, P., et al. (2011), “The Australia Telescope Compact Array broad-band backend: description and first results”, *Monthly Notices of the Royal Astronomical Society*, 416:832–856
- Windmark, F., Birnstiel, T., Güttler, C., et al. (2012), “Planetesimal formation by sweep-up: how the bouncing barrier can be beneficial to growth”, *Astronomy and Astrophysics*, 540:A73
- Wolf, S. & Voshchinnikov, N. V. (2004), “Mie scattering by ensembles of particles with very large size parameters”, *Computer Physics Communications*, 162, #2:113–123
- Wood, B. E. (2004), “Astrospheres and solar-like stellar winds”, *Living Reviews in Solar Physics*, 1:2

- Wood, B. E., Müller, H.-R., Zank, G. P., et al. (2002), “Measured mass-loss rates of solar-like stars as a function of age and activity”, *Astrophysical Journal*, 574:412–425
- Wood, B. E., Müller, H.-R., Zank, G. P., et al. (2005), “New mass-loss measurements from astrospheric Ly $\alpha$  absorption”, *Astrophysical Journal Letters*, 628:L143–L146
- Wright, E. L., Eisenhardt, P. R. M., Mainzer, A. K., et al. (2010), “The *Wide-field Infrared Survey Explorer (WISE)*: mission description and initial on-orbit performance”, *Astronomical Journal*, 140:1868
- Wurm, G. & Blum, J. (2000), “An experimental study on the structure of cosmic dust aggregates and their alignment by motion relative to gas”, *Astrophysical Journal Letters*, 529:L57–L60
- Wurm, G., Paraskov, G., & Krauss, O. (2005), “Growth of planetesimals by impacts at  $\sim 25$  m/s”, *Icarus*, 178:253–263
- Wyatt, M. C. (2005a), “Spiral structure when setting up pericentre glow: possible giant planets at hundreds of au in the HD 141569 disk”, *Astronomy and Astrophysics*, 440:937–948
- Wyatt, M. C. (2005b), “The insignificance of P-R drag in detectable extrasolar planetesimal belts”, *Astronomy and Astrophysics*, 433:1007–1012
- Wyatt, M. C. (2006), “Dust in resonant extrasolar Kuiper belts: grain size and wavelength dependence of disk structure”, *Astrophysical Journal*, 639:1153–1165
- Wyatt, M. C. (2008), “Evolution of debris disks”, *Annual Review of Astronomy and Astrophysics*, 46:339–383
- Wyatt, M. C., Booth, M., Payne, M. J., et al. (2010), “Collisional evolution of eccentric planetesimal swarms”, *Monthly Notices of the Royal Astronomical Society*, 402:657–672
- Wyatt, M. C., Clarke, C. J., & Booth, M. (2011), “Debris disk size distributions: steady state collisional evolution with Poynting-Robertson drag and other loss processes”, *Celestial Mechanics and Dynamical Astronomy*, 111:1–28
- Wyatt, M. C. & Dent, W. R. F. (2002), “Collisional processes in extrasolar planetesimal discs: dust clumps in Fomalhaut’s debris disc”, *Monthly Notices of the Royal Astronomical Society*, 334:589–607
- Wyatt, M. C., Farihi, J., Pringle, J. E., et al. (2014), “Stochastic accretion of planetesimals on to white dwarfs: constraints on the mass distribution of accreted material from atmospheric pollution”, *Monthly Notices of the Royal Astronomical Society*, 439:3371–3391
- Wyatt, M. C., Kennedy, G., Sibthorpe, B., et al. (2012), “*Herschel* imaging of 61 Vir: implications for the prevalence of debris in low-mass planetary systems”, *Monthly Notices of the Royal Astronomical Society*, 424:1206–1223

## REFERENCES

- Wyatt, M. C., Smith, R., Greaves, J. S., et al. (2007a), “Transience of hot dust around Sun-like stars”, *Astrophysical Journal*, 658:569–583
- Wyatt, M. C., Smith, R., Su, K. Y. L., et al. (2007b), “Steady state evolution of debris disks around A stars”, *Astrophysical Journal*, 663:365–382
- Wyatt, S. P. (1969), “The electrostatic charge of interplanetary grains”, *Planetary Space Science*, 17:155–171
- Wyatt, S. P. & Whipple, F. L. (1950), “The Poynting-Robertson effect on meteor orbits”, *Astrophysical Journal*, 111:134–141
- Yamamura, I., Makiuti, S., Ikeda, N., et al. (2010), “AKARI/FIS all-sky survey point source catalogues (ISAS/JAXA)”, *VizieR Online Data Catalog*, II/298
- Youdin, A. N. & Kenyon, S. J. (2013), “From disks to planets”, in T. D. Oswalt, L. M. French, & P. Kalas (Editors), *Planets, Stars and Stellar Systems. Volume 3: Solar and Stellar Planetary Systems*, pp. 1–62
- Young, K. E., Harvey, P. M., Brooke, T. Y., et al. (2005), “The *Spitzer* c2d survey of large, nearby, interstellar clouds. I. Chamaeleon II observed with MIPS”, *Astrophysical Journal*, 628:283–297
- Zsom, A., Ormel, C. W., Güttler, C., et al. (2010), “The outcome of protoplanetary dust growth: pebbles, boulders, or planetesimals? II. Introducing the bouncing barrier”, *Astronomy and Astrophysics*, 513:A57
- Zubko, V. G., Mennella, V., Colangeli, L., et al. (1996), “Optical constants of cosmic carbon analogue grains – I. Simulation of clustering by a modified continuous distribution of ellipsoids”, *Monthly Notices of the Royal Astronomical Society*, 282:1321–1329
- Zuckerman, B. & Song, I. (2012), “A 40 Myr old gaseous circumstellar disk at 49 Ceti: massive CO-rich comet clouds at young A-type stars”, *Astrophysical Journal*, 758:77

# Units

Units employed in this thesis and their SI conversion

Symbol	Value (SI units)	Meaning
1 au	$\simeq 1.5 \times 10^{11} \text{ m}$	Astronomical unit
1", 1 arcsec	$= \pi/648\,000 \text{ rad}$	Arcsecond
1 erg	$= 10^{-7} \text{ J}$	Erg
1 Jy	$= 10^{-26} \text{ W m}^{-2} \text{ Hz}^{-1}$	Jansky
1 $L_{\odot}$	$\simeq 3.9 \times 10^{26} \text{ W}$	Solar luminosity
1 $M_{\odot}$	$\simeq 2.0 \times 10^{30} \text{ kg}$	Solar mass
1 $M_{\oplus}$	$\simeq 6.0 \times 10^{24} \text{ kg}$	Earth mass
1 pc	$\simeq 3.1 \times 10^{16} \text{ m}$	Parsec
1 $R_{\oplus}$	$\simeq 7.0 \times 10^8 \text{ m}$	Solar radius
1 yr	$\simeq 3.2 \times 10^7 \text{ s}$	Year





# List of Figures

1.1	Scenarios explaining the origin of two-component debris discs . . . . .	9
1.2	Schematic illustrating the methodology of debris disc studies . . . . .	11
2.1	Dependence of $\beta$ ratios on particle radius and stellar properties . . . . .	18
2.2	Edge-on disc geometry in side and top view . . . . .	27
3.1	Models with one planetesimal belt for HIP 17439's debris disc . . . . .	35
3.2	Timescales for collisions and transport . . . . .	37
3.3	Dust distributions with and without stellar wind activity . . . . .	38
3.4	Radial profile of the optical depth in model 2PB_II . . . . .	41
3.5	Models with two planetesimal belts for HIP 17439's debris disc . . . . .	42
3.6	One- and two-component discs seen by LMT and ALMA . . . . .	45
4.1	Models for the AU Mic disc with different stellar wind strengths . . . . .	59
4.2	Modelled and measured 1.3 mm profiles . . . . .	62
4.3	Modelled and measured scattered light profiles . . . . .	63
4.4	Modelled and measured degree of polarisation . . . . .	64
4.5	Scattering behaviour of single dust grains . . . . .	66
4.6	Influence of the dust composition on SED and polarisation . . . . .	68
4.7	SED models with different $e_{\max}$ . . . . .	69
4.8	An extended planetesimal belt model . . . . .	72
4.9	SEDs models of inner planetesimal belts . . . . .	74
5.1	Long-term evolution of a radially extended planetesimal belt . . . . .	82
5.2	Comparison between the evolution of one- and two-component discs . . . . .	85
5.3	A two-component model for the q <sup>1</sup> Eri system . . . . .	89

# List of Tables

2.1	Model parameters for ACE simulations . . . . .	24
3.1	Ertel et al.'s (2014b) best-fit results for the HIP 17439 disc . . . . .	31
3.2	Descriptions of ACE simulations for the HIP 17439 disc . . . . .	32
4.1	Photometry of the AU Mic disc . . . . .	55
4.2	Materials used for modelling of the AU Mic disc . . . . .	57
4.3	Description of ACE simulations for the AU Mic disc . . . . .	58
4.4	Power-law fitting results for the (outer) AU Mic disc . . . . .	76
5.1	Photometry of the $q^1$ Eri disc . . . . .	87
5.2	Parameters of the two-component model shown in Figure 5.3 . . . . .	90
6.1	Summary of modelling results presented in this thesis . . . . .	95

# Danksagung

*(Acknowledgements)*

„Keine Schuld ist dringender, als die, Dank zu sagen.“

MARCUS TULLIUS CICERO (106 – 43 v. CHR.)

An dieser Stelle möchte ich allen denjenigen danken, die mich während der Erstellung meiner Doktorarbeit begleitet und unterstützt haben. Allen voran ist hier Prof. Dr. Alexander V. Krivov zu nennen, der mich in den vergangenen Jahren betreut hat. Seine hohe fachliche Kompetenz und humorvolle Art gaben mir stets Antrieb, insbesondere dann, wenn das Projekt schwierige Phasen durchlebte.

Weiterhin geht mein besonderer Dank an Dr. Torsten Löhne, der für mich mit seiner gefühlt unendlichen Geduld stets ein offenes Ohr hatte und mir ein wichtiger Ansprechpartner bei vielen Problemen war. Seine hervorragenden Ratschläge und Anreize haben wesentlich zum Gelingen dieser Arbeit beigetragen.

Ausdrücklicher Dank für den wissenschaftlichen Input gebührt auch allen Koautoren, die an den in dieser Arbeit beschriebenen Veröffentlichungen mitgewirkt haben.

Bedanken möchte ich mich auch bei meiner Kollegin und Mitdotorandin Nicole Pawellek für die vielen schönen Diskussionen, in denen neben Fachlichem, auch musische, kulinarische und linguale Themen im Mittelpunkt standen.

Ferner danke ich allen weiteren Kollegen und Kolleginnen am AIU Jena für die angenehme Arbeitsatmosphäre und die heiteren Gesprächsrunden, egal ob im Büro, in der Mensa oder während abendlicher DVD-Seminare.

Schließlich und vorallem möchte ich mich bei meinem ganz persönlichen F-Stern bedanken, der mich im Leben begleitet, meinen Alltag erhellt, mich jederzeit ermutigt, Neues zu wagen, und mich jeden Tag erneut auf den richtigen Weg lenkt.



# Ehrenwörtliche Erklärung

*(Declaration of authorship)*

Ich erkläre hiermit ehrenwörtlich, dass ich die vorliegende Arbeit selbstständig, ohne unzulässige Hilfe Dritter und ohne Benutzung anderer als der angegebenen Hilfsmittel und Literatur angefertigt habe. Die aus anderen Quellen direkt oder indirekt übernommenen Daten und Konzepte sind unter Angabe der Quelle gekennzeichnet.

Weitere Personen waren an der inhaltlich-materiellen Erstellung der vorliegenden Arbeit nicht beteiligt. Insbesondere habe ich hierfür nicht die entgeltliche Hilfe von Vermittlungs- bzw. Beratungsdiensten (Promotionsberater oder andere Personen) in Anspruch genommen. Niemand hat von mir unmittelbar oder mittelbar geldwertige Leistungen für Arbeiten erhalten, die im Zusammenhang mit dem Inhalt der vorgelegten Dissertation stehen.

Die Arbeit wurde bisher weder im In- noch Ausland in gleicher oder ähnlicher Form einer anderen Prüfungsbehörde vorgelegt.

Die geltende Promotionsordnung der Physikalisch-Astronomischen Fakultät ist mir bekannt.

Ich versichere ehrenwörtlich, dass ich nach bestem Wissen die reine Wahrheit gesagt und nichts verschwiegen habe.

Jena, 26. Januar 2017

---

Christian Schüppler



# Lebenslauf

*(Curriculum vitae)*

## Zur Person

---

Name	Christian Schüppler
Geburtsdatum	12.06.1987
Geburtsort	Hildburghausen
Staatsbürgerschaft	Deutsch
Wohnanschrift	Mühlenstr. 67, 07745 Jena
Dienstanschrift	Astrophysikalisches Institut und Universitäts-Sternwarte (AIU) Friedrich-Schiller-Universität (FSU) Jena Schillergäßchen 2-3, 07745 Jena
E-Mail	christian.schueppler@uni-jena.de christian.schueppler@gmail.com

## Werdegang

---

Schulbildung	<i>1998 – 2006</i> Gymnasium Georgianum, Hildburghausen Abschluss mit Abitur
Zivildienst	<i>08/2006 – 04/2007</i> Henneberg Kliniken gGmbH, Hildburghausen
Studium	<i>04/2007 – 09/2012</i> FSU Jena, Studiengang Physik Diplomarbeit bei Prof. Dr. A. V. Krivov (AIU) Thema: Wechselwirkung von Staubaggregaten mit Sternstrahlung anhand der T-Matrix-Methode Abschluss als Diplom-Physiker
Nebentätigkeit	<i>04/2012 – 07/2012</i> Studentische Hilfskraft an der FSU Jena (AIU)

Promotion	<i>seit 10/2012</i> FSU Jena (AIU) Thema: Kollisionsmodellierung aufgelöster Trümmerscheiben Betreuer: Prof. Dr. A. V. Krivov
Lehrtätigkeit an der FSU Jena	<i>WS 2012/13, WS 2013/14, WS 2015/16</i> Leitung des Seminars „Himmelsmechanik“  <i>SS 2013</i> Assistenz im Physikalischen Grundpraktikum  <i>SS 2014, SS 2015</i> Leitung des Seminars „Physik der Planetensysteme“  <i>WS 2014/15</i> Leitung des Seminars „Einführung in die Astronomie“  <i>WS 2015/16, SS 2016</i> Betreuung von Schülern bei einer Seminarfacharbeit

## Fachbeiträge

---

Konferenz- vorträge	<i>25.07.2013</i> Dust growth 2013, Heidelberg <i>Effect of dust aggregates on SEDs of debris discs</i>  <i>08.10.2015</i> From clouds to protoplanetary discs, Berlin <i>Collisional modelling of the AU Mic debris disc</i>
Poster- präsentationen	<i>15. – 20.07.2013</i> Protostars and planets VI, Heidelberg <i>The debris disc around HIP 17439</i>  <i>28.07. – 01.08.2014</i> Planetary systems across the HR diagram, Cambridge (UK) <i>Approaching the origin of warm dust in resolved debris discs</i>



Publikationen Ch. Schüppler, A. V. Krivov, T. Löhne, M. Booth,  
F. Kirchschrager, S. Wolf  
*Origin and evolution of two-component debris discs  
and an application to the  $q^1$  Eridani system*  
Monthly Notices of the Royal Astronomical Society,  
461:2146–2154, 2016

Ch. Schüppler, T. Löhne, A. V. Krivov, S. Ertel, J. P. Marshall,  
S. Wolf, M. C. Wyatt, J.-C. Augereau, S. A. Metchev  
*Collisional modelling of the AU Microscopii debris disc*  
Astronomy & Astrophysics, 581:A97, 2015

Ch. Schüppler, T. Löhne, A. V. Krivov, S. Ertel,  
J. P. Marshall, C. Eiroa  
*Collisional modelling of the debris disc around HIP 17439*  
Astronomy & Astrophysics, 567:A127, 2014

S. Ertel, J. P. Marshall, J.-C. Augereau, A. V. Krivov,  
T. Löhne, C. Eiroa, A. Mora, C. del Burgo, B. Montesinos,  
G. Bryden, W. Danchi, F. Kirchschrager, R. Liseau,  
J. Maldonado, G. L. Pilbratt, Ch. Schüppler, Ph. Thébault,  
G. J. White, S. Wolf  
*Potential multi-component structure of the debris disk around  
HIP 17439 revealed by Herschel/DUNES*  
Astronomy & Astrophysics, 561:A114, 2014

Jena, 26. Januar 2017

---

Christian Schüppler